

FUNCTIONAL CONNECTIVITY OF THE RODENT STRIATUM

Daniel Laurence Albaugh

A dissertation submitted to the faculty at the University of North Carolina at Chapel Hill in
partial fulfillment of the requirements for the degree of Doctor of Philosophy in the
Neurobiology Curriculum in the School of Medicine

Chapel Hill
2016

Approved by:
Yen-Yu Ian Shih
Paul Manis
Warren Grill
Garret Stuber
Donita Robinson

©2016
Daniel Laurence Albaugh
ALL RIGHTS RESERVED

ABSTRACT

Daniel Laurence Albaugh: Functional Connectivity of the Rodent Striatum
(Under the Direction of Yen-Yu Ian Shih)

The striatum serves as the major input nucleus of the basal ganglia circuitry, important for its varied roles in cognition, motivation, and sensorimotor function. Despite decades of study, fundamental features of the striatum's functional organization and broader role(s) within the basal ganglia circuitry remain contentious and/or poorly defined. Given the diverse and critical roles of striatal activity in normal brain function and a multitude of disease states (including neurodegenerative and psychiatric disorders), a better understanding of this nucleus' functional organization is imperative. The use of electrophysiological tools, which predominate the field, allow for in-depth characterizations of discrete, pre-selected brain regions, but are not appropriate for delineating functional neural circuit interactions on large spatial scales in an unbiased manner. A complementary approach to these studies is the use of functional magnetic resonance imaging (fMRI), which provides global, unbiased measures of functional neural circuit and network connectivity.

In the first two studies described herein (Chapters 2 and 3), we used fMRI to map the functional response patterns to electrical DBS of the rat nucleus accumbens (NAc; ventral striatum), as well as the dual striatal outputs: external globus pallidus (GPe), and substantia nigra pars reticulata. Notable findings included the presence of negative fMRI

signals in striatum during stimulation of each nuclei, robust prefrontal cortical modulation by NAc- and GPe-DBS, and marked functional connectivity changes by high frequency DBS.

We next used optogenetic tools to more selectively map the brain-wide responses to stimulation of GPe neurons in healthy and Parkinson's disease model rats (Chapter 4), as well as dorsal striatal neurons and their motor cortical inputs (Chapter 5). Optogenetic stimulation of each nuclei elicited an intriguing dorsal striatal negative fMRI signal, observed during direct striatal stimulation as well as putative recruitment of both excitatory both inhibitory striatal inputs, and thus suggestive of neurovascular uncoupling. Additionally, results from our GPe experiments revealed that this signal may be compromised in certain neurological disease states (e.g., Parkinson's disease). Collectively, the studies described in this dissertation have exploited fMRI tools to reveal novel features of striatal connectivity, which may shed light on striatal function in health and disease.

ACKNOWLEDGEMENTS

I would like to recognize and thank several individuals for their scholarly contributions to the work presented within this dissertation. In particular, I thank Dr. Nathalie Van Den Berge for assistance with data acquisition and analysis (Chapters 3 and 4; evoked-fMRI portions), and Drs. Andrew Salzwedel and Wei Gao for their major contributions towards the analyses and interpretations of all fcMRI data presented in this work (Chapters 2-4). Finally, I thank my dissertation committee for their guidance and support throughout my doctoral studies.

I am deeply indebted to my thesis adviser, Dr. Yen-Yu Ian Shih, for his unparalleled mentorship. Ian's scientific curiosity and dedication, patience, and warm personality made my thesis studies equally productive and fun. I am unequivocally a better scientist for having studied under his leadership, and am proud to call him both a mentor and friend.

None of this work could have been completed without support from my family. I owe no larger thanks than to my beautiful wife, Courtenay. She has provided emotional and intellectual support throughout my entire doctoral studies, and is overall the best wife a guy could ask for. I am also tremendously thankful to my parents, Bruce and Melissa Albaugh, for seeing me through many difficult life challenges with unwavering optimism. With their support, I have learned the perseverance so critical for any scientist.

PREFACE

Chapter 2 was previously published as (in modified form) as:

Albaugh, D.L., Salzwedel, A., Van Den Berge, N., Gao, W., Stuber, G.D., Shih Y.Y. 2016, "Functional magnetic resonance imaging of electrical and optogenetic deep brain stimulation at the rat nucleus accumbens". *Scientific Reports*, 6: 31613.

Publications in this journal are made available under the terms of the Creative Commons Attribution license.

Chapter 3 had been accepted for publication (in modified form) in *Neuroimage*.
Publications in this journal are made available under the terms of the Creative Commons Attribution license.

TABLE OF CONTENTS

LIST OF FIGURES.....	vi
CHAPTER 1: GENERAL INTRODUCTION.....	8
1.1 The Basal Ganglia: Anatomy and Functional Circuitry.....	8
1.2 Neural Circuit and Network Mapping with Functional Magnetic Resonance Imaging (fMRI).....	22
1.3 Dissertation Aims.....	29
CHAPTER 2: FUNCTIONAL MAGNETIC RESONANCE IMAGING OF DEEP BRAIN STIMULATION AT THE RAT NUCLEUS ACCUMBENS.....	30
2.1 Introduction.....	30
2.2 Materials and Methods.....	32
2.3 Results.....	42
2.4 Discussion.....	53
CHAPTER 3: FUNCTIONAL CIRCUIT MAPPING OF STRIATAL OUTPUT NUCLEI USING SIMULTANEOUS DBS-FMRI.....	59
3.1 Introduction.....	59
3.2 Materials and Methods.....	61
3.3 Results.....	66
3.4 Discussion.....	77
CHAPTER 4: FUNCTIONAL CIRCUIT MAPPING OF THE EXTERNAL GLOBUS PALLIDUS IN THE HEALTHY AND PARKINSONIAN RAT: AN OPTOGENETIC-FMRI STUDY.....	87

4.1 Introduction.....	87
4.2 Materials and Methods.....	89
4.3 Results.....	94
4.4 Discussion.....	98
CHAPTER 5: OPTOGENETIC-FMRI CIRCUIT MAPPING OF THE STRIATUM AND ITS CORTICOSTRIATAL INPUT.....	102
5.1 Introduction.....	102
5.2 Materials and Methods.....	103
5.3 Results.....	107
5.4 Discussion.....	111
CHAPTER 6: GENERAL DISCUSSION.....	114
6.1 Patterns and Putative Sources of Dorsal Striatal Vasoconstriction	114
6.2 Suggestions for Future Experimental Directions.....	116
6.3 Summary.....	122
APPENDIX 2.1: SUPPLEMENTAL MATERIALS FOR CHAPTER 2.....	123
APPENDIX 3.1: SUPPLEMENTAL MATERIALS FOR CHAPTER 3.....	127
REFERENCES.....	136

LIST OF FIGURES

Figure 2.1: Experimental schematic and electrode targeting for NAc-DBS.....	43
Figure 2.2: Functional CBV activation maps by 130 Hz NAc-DBS.....	44
Figure 2.3: fcMRI modulation by 130 Hz NAc-DBS.....	46
Figure 2.4: Network-level visualization of pair-wise fcMRI modulations.....	48
Figure 2.5: Temporal dynamics and amplitudes of CBV responses to NAc-DBS across varying stimulation frequencies.....	50
Figure 2.6: Optogenetic stimulation at NAc evokes local CBV increases.....	52
Figure 3.1: Experimental schematic and electrode targeting for GPe- and SNr-DBS.....	66
Figure 3.2: Functional activation maps of CBV modulation by SNr- and GPe-DBS.....	68
Figure 3.3: SNr-DBS evoked CBV changes at select, anatomically-defined regions of interest.....	70
Figure 3.4: GPe-DBS evoked CBV changes at select, anatomically-defined regions of interest.....	71
Figure 3.5: fcMRI modulation via DBS of the SNr and GPe.....	74
Figure 3.6: Robust functional connectivity modulation during SNr- and GPe-DBS.....	77
Figure 4.1: Experimental Schematic for GPe optogenetic-fMRI.....	94
Figure 4.2: Striatal tyrosine hydroxylase expression following 6-OHDA treatment.....	95
Figure 4.3: Functional activation maps of CBV modulation by optogenetic GPe stimulation.....	96

Figure 4.4: Optogenetic GPe stimulation-evoked CBV changes at select, anatomically-defined regions of interest.....	98
Figure 5.1: Characterization of motor cortical and striatal fMRI responses to optogenetic stimulation of deep-layer motor cortical neurons.....	108
Figure 5.2: Characterization of fMRI responses to optogenetic stimulation of striatonigral afferents.....	110
Figure 5.3: Functional activation maps of CBV modulation by optogenetic dorsal striatal stimulation.....	111

CHAPTER 1: GENERAL INTRODUCTION

1.1 The Basal Ganglia: Anatomy and Functional Circuitry

The basal ganglia comprise a grouping of forebrain and midbrain structures, densely interconnected and multifunctional with respect to behavioral output. In brief, the basal ganglia comprises: the striatum, internal and external globus pallidus (GPi/GPe), subthalamic nucleus (STN), and substantia nigra pars reticulata (SNr). The striatum serves as the major input nucleus of the basal ganglia, whereas the GPi (entopeduncular nucleus in rodents) and SNr represent the canonical output nuclei. In rodents, the SNr is the major output whereas the entopeduncular nucleus may serve a minimal role (1); thus, only the SNr will be reviewed here. Basal ganglia inputs from cortex and the dopaminergic neurons of the midbrain (the A8-10 groupings of the retrorubral area, substantia nigra pars compacta [SNpc] and ventral tegmental area [VTA] (2)) are integral to the circuit and will thus also be reviewed. In an effort to restrain scope, the below description of the basal ganglia circuitry will largely focus on basic and functional neuroanatomy; for additional information on the cognitive-behavioral functions of the basal ganglia in health and disease, the reader is referred to several excellent recent reviews (3-11).

1.1a. Cortical Inputs to the Basal Ganglia

Inputs to Striatum

Cortical innervation of striatum (i.e., the corticostriatal pathway) arises from multiple, distinct classes of cortical projection neurons, including the intratelencephalic (IT)

and pyramidal tract (PT), as well as inhibitory projections. IT neurons reside in cortical layers 2-6, provide bilateral striatal inputs, and do not target extratelencephalic areas (12). In contrast, PT neurons reside exclusively in cortical layer Vb, innervate the striatum unilaterally, and also target a wide number of other brain areas (thalamus, brainstem) all the way to their caudal-most destinations in spinal cord (12). Both IT and PT cortical projections are excitatory and glutamatergic, forming asymmetric and axospinous synapses in striatum (13). Interestingly, available data suggest that IT neurons provide non-reciprocal inputs to PT neurons, implying a cortical hierarchy among these corticostriatal projections (14). A third, recently-defined class of corticostriatal inputs arise from somatostatin-expressing inhibitory projection neurons that monosynaptically inhibit striatal projection cells (15).

Among the additional major anatomical features of corticostriatal projections are cortical topography and patterns of innervation selectivity among striatal target neurons. Cortical inputs to striatum are topographically-organized so that different portions of the cortex project to different areas of striatum, with the entire cortex providing inputs (16-18); these observations have sustained the long-standing conceptual modeling of the cortico-basal ganglia circuits as functionally and somatotopically-organized parallel circuits (18). With respect to striatal targets, cortical projections target both striatal projection neurons and interneurons (19-21). Striatal projection neurons are broadly classified as members of the direct or indirect pathways, distinguished based upon their distinct molecular makeups and projection patterns (thoroughly described below). A recent study has conclusively shown that IT and PT cortical projections innervate both types of striatal projection neuron (21). However, there does appear to be a bias in the regional distribution

of direct vs. indirect pathway cortical inputs, for example, with primary motor cortex showing a strong bias towards innervation indirect pathway projection cells (19). The functional significance of such cortical region-dependent input biases remains unknown.

Inputs to STN

Cortical inputs to the STN, referred to as the “hyperdirect” pathway, have received increasing attention in recent years (13, 22-24). Compared to the corticostriatal projection, these inputs (arising mostly from cortical layer V) are relatively sparse (25), and appear to exhibit a more limited topographical organization (26). Functionally, it is critical to note that the hyperdirect pathway is likely to provide more rapid (and net inhibitory) modulation of basal ganglia output than its corticostriatal counterparts, and has been proposed to “prime” the basal ganglia system for incoming corticostriatal inputs (13).

1.1b. Thalamic Inputs to Striatum

In addition to cortex, the striatum also receives dense excitatory input from the thalamus, particularly the intralaminar (parafascicular and central lateral) nuclei (27, 28). Similar to corticostriatal inputs, thalamostriatal afferents are topographically-organized and target both striatal projection neurons and interneurons (28-30). However, notable distinctions also exist between the corticostriatal and thalamostriatal systems; these include the type of vesicular glutamate transporter expressed presynaptically (VGLUT 1 and 2 for cortical and thalamic inputs, respectively), as well as the location of synaptic boutons (axonspinous and axodendritic [shafts] for cortical and thalamic inputs, respectively) (28). Based on VGLUT1 expression, it can be estimated that at least a quarter of all glutamatergic synapses in striatum arise from thalamus (28). Despite this remarkable

percentage, very little is known about the functional nature of the thalamostriatal system in health or disease.

1.1c. Striatum: Major Input Nucleus of the Basal Ganglia

The striatum comprises the caudate and putamen nuclei, anatomically separated by the internal capsule in primates but not rodents; the fused structure is therefore termed the “caudate-putamen”, or simply “striatum” in rodents. Below the caudate/putamen lies the ventral striatum, also known as the nucleus accumbens (NAc), notable for its limbic functions and unique neural connectivity patterns (the latter reviewed in part within this section). Medium spiny neurons (MSNs), the projection neurons of the striatum, comprise roughly 95% of all striatal neurons (10, 31). MSNs, so-named due to their size and spine-dense dendrites (largely sites of glutamatergic input), are GABAergic and inhibitory to their projection targets (32). The major, classically-defined sites of striatal innervation are the GPe and SNr/GPi (i.e., the basal ganglia output nuclei). The MSNs that target the GPe vs. GPi/SNr form two largely-distinct neuronal subtypes, referred to as “indirect” and “direct” pathway MSNs, respectively. Neurochemically, MSNs of the indirect pathway are identifiable based on their expression of D2 dopamine and A2A adenosine receptors, as well as enkephalin; direct pathway MSNs express D1 dopamine receptors, substance P, and dynorphin (33, 34). There appears to be little to no overlap in the expression of these proteins (though see (35)), allowing for the often-used selective genetic targeting of direct vs. indirect pathway MSNs (e.g., by placing transgenes under the D1 vs. A2A receptor promoter) (36). D1 and D2 receptors are positively and negatively coupled to cAMP signaling, respectively; thus dopamine has been classically modeled as exerting opposing influences on direct and indirect pathway MSNs, acutely increasing or decreasing their

excitability (37). The modulatory role of dopamine signaling within the basal ganglia is further explored below.

The projection pathway specificity of direct and indirect pathway MSNs is perhaps the most salient feature of the traditional classification scheme of the basal ganglia (38). Recruitment of direct pathway MSN output is associated with inhibition of the tonically active basal ganglia output nuclei, which is further correlated with motor action (39, 40). In contrast, electrophysiological recordings have demonstrated that GABAergic transmission within the STN drives excitation of the downstream SNr/GPi (41). Indirect pathway-mediated inhibition of GPe neurons can thus be expected to disinhibit the STN and facilitate activity within the SNr and GPi. Although this functional architecture may suggest that the direct and indirect pathway MSNs would exhibit some level of temporal isolation in their activity (lest they compete for control of the output nuclei), both cell types are simultaneously active during movement (42). Additional complexities arise from anatomical deviations within the direct/indirect pathway scheme. For example, striatal neurons of the direct pathway may send collaterals to the GPe (43). In the ventral striatum, the entire classification scheme of direct/indirect pathways has recently been called into question; a controversy arising in part from the observation that both D1 and D2 receptor expressing MSNs project to the ventral pallidum (44).

Topographical compartmentalization of the striatum is present in at least two-major levels (45). First, the striatum is broadly divided into dorsal and ventral subdivisions based on their input/output organization. Sensorimotor cortical input preferentially innervate dorsolateral striatal component (putamen), whereas associative regions innervate the dorsomedial component (caudate) (4). The ventral striatum receives prefrontal cortical

input, and is further subdivided into core and shell territories, with dissociable anatomical and functional characteristics (46). The topographical orientation of the striatum is at least partially conserved throughout the downstream basal ganglia circuitry, e.g., as demonstrated through functionally distinct subterritories of the pallidum and SNr (1, 47, 48). A second major feature of striatal organization concerns the so-called patch/matrix organization (45). The striatal patches (or “striosomes”), enriched with mu-opioid receptors (as well as other dissociating histochemical features compared to matrix), contain striatonigral neurons that preferentially innervate the dopaminergic neurons of the pars compacta (45, 48). In contrast, the dopaminergic neurons of the SNr, preferentially distributed in its dorsal tier, preferentially target striatal neurons of the matrix compartment (45). In the initial report of the patch/matrix organization by Gerfen, it was also demonstrated that patches receive prefrontal cortical input, whereas the matrix receives sensorimotor cortical input (49). The dendrites of MSNs in each patch do not cross patch/matrix borders (although interneurons may do so) (10). The functional relevance of this striatal organization has remained fairly elusive, although recent progress has been made using modern experimental tools (50).

Comprising approximately 5% of its neuronal population, striatal interneurons are both highly functionally diverse and behaviorally-relevant (10, 51-54). Large, aspiny cholinergic interneurons represent approximately 1% of striatal interneurons, notable for their tonic activity (approximately 5 Hz) (55) and regulation of dopamine and GABA release from nigrostriatal terminals (56, 57). Parvalbumin-positive fast-spiking interneurons (FSI's) receive excitatory cortical input and provide powerful feedforward inhibition to neighboring MSNs (51). Other interneuron subtypes, including persistent and

low-threshold spiking (somatostatin, neuropeptide Y-positive) and calretinin-positive subtypes are also present, yet their functions remain poorly-defined, possibly due to their rarity (10, 51). Interestingly, interneuron numbers and wiring patterns may be altered in animal models of basal ganglia-oriented movement disorders such as Parkinson's and Huntington's diseases (58).

In addition to interneurons, MSNs themselves may provide a source of MSN inhibition via local GABAergic collaterals (i.e., lateral inhibition), both in the dorsal and ventral striatum (31, 59-63). Anatomically, these collaterals are known to be present on distal dendrites and spines of MSNs, and may thus be poised to modulate dendritic potentials (64). Physiological investigations of lateral inhibition among MSNs have traditionally been conducted with paired recording *in vitro* electrophysiology, which have been remarkably inconsistent in reporting the presence and strength of lateral inhibition (31). Czubayko and Plenz identified GABA-A receptor-mediated IPSP's (driven by MSN collaterals) in less than 50% of MSN pairings, with a synaptic failure rate also above 50% (60). In another study, the investigators were unable to identify collateral inhibition among MSNs at all (65). Findings such as these have led some investigators to question the strength of collateral synapses as a potent form of MSN feedback inhibition (31, 64, 65). However, even if lateral inhibition by a single MSN-MSN pairing is weak, the sheer number of striatal MSNs provides a means by which lateral inhibition may potentially influence striatal activity (10). Further suggestive of functional relevance, lateral inhibition among MSNs is subject to acute modulation, for example by dopamine or histamine (62, 66), and is also sharply reduced in experimental Parkinsonism (67). Additional work is clearly needed to unravel the functional significance of MSN lateral inhibition, particularly *in vivo*.

1.1d. The External Globus Pallidus (GPe): A Relay Nucleus and More

The GPe is downstream of the striatum (via D2R-expressing MSNs) in the basal ganglia's indirect pathway. It is an inhibitory nucleus, comprised largely of GABAergic neurons and a small population of cholinergic neurons (approximately 5%) clustered along its medial-ventral borders (68, 69). The GABAergic neurons of the GPe can be broadly divided into two separate yet intermingled classes, based on their developmental origins, molecular makeup, firing properties, and innervation patterns (69-73). Prototypical GPe neurons represent the major inhibitory input to the subthalamic nucleus, and are thus those neurons classically modeled in traditional basal ganglia circuit diagrams (38). These neurons arise from the medial ganglionic eminence, express parvalbumin and are concentrated within the lateral GPe (73, 74). Electrophysiologically, prototypical GPe neurons recorded *in vivo* in rat display regular activity with mean firing rates above 10Hz (sometimes substantially higher, e.g., 50Hz) (70). These neurons, which make up approximately 70% of the GPe neurons, are thus excellently poised to provide tonic inhibitory inputs to the STN (69). A second subclass of GABAergic GPe neurons have recently been examined in great detail by many groups: the arkypallidal group. Arkypallidal neurons arise from the lateral and causal ganglionic eminence, express the opioid precursor preproenkephalin and the transcription factor FoxP2 (69, 73). In contrast to the STN-projecting prototypical subclass, arkypallidal GPe neurons largely innervate the striatum in a presumptive negative feedback loop (69, 72). Very recently, it has been demonstrated that striatal MSNs of both direct and indirect pathway classes are subject to arkypallidal innervation, as well as striatal interneurons (75). Compared to prototypical

neurons, arypallidal cells are electrophysiologically defined by irregular/bursty, low-rate firing patterns (as measured in awake rat, *in vivo*) (70).

The identification of a direct GPe output to frontal cortical areas, both in rodent and monkey, has added to the growing appreciation of the GPe as a complex (i.e., not a simple relay) nucleus (76, 77). Many of the GPe neurons within this pallidocortical pathway are cholinergic, but also drive monosynaptic, GABA-mediated IPSC's in pyramidal cells and interneurons across cortical layers (76). *In vivo* spike recordings in frontal cortex have revealed a complex mixture of excitations and inhibitions driven by optogenetic stimulation of pallidostriatal fibers (76). Pallidostriatal neurons correspond, at least in part, to the cholinergic population distributed in the medial/ventral GPe (near the cholinergic nucleus basalis). However, pallidostriatal neurons receive striatal input and project to the STN, justifying their inclusion in the basal ganglia circuitry (i.e., they are not simply ectopically-placed cells of the nucleus basalis) (69).

1.1e. The Subthalamic Nucleus (STN): The Basal Ganglia's Excitatory Nucleus

The STN is the sole excitatory nucleus of the basal ganglia, and the second intermediary nucleus of the indirect pathway, receiving GPe innervation and projecting to the output nuclei of the GPi and SNr (78-81). It is located above the zona incerta and below the cerebral peduncle, in a heavily fibrous region (79, 82). As in other basal ganglia areas, there exists ample functional and anatomical evidence for a topographical organization of the STN, including motor, associative, and limbic territories (26, 79, 81). Physiologically, STN neurons are characterized by irregular activity, with average firing rates of 7-12Hz (in anesthetized rat) (83). However, STN neurons are also capable of firing at far greater frequencies, at least 250Hz during movement (83). Cortical stimulation drives a complex

cascade of responses in STN, reflecting its intimate crosstalk with both cortex (via the hyperdirect pathway) and other basal ganglia nuclei. Observed first is a fast excitation driven by direct cortical afferents, followed by a pause, then a second, delayed excitation, and finally a long-lasting inhibition (83). The delayed excitation and inhibition are likely to reflect internal basal ganglia processing, including cross-talk with the GPe.

In addition to its relay innervation of the GPi and SNr, the STN also sends projects back to the GPe (84). Excitation of the GPe by the STN may provide a mechanism of feedback inhibition that dampens the STN's activity in response to excitatory (cortical) or disinhibitory (indirect pathway) inputs. A number of studies have suggested that the reciprocal connectivity of the STN and GPe may subserve more complex neural processing (85). Of particular interest, although the activity of STN and GPe neurons are generally uncorrelated in healthy rats (recorded *in vivo*), in rats with nigrostriatal lesions and in isolated *in vitro* preparations, their activity becomes bursty and highly synchronized (83, 85). Thus, reciprocal activity within the STN-GPe circuit may be an important correlate and/or contributor of certain motor disorder symptoms.

1.1f. Mesencephalic Dopamine Inputs to the Basal Ganglia

Midbrain dopaminergic neurons provide substantial input to the basal ganglia, most notably to the striatum (both dorsal and ventral subdivisions). These dopamine neurons are segregated into three separate groupings: the retrorubral area, SNpc, and VTA (2). Each of these populations has unique inputs and projection patterns (48, 86). The VTA, located most ventromedially, predominantly sends projections to the ventral striatum/nucleus accumbens, as well as a substantial pre/frontal cortical input (i.e., the mesocorticolimbic dopamine pathway). In turn, the ventral striatum, particularly the NAc shell, send

reciprocal projections from MSN projection neurons to the VTA, as well as portions of the dorsal SNpc (87). Dopamine cells of the SNpc are located immediately dorsal and lateral to the VTA in a characteristic “moustache”-like distribution. These neurons form the nigrostriatal pathway that heavily innervates the dorsal striatum, and also sends input to frontal cortex. Whereas the medial portion of the SNpc also sends projections to ventral striatum, the lateral SNpc (as well as dopamine neurons of the SNr) appear to exclusively target the dorsal striatum (48). Reciprocal striatal inputs to the SNpc come from both dorsal and ventral striatum (48). Lastly, the retrorubral area, located dorsally and caudally to the SNpc, targets and receives reciprocal input from both dorsal and ventral striatum (2, 48).

Mesencephalic dopamine neurons target both striatal and extra-striatal regions of the basal ganglia (37, 88). Little is known regarding the role(s) of extrastriatal dopamine signaling in the basal ganglia, although pharmacological studies have demonstrated electrophysiological and behavioral changes following local administration of dopamine receptor agonists (89-92); for example, D1 and D2 receptor agonists both facilitate pacemaking activity in the STN, recorded in rat brain slices (93). The role of dopamine signaling in extra-striatal basal ganglia areas has been most thoroughly examined in the context of Parkinson’s Disease, where dopaminergic drugs have been demonstrated to, in some cases, ameliorate motor impairments in diseased animal models (89-91). However, far less is known about dopaminergic signaling in these areas (in health or disease) compared to the rich field of dopamine signaling in striatum (37, 94, 95). Here, we will only briefly address a subset of salient physiological features regarding dopaminergic regulation of striatal physiology.

Dopamine regulates activity in the striatum both acutely and through long-term plasticity mechanisms. Acutely, both corticostriatal afferents and MSNs (among other striatal microcircuit elements) are subject to dopaminergic modulation. Corticostriatal terminals express D2 dopamine receptors (G_i coupled), which serve to transiently reduce the probability of neurotransmitter release in the presence of extracellular dopamine (96). Because this presynaptic inhibition is biased for less active terminals, it may serve as a filtering mechanism to remove “noise” from the corticostriatal signal. At the level of MSNs, dopamine gates the well-described up/down state transition, wherein MSNs exhibit bistable shifts (of approximately 30mV) in membrane potential, with cortically-driven spiking occurring during the plateau depolarization (up-states) (97, 98). In rats with nigrostriatal dopamine lesions, MSNs spend significantly more time in the up-state, and are more excitable in both up- and down (hyperpolarized) states (99). Similar to the case for regulation of acute regulation of corticostriatal terminal release probability, these findings again suggest that dopamine gates and filters corticostriatal inputs (the presumptive drivers of MSN excitability). On longer time-scales, dopamine also regulates corticostriatal long-term plasticity (100). For example, a presynaptic long-term depression observed at corticostriatal synapses is facilitated and blocked by D2 receptor antagonists and agonists, respectively (although the location of the responsible D2 receptors are unknown, potentially being presynaptic, postsynaptic, or on interneurons) (101).

In addition to dopaminergic neurons, additional cell types may be present in these heavily-dopaminergic regions. The best such example of a non-dopaminergic population are the GABAergic neurons of the VTA, which send inhibitory projections to the prefrontal cortex, ventral striatum, and locally to neighboring dopamine neurons (102, 103).

Functionally, selective stimulation of these neurons has been shown to generate pauses in the activity of tonically-firing cholinergic interneurons and suppress dopamine release in the ventral striatum (102, 104). A second layer of complexity concerns the presence of neurotransmitter co-release (105), which has been convincingly demonstrated at dopaminergic synapses in both the dorsal and ventral striatum. GABA is co-released by dopaminergic neurons in both dorsal and ventral striatum, dependent upon the non-canonical presynaptic packaging of this transmitter in the vesicular monoamine transporter type 2 (VMAT2) (106, 107). Dopamine itself has also been suggested to directly interact with certain forms of the GABA-A receptors (108). In addition to GABA, glutamate co-release has also been demonstrated to occur from dopaminergic terminals, however it appears restricted to the ventral striatal division (109).

1.1g. The Substantia Nigra pars reticulata (SNr)

The SNr is the main output nucleus of the rodent basal ganglia, receiving inputs from both the direct and indirect pathways (via the striatum and STN, respectively), and projecting to multiple extra-basal ganglia targets; these include thalamus, superior colliculus, and the pontine tegmentum. It is through the regulation of these nigral outputs that the basal ganglia is ultimately believed to influence behavior.

The SNr is located ventrolaterally to the SNpc, where it is further differentiated by its relative lack of cellular density, strong enrichment of GABAergic neurons, and absence of dopaminergic neurons (although some are present, particularly in the caudal and ventral regions) (1). Glutamatergic neurons, which may also express tyrosine hydroxylase, have also been identified, forming a unique SNr subpopulation that targets the parafascicular and reticular thalamus (110). Interneurons generally appear absent in the SNr, although

local inhibition occurs through GABA release from projection neuron collaterals, which arise in the SNr and target both SNr and SNpc (1, 111).

The topographical organization of the basal ganglia would perhaps mean very little if it were not conserved at the output level of the SNr. The SNr does indeed maintain this topography in the form of lammellar, “onion-like” divisions, including a “core” located dorsolaterally (112, 113). The somatotopic arrangement of this structure has been mapped (1), and also functionally divided into sensorimotor and associative territories.

SNr projection neurons fire spontaneously and tonically at frequencies of 25-30Hz (measured in awake rodent) (114). The tonic firing of these neurons provides a putative means for bidirectional control of basal ganglia output by the direct and indirect pathways; namely, excitation and inhibition of the direct and indirect pathways, respectively, serves to relieve tonic SNr-mediated inhibition of basal ganglia output target regions (e.g., thalamic relays) via disinhibition. Suppression and excitation of the direct and indirect pathways facilitates and perhaps strengthens this tonic SNr-mediated target suppression. Evidence for this mode of disinhibitory action is mixed, and at the very least, oversimplified. For example, in the avian basal ganglia, where paired recordings of pallidal presynaptic terminals are possible alongside their thalamic inputs (experimentally feasible due to the large size of avian pallidal boutons), both inputs and outputs are simultaneously excited (115). Such a finding is certainly difficult to reconcile with modern models of basal ganglia function.

1.2. Neural Circuit and Network Mapping with Functional Magnetic Resonance Imaging (fMRI)

The series of studies described in this dissertation employed fMRI toolsets to map the circuits and networks recruited by exogenous stimulation of various basal ganglia circuit elements. Broadly, the impetus behind these studies was to elucidate how basal ganglia nuclei interact and influence extra-basal ganglia areas on a global level using spatially unbiased tools. Despite decades of study using increasingly powerful anatomical and physiological toolsets, even the most fundamental aspects of basal ganglia functional connectivity remain openly disputed (115-117). Thus, mapping of functional brain modulation by basal ganglia circuits and networks, over spatial scales far larger than those commonly used in preclinical studies, and without the experimental and analytical constraints of *a priori* hypotheses, facilitates the identification of unexpected features of basal ganglia connectivity. Insights gleaned from such fMRI studies can then, in turn, support finer-grain mechanistic analyses on smaller spatial scales (e.g., electrophysiology) to ultimately develop updated models of basal ganglia function.

This section begins with an introduction to the fMRI toolsets employed in this dissertation: evoked and functional connectivity MRI, followed by a brief examination of the electrophysiological correlates of the measured fMRI signals. I then move to discussion of the two stimulation means chosen to acutely modulate activity with select basal ganglia circuit elements: electrical deep brain stimulation and optogenetic toolsets. Broadly, these tools differ widely in their translational relevance and specificity with respect to stimulated circuit elements.

1.2a. Overview of fMRI: Evoked and Functional Connectivity MRI Paradigms

fMRI is a highly versatile toolkit used to examine whole-brain neural activity in a relatively unbiased manner, noninvasively. Blood oxygenation, volume, and/or flow are measured, which then serve as indirect metrics of neural activity (based on principles of neurovascular coupling) (118, 119). The use of varying pulse sequences, coil configurations, and other flexible experimental parameters broaden the utility of fMRI to capture neural dynamics at varying spatial and temporal resolutions. Two major types of experimental paradigms are used with fMRI, referred to as task-based and resting-state in the human fMRI literature. Task-based measures compare neural activity measure by fMRI during an experimental task (e.g., reading, listening to music, playing a game) when compared to baseline periods. A comparison of neural responses during the task and no task periods then reveals task-specific changes in brain activity. In animal models, a similar design can be used to probe the neural circuit-level responses of sensory or otherwise exogenous brain stimulation (e.g., peripheral or deep brain stimulation); these studies are referred to as “evoked-fMRI”. In comparison to task-based/evoked-fMRI, the second type of fMRI paradigm, resting state, measures spontaneous hemodynamic fluctuations that occur in the absence of a task, when the subject is at rest (120, 121). These spontaneous fluctuations, which occur at low frequencies (commonly detected at $<0.1\text{Hz}$ in humans), are then correlated by region to identify putative, functionally connected neural networks. Many of the “canonical” resting state networks defined in this manner match well to networks previously detected by other means (e.g., positron emission tomography), and in some cases, analogous networks have been identified in nonhuman primates and rodents (121, 122). In recognition of the fact that such animal “resting state” studies are not conducted in

a deliberate resting-state, we broadly refer to these as “functional connectivity” MR experiments.

1.2b. Neurophysiological Correlates of fMRI Signals

The use of hemodynamic signals as a surrogate measure of neural activity presents a major challenge to any straightforward interpretation of fMRI data. In recognition of this caveat, it is prudent to discuss the known correlates of fMRI signals with respect to more “ground-truth” measures of neuronal activity, such as electrophysiological recordings. A number of experiments have been conducted comparing fMRI-based signals (commonly BOLD, or local neural tissue oxygen saturation as a surrogate) to electrophysiological readouts obtained in the same brain region during an identical stimulus (123, 124), occasionally even as measured simultaneously (125, 126). Among the electrophysiological readouts that one may obtain are: isolated single units (spike discharge from a single neuron near the electrode tip), multi-unit activity (MUA; non-isolated discharge from multiple neurons, generally located in a 100-300 μ m radius from the tip), and the local field potential (LFP; low frequency components of the extracellular potential reflecting both spiking and perisynaptic activity over a few millimeters, generally low-pass filtered at 250Hz) (119, 127).

In a seminal study by Logothetis and colleagues, simultaneous electrophysiological and BOLD-fMRI recordings were conducted in monkeys during visual stimulation (electrodes in visual cortex) (128). Comparing the visual stimulation-evoked BOLD signal in visual cortex to MUA and LFP’s revealed several interesting findings. The LFP signal change during the BOLD signal-evoking stimulus was greater in magnitude than the MUA change, with the greatest increases occurring around the 80Hz portion of the LFP (gamma band).

Moreover, the LFP generally persisted over the stimulus duration, whereas MUA increases were transient, showing strong stimulus adaptation. Thus, it was concluded that compared to the MUA, LFP signals were more strongly correlated with the BOLD signal.

Because the LFP reflects perisynaptic activity in addition to spiking, it has been hypothesized that fMRI signals are strongly biased towards presynaptic spiking and local processing (i.e., inputs), rather than regional spiking activity. The strongest evidence for this hypothesis has come from an elegant study by Vishwanathan and Freeman, employing dual LFP/MUA and oxygen amperometry recordings in the cat visual system (123). Compared to its relay projection target of visual cortex, the lateral geniculate nucleus of the thalamus (LGN) is tuned to higher frequencies of visual stimulation. Thus, using 30Hz light pulses, the authors were able to evoke spiking activity in the LGN, without any detectable MUA signals in primary visual cortex. In this way, the authors could examine local changes in tissue oxygenation (a surrogate measure of the BOLD signal) that occur in visual cortex in the absence of spiking activity. Remarkably, despite no detectable MUA response, a clear rise in tissue oxygenation was observed, as well as LFP magnitude increases. These results provide strong evidence that spiking activity is not required for the generation of the BOLD signal, and further that the LFP is better predictive of fMRI signals than spiking activity. Such dissociations between spiking activity and fMRI signals have since been observed using fMRI signals directly, rather than oxygen amperometry (126).

For as little as is known about the electrophysiological correlates of evoked-fMRI signals, even less is known about the neuronal underpinnings of fcMRI signals (129). In a seminal study by Schölvinck and colleagues, LFP signals were obtained from monkey cortex during simultaneous fcMRI measurements, revealing positive correlations between

LFP and widespread fcMRI signals (130). In particular, LFP signals above 40Hz, in the upper gamma band, were most strongly correlated to fcMRI signals with a hemodynamic delay of 6-8 seconds. More recently, fcMRI network modulation has been reported during selective stimulation of genetically-defined neuronal populations in rats, providing perhaps more causal evidence for a neuronal contribution to fcMRI signals (131).

1.2c. Brain Stimulation Tools for fMRI-Based Circuit Mapping

How do we map neural circuit relationships using fMRI modalities in animal models? The presentation of sensory stimuli inside the scanner, including peripheral electrical stimulation, odorants, and flashing lights has proven very useful to map primary sensory pathways. However, for mapping many neural circuits, including the basal ganglia nuclei that form the subject of this dissertation, more invasive stimulation methods may be required. Among these brain stimulation tools are deep brain electrical stimulation (DBS) and optogenetics.

Electrical DBS-fMRI

DBS provides a relatively straightforward means of mapping the functional circuit architecture of a targeted neural structure. With appropriate experimental considerations, including the application of MR-compatible electrodes (132), DBS-fMRI experiments (in rodents) can be employed with relative ease (133). Perhaps more challenging is the interpretation of DBS-fMRI datasets, as electrical stimulation may modulate local cell bodies, afferents, and efferents of the targeted area, as well as fibers of passage. Thus, a highly conservative approach is required in generating experimental conclusions. However, that is not to say that these tools do not hold incredible value for fMRI-based circuit

mapping- far from it. Compared to the more selective stimulation modality of optogenetics (described below), only electrical DBS allows for the mapping of the afferent fibers to a targeted region (modulated in many cases via antidromic signal propagation) (134). Second, and perhaps more importantly, DBS-fMRI experiments in animal models may provide important insights into the neural circuit mechanisms of DBS therapy, as applied in clinical settings for the treatment of a broad range of neurological and neuropsychiatric diseases (135-137). The efficacy of DBS therapy depends upon several known factors, including the target of stimulation (substantial debate exists regarding the optimal target(s) for many disorders in which DBS is applied), as well as the frequency and pattern of stimulation (138, 139). In principal, determining the fMRI-based neural correlates to DBS at varying targets, and using therapeutically effective vs. ineffective stimulation parameters, may provide unique insights into the mechanism of DBS action. Unfortunately, due to safety concerns pertaining to the introduction of DBS equipment into the MRI scanner environment, such studies are generally not feasible in clinical populations. Thus, many research groups, including our own, have turned to animal models to study the fMRI signals generated by DBS at therapeutically-relevant targets (140-142).

Optogenetic fMRI

Optogenetics broadly refers to the genetic targeting and manipulation of light-sensitive proteins (opsins) to perturb and measure cellular function (143, 144). In neuroscience, the term is more specifically used to refer to the transgenic application of microbial opsins (generally ion channels or pumps (145)) alongside opsin-stimulating light delivery methods, to manipulate neuronal membrane potentials in a cell type-specific manner. The rapid and substantial integration of optogenetic tools by the neuroscience

community over the past decade is in large part due to the unprecedented cellular specificity and tight temporal control that these tools provide in manipulating select neuronal populations. A hallmark example is provided in a seminal study by Kravitz et al., who used the blue light-gated cation channel ChannelRhodopsin-2 (ChR2) to selectively target the striatal MSNs of the direct and indirect pathways(36). Direct and indirect pathway MSNs, being spatially intermingled, could not be selectively targeted using electrical stimulation, and pharmacological manipulations are similarly hampered by slow onset/offsets, and caveats to selectivity (e.g., the indirect pathway MSN-defining D2 dopamine receptor is present on both indirect pathway MSNs and certain corticostriatal presynaptic terminals). Using the D1R and D2R/A2A receptors as molecular labels to selectively target opsins to direct or indirect-pathway MSNs, Kravitz and colleagues demonstrated that, in mice, locomotion is facilitated by artificial (light-evoked) recruitment of the direct pathway, and suppressed by recruitment of the indirect pathway. These findings conform to the traditional models of basal ganglia pathway function established decades earlier (38, 47).

The merger of optogenetic tools and fMRI readouts, hereafter referred to as “opto-fMRI” was a fairly intuitive step for the preclinical fMRI field (146). The relatively unbiased, global brain readouts of fMRI, coupled with the neuronal targeting selectivity of optogenetics, provides an attractive means to identify novel functional neural circuit connections and networks *in vivo*. Similarly, it provides a powerful toolset for identifying the contributions of select circuits and cell populations to hemodynamic signals more generally; these findings are then hoped to translate to human fMRI studies, which provide the large bulk of fMRI research programs and are generally based on the loose

interpretation of neural hemodynamic signals without reference to circuit- or cell-type contributions. Thus, both basic scientific and translational initiatives strongly converge on the adoption of opto-fMRI toolsets in animal models.

1.3. Dissertation Aims

The studies presented in this dissertation broadly aimed to examine the neural circuit and network relationships of various basal ganglia nuclei (with an emphasis on striatum, as well as its inputs/outputs), using preclinical fMRI experiments with simultaneous deep brain stimulation techniques. The first of these studies, described in Chapter 2, employed electrical DBS of the ventral striatum/NAc to map the functional neural modulation achieved by stimulating this brain region, with an emphasis on the changes evoked at clinically therapeutic stimulation parameters. Next, in Chapter 3, electrical stimulation with simultaneous fMRI was used to functionally map the circuit and network connectivity of the two chief striatal output nuclei- the GPe and SNr. Chapter 4 extended upon this work by examining the functional circuit connectivity of the GPe, using more selective (optogenetic) stimulation tools, in both healthy and Parkinsonian subjects. Lastly, in Chapter 5, I describe optogenetic-fMRI studies aimed to elucidate the neural circuit-basis of a unique negative dorsal striatal fMRI signal observed in all of the previous chapters. The data presented herein hold implications for: 1) the neural circuit and network mechanisms of DBS therapy, 2) the neural circuit and network architecture of the striatum and its inputs and outputs, and 3) the interpretation of fMRI signal underpinnings.

CHAPTER 2: FUNCTIONAL MAGNETIC RESONANCE IMAGING OF DEEP BRAIN STIMULATION AT THE RAT NUCLEUS ACCUMBENS

2.1 Introduction

Therapeutic deep brain stimulation (DBS) therapy has become an increasingly important clinical tool in neuropsychiatry (147, 148). Among several targets under active clinical consideration for neuropsychiatric DBS, the nucleus accumbens (NAc, ventral striatum) is perhaps the most common. Functionally interfaced with both limbic and executive circuitry (46), the NAc has emerged as a promising target for several neuropsychiatric conditions, including obsessive-compulsive disorder (OCD) (149) and treatment-resistant depression (150).

A longstanding issue with DBS therapy is the unpredictability of the cellular, circuit- and network-level responses to site-specific electrical stimulation, particularly at the high stimulation frequencies that are commonly employed (>100Hz) (151). Indeed, despite active clinical use, the therapeutic mechanisms of NAc-DBS are poorly understood, impeding the development and refinement of this promising therapy. Functional brain mapping tools, including positron emission tomography (PET) and functional magnetic resonance imaging (fMRI), are promising avenues for the study of circuit and network modulation by DBS therapy (152, 153). The key strengths to fMRI-based studies of DBS include the ability to detect dynamic changes in stimulus-evoked activity and connectivity, *in vivo*, across the whole brain with reasonably high spatiotemporal resolution. Unfortunately, the implementation of fMRI tools to study NAc-DBS in clinical populations is

strongly limited by both obstructive electrode imaging artifacts and appropriate safety considerations (largely pertaining to dangers associated with the introduction of DBS equipment to the MR environment) (154).

In contrast to clinical populations, animal models of DBS can be readily studied with fMRI under far more flexible experimental conditions (133, 140, 141, 155). For example, long-duration scan sessions can be conducted to map the acute neural responses to DBS at varying stimulation frequencies. This is particularly important as DBS therapy for both movement and neuropsychiatric disorders is commonly employed only at high stimulation frequencies, suggesting frequency-dependent mechanism(s) of action (151). In the case of NAc-DBS, the effects of stimulation frequency on neural circuit modulation have not been extensively explored using neuroimaging tools. DBS-fMRI in animal models also offers flexibility in electrode choice, in particular those built using more MR-compatible materials, reducing obstructive imaging artifacts (132).

In the present study, we employed simultaneous DBS and multimodal fMRI to study the circuit and network-level effects of NAc stimulation in a healthy rat model. This model was chosen based on its widespread use in preclinical studies of NAc-DBS (156-161). Electrical stimulation of the NAc strongly modulated prefrontal cortex and a diverse complement of subcortical limbic regions, including many areas not previously detected by DBS-fMRI. We also provide the first global functional connectivity mapping of NAc-DBS at therapeutic stimulation parameters. Broadly, these DBS-fMRI measurements provide critical information regarding both the pathways modulated by NAc-DBS, as well as the strength of modulation by DBS at therapeutic parameters. Interestingly, the detected pattern and size of CBV modulation by NAc DBS was largely insensitive to stimulation

frequency. Supplementing our electrical DBS findings, we describe exploratory optogenetic-fMRI experiments with selective stimulation of NAc neurons.

2.2 Materials and Methods

Subjects

A total of 15 male Sprague-Dawley rats (300-500g, Charles River Laboratories, Wilmington MA) were included in this study. Rats were individually housed in cages with food and water available ad libitum and 12:12 day–night cycles with control of humidity and temperature. All procedures were performed in accordance with the National Institutes of Health Guidelines for Animal Research (Guide for the Care and Use of Laboratory Animals) and approved by the University of North Carolina Institutional Animal Care and Use Committee.

Experimental Overview

This study broadly consisted of four different experiments: 1) Evoked-fMRI of electrical NAc-DBS at 130 Hz (300 μ A stimulation); 2) Evoked-fMRI of electrical NAc-DBS to examine frequency-dependency of fMRI responses (10, 40, 70, 130, 200 Hz; 500 μ A stimulation); 3) Functional connectivity (fc) MRI measurements of network-level responses to NAc-DBS at 130 Hz (300 μ A stimulation); and 4) A pilot experiment examining evoked-fMRI responses to selective stimulation of NAc neurons. Evoked- and fcMRI experiments were conducted in the same group of subjects (and scanning session), whereas optogenetic experiments were conducted in a separate group of subjects.

Stereotactic Surgery

For all surgical procedures, rats were endotracheally intubated and mechanically ventilated using a small animal ventilator (CWE Inc., SAR-830/PA, Ardmore, PA). Anesthesia was maintained under a constant flow of 2% isoflurane mixed with medical air, and physiological parameters were continuously monitored and maintained within normal ranges using capnometry (Surgivet, Smith Medical, Waukesha, WI) and pulse oximetry (MouseOx Plus, STARR Life Science Corp., Oakmont, PA). Animals were head-fixed to a stereotactic frame (Kopf Instruments, Model 962, Tujunga, CA), and burr holes were prepared according to experimental coordinates. For electrical DBS experiments, homemade MRI-compatible two-channel tungsten microelectrodes were fabricated as previously described (132), and targeted to the mediodorsal boundary of the NAc core/shell (2.28 mm anterior to bregma, 1.2 mm right of midline, and 6.6 mm ventral to cortical surface). Two electrode leads (50 μ m each in diameter, approximately 1 cm in length), were adhered with a saturated sucrose solution for minimal interspace distance. These electrodes were fully insulated with polyimide except at the tips, with an *in vitro* impedance of 18-22 k Ω at 1 kHz (132). For optogenetic DBS experiments, viral microinjections were targeted to the same stereotactic coordinates used for electrode implantations. Injections were administered as either 1 or 2 μ l volumes at a flow rate of 0.1 and 0.2 μ l/min, respectively (total infusion time= 10 min). An additional 10 min was given for virus diffusion prior to slow retraction of the microsyringe needle. Chronically-implantable optic fibers (200 μ M; NA: 0.37) (162) were placed 0.5 mm above virus injection sites.

For all experiments, MR-compatible miniature brass screws (Item # 94070A031, McMaster Carr, Atlanta, GA) were anchored to the skull, and dental cement was used to seal implanted components. Surgical sutures were employed to further protect the surgical site. For electrical DBS experiments, a recovery period of at least 24 h was given prior to fMRI, while at least three weeks were given for optogenetics experiments to allow for sufficient virus expression. The relatively short surgical recovery period for electrical DBS was necessitated by the fragility of the implanted microwires, is consistent with published DBS-fMRI experiments from other groups (141, 163, 164), and is further justified by the observation that therapeutic DBS efficacy may be observed immediately following implantation (at least for movement disorders).

Functional MRI Scan Preparation

In preparation for fMRI procedures, rats were endotracheally intubated and mechanically ventilated using a small animal MR-compatible ventilator (CWE Inc., MRI-1, Ardmore, PA). Anesthesia was initially maintained under constant isoflurane (1.5-2%) mixed with medical air. Next, tail vein catheterization was performed for intravenous drug and contrast agent injections (see below). Immediately following intubation and tail vein catheterization, animals were placed within a head-holder, and harnessed to a small animal cradle (both plastic and custom-made). The cradle was lined with a circulating water blanket connected to a temperature-adjustable water bath located outside the scanner room (Thermo Scientific, Waltham, MA). A rectal probe was employed and core body temperature was maintained at $37 \pm 0.5^{\circ}\text{C}$. Mechanical ventilation volume and rate were adjusted to maintain EtCO_2 of 2.8-3.2% and SpO_2 above 96%, using capnometry (Surgivet, Smith Medical, Waukesha, WI) and pulse oximetry (MouseOx Plus, STARR Life Science

Corp., Oakmont, PA). EtCO₂ values from the capnometry system were previously calibrated against invasive sampling of arterial blood gas, reflecting a pCO₂ level of 30–40 mm Hg (165, 166).

Functional MRI

MR images were acquired on a 9.4-Tesla Bruker BioSpec system with a BGA-9S gradient insert (Bruker Corp., Billerica, MA). A homemade single-loop surface coil with an internal diameter of 1.6 cm, placed directly over the head, was used as a transceiver. Toothpaste was applied within the open coil loop to minimize MR susceptibility artifacts. The set-up of the coil and DBS electrode is shown in **Figure 2.1A**.

Magnetic field homogeneity was optimized first by global shim and followed by local first- and second-order shims using the FASTMAP protocol (167). For anatomical referencing, a T₂-weighted RARE pilot image was taken in the mid-sagittal plane to localize the anterior commissure; this structure is located at approximately 0.36 mm posterior to the bregma and served as a reference for anteroposterior slice positioning in subsequent anatomical and functional scans. T₂-weighted anatomical images were obtained using a RARE sequence (scan parameters: TR = 2500 ms, TE_{eff} = 33 ms, RARE factor = 8, slice thickness = 1 mm, matrix size = 256 x 256, FOV = 2.56 x 2.56 cm²). Twelve coronal slices were acquired, with the 5th slice from the anterior direction aligned with the anterior commissure (as revealed in the previous T₂-weighted pilot scan). The reduced electrode distortion artifact (**Supplemental Figure S2.1**), together with standardized slice positioning, rendered these images sufficient to localize the electrode tip placement, as previously described (132, 140). As visualized slices were 1mm thick, all correctly targeted electrodes fell within approximately the same anteroposterior plane; we deemed this

resolution adequate given the relatively large anteroposterior size of the NAc. For optogenetic-fMRI experiments, optic fiber placements above the NAc virus injection site were similarly visualized using the anatomical scan image. Electrode and optic fiber placements within the NAc were confirmed for each rat (**Figure 2.1B and Supplemental Figure S2.1**); animals with placements outside of the target regions or defective electrodes were discarded for subsequent experiments ($n = 3$).

Following setup processes and immediately prior to cerebral blood volume (CBV) fMRI scan acquisition, rats were administered a monocrystalline iron oxide contrast agent (MION; Feraheme; 30 mg Fe/kg, i.v.). Subsequently, anesthesia was switched from 1.5-2% isoflurane to sedation using dexmedetomidine (dexdomitor; 0.05 mg/kg/hr, i.v.) cocktailed with the paralytic agent pancuronium bromide (0.5 mg/kg/hr, i.v.) (to facilitate mechanical ventilation). This cocktail was administered for the remaining scan duration, continuously supplemented by 0.5% isoflurane (168). A delay of at least 10 min was given before beginning fMRI experiments, to allow animals for animals to adjust to sedation. Total experimental duration was limited to a maximum of three hours (following Feraheme injection) for all subjects.

CBV fMRI was chosen against the more traditional blood-oxygen-level-dependent (BOLD) fMRI due to its superior contrast-to-noise ratio (169). CBV fMRI scans were acquired using a multi-slice single-shot gradient echo echo-planar imaging sequence (GE-EPI) (scan parameters: TR = 1000 ms, TE = 8.1 ms, bandwidth = 250 kHz, slice thickness = 1 mm, matrix size = 80 x 80 (zero-padding to 128 x 128), and FOV = 2.56 x 2.56 cm². Image slice geometry was imported from the previously acquired T₂-weighted anatomical image (12 slices).

Deep Brain Stimulation (DBS)

Simultaneous electrical DBS with CBV fMRI was acquired in the same manner for all subjects showing accurate electrode placement ($n = 9$), using bipolar and uniformly-distributed unilateral stimulation of the right NAc. Subjects with inaccurate electrode placement were excluded for subsequent experiments. Each stimulation period consisted of a series of TTL-triggered biphasic, charge-balanced square-wave pulses delivered at 130 Hz, with a stimulation intensity of 300 μ A and pulse duration of 90 μ s (Experiment 1). A 70 s block design paradigm was implemented (adopted from one of our previous DBS-fMRI studies) (140), consisting of 20 s of rest (stimulation OFF) followed by 10 s of stimulation ON, and an additional 40 s of rest (stimulation OFF). In a second set of experiments designed to test frequency-dependency of DBS-evoked CBV modulation (Experiment 2), higher current amplitude was employed (500 μ A). These experiments, conducted prior to the observation of detectable CBV responses at 300 μ A, nevertheless fall within normal amplitude ranges (or lower) for rodent DBS-fMRI experiments (140, 170). Stimulation frequencies were varied in a pseudo-randomized order (i.e., 130, 40, 70, 200, 10 Hz), consistent across subjects yet designed to eliminate potential stimulation frequency order effects. The application of a fixed pulse duration in this experiment (i.e., 90 μ s), while varying total charge delivered by stimulation frequency, was chosen to mimic the short pulse durations used clinically, which may be biased for targeting axons over somata (171). Each DBS frequency scan was repeated 5-times per rat for within-subject/session averaging (note that all descriptions of n refer to total rat number). An additional rest period of at least two min was given between all evoked-fMRI DBS scans (electrical and optogenetic [see below]) to allow for neurovascular recovery.

For Experiment 3, fcMRI scans were acquired using EPI scan parameters identical to those for evoked-fMRI data (see above), however with a 5 min (300 frame) scan duration ($n = 7$). First, a pre-stimulation (“resting”) baseline scan was acquired, wherein no NAc-DBS was applied. Immediately afterwards, a second fcMRI scan was acquired with simultaneous, continuous 130 Hz NAc-DBS (300 μ A). This was again followed by a resting, post-stimulation scan in which no DBS was applied.

In Experiment 4, a pilot experiment examining the evoked-fMRI responses to optogenetic stimulation at NAc ($n = 4$ for ChR2; $n = 2$ for EYFP control), a 473 nm wavelength diode-pumped solid-state (DPSS) laser (model BL473T8-200, Shanghai Laser & Optics Century, Shanghai, China) was connected via coupler to a homemade patch cable terminating above the chronically-implanted optic fibers. Wavelength-specific light output at the terminating end of the patch cable was pre-calibrated to 20 mW using a wattage meter. Optogenetic stimulation periods consisted of a series of TTL-triggered light pulses with a stimulation frequency of 40 Hz and pulse duration of 5 or 10 ms. A 100 s block design paradigm was implemented, consisting of 20 s rest (stimulation OFF) followed by two 10 s stimulation periods (stimulation ON), with intervening and final rest periods of 30 s. The use of a two stimulation period design was chosen to enhance detection sensitivity for within-scan optogenetically-driven fMRI signal changes through the inclusion of two stimulation periods, and matches prior studies from our group demonstrating robust optogenetically-driven fMRI responses (172, 173).

Stimulus-Evoked Data Processing and Statistical Analyses

Preprocessing and image analysis was performed using SPM codes and a custom-written program in Matlab (MathWorks Inc., Natick, MA) similar to our previous DBS-fMRI

studies (132, 133, 140). CBV fMRI data were automatically realigned to the first volume of a well-positioned subject. These datasets were semi-automatically skull-stripped using a thresholding method and coregistered to an anatomical MRI rat atlas (174).

Functional DBS response maps were generated using the general linear model (GLM), statistical significance was set at $p \leq 0.05$. To control for multiple comparisons, the Benjamini and Hochberg/ Yekutieli procedure for controlling false discovery rate was utilized (175). All images were smoothed by applying a mean filter with a 3×3 kernel, and overlaid on an anatomical MRI rat atlas (174) or group-averaged raw EPI data for visualization. Responses are expressed in T-score units ranging from 2 to 10.

For temporal analysis of electrical DBS-evoked CBV changes, 3-dimensional regions of interest (ROIs) were defined *a priori* according to anatomical structural boundaries (174, 176), and applied onto the coregistered data. The ROIs chosen for time-course analysis included only those regions showing statistically significant modulation during 130 Hz DBS with 300 μ A current (see **Figure 2.2**).

The effect of DBS stimulation frequency on Δ CBV change was calculated by averaging CBV values from the 10 second stimulation epochs. The baseline ΔR_2^* value was calculated as follows: Baseline $\Delta R_2^* = -1/TE \ln(S_{\text{prestim}}/S_0)$, where S_{prestim} and S_0 represents MR signal intensity after and before Feraheme injection. Stimulus evoked ΔR_2^* values were calculated as follows: Stimulus evoked $\Delta R_2^* = -1/TE \ln(S_{\text{stim}}/S_{\text{prestim}})$, where S_{stim} and S_{prestim} are the MR signal intensities during and before stimulation, respectively. Cerebral blood volume changes were calculated by dividing stimulus-evoked ΔR_2^* by baseline ΔR_2^* values; because S_{prestim} is used, this corrects for any potential baseline drift. Statistical

comparisons of DBS frequency effects on Δ CBV for each ROI were conducted using Graphpad Prism software (San Diego, CA). Two-tailed, one-way repeated measures ANOVA tests were conducted with Tukey post-hoc analyses. Statistical significance was set at $p \leq 0.05$.

Functional Connectivity Data Processing and Statistical Analyses

Functional scans were preprocessed using the Analysis of Functional NeuroImages software suite (AFNI v2011-12-21-1014). The workflow included discarding the first 20 volumes, slice-timing correction, motion correction, alignment to a pre-existing high-resolution T₂-weighted template, spatial smoothing (Gaussian kernel FWHM = 1.5 mm), low-pass filtering (0.001 Hz), and regression of whole brain signal and the six motion parameters. The number of volumes discarded was increased from the traditional number (approximately 3-10) in order to ensure DBS-related changes from the initial stimulation were minimized. Furthermore, warping in the alignment procedure was limited to shifts and rotations to avoid unnecessary shearing and scaling of brain regions with signal drop-out associated with the DBS electrode. fcMRI analyses were conducted using the temporal correlation method. Fisher-Z transformed correlation matrices were generated using the average functional time series extracted for each region-of-interest (ROI) in the template atlas. Left (LH) and right hemispheres (RH; ipsilateral to DBS electrode) ROIs were analyzed separately yielding correlation matrices detailing within and between hemisphere connectivity. The ROIs were further separated into two putative networks, a NAc-DBS network consisting of regions with robust DBS-evoked responses, as well as the ventral tegmental area (due to its highly established involvement in NAc circuitry)(46) versus Other, a network made up of 30 miscellaneous brain regions. The NAc-DBS network

included the following 15 regions: prelimbic cortex (PLC), infralimbic cortex (ILC), orbitofrontal cortex (OFC), cingulate cortex (CC), insula, nucleus accumbens (NAc), anterior striatum (AS), ventral pallidum (vPall), septum (Sept), lateral hypothalamus (lHyp), amygdala (Amyg), bed nucleus of the stria terminalis (BNST), mediodorsal thalamus (MDT), ventral hippocampus (vHipp), and the ventral tegmental area (VTA). Repeated measures analyses of variance (MATLAB, rANOVA) were implemented in order to test the effects of the stimulation paradigm (Pre-DBS Rest, DBS, Post-DBS Rest) and the interaction with mean connectivity responses within and between hemispheres (RH, LH, RH↔LH) across animals ($n = 7$). P-values were assessed using the more conservative lower-bound estimate (p_{lb}) in order to correct for potential violations in symmetry.

Individual connections, or pair-wise correlations (i.e. NAc↔OFC, etc), were further evaluated in the context of the stimulation paradigm and relative direction of effect (Connectivity versus Condition). Direction of effect was determined by fitting each significant (rANOVA, $p \leq 0.05$ uncorrected) set of pair-wise connections with a 2nd-order polynomial. The resulting sign of the quadratic term was used to categorize connections as either enhanced (increased correlation) or suppressed (increased anti-correlation). Pair-wise connections with weak modulation ($|\Delta_{Z-corr.}| < 0.10$) were ignored. Finally, connections were grouped based on network classifications (sensorimotor, executive, limbic, and between network connections) and then visualized on coronal and volumetric representations of the rat template brain.

Optogenetic Constructs

For optogenetic experiments, neuronal opsin expression was achieved using adeno-associated viral vectors (AAV, serotype 5), encoding either a humanized variant of ChannelRhodopsin-2 (hChR2; H134R) fused to an enhanced yellow fluorescent protein (EYFP), or EYFP alone. Both constructs were placed under the calcium-calmodulin kinase II α (CaMKII α) promoter to target striatal neurons. Viral titers were approximately 5.0×10^{12} viral genome/ml. All viruses were obtained from the Vector Core at the University of North Carolina at Chapel Hill.

Histology

Following scan procedures, rats were deeply anesthetized with a 1-2 ml cocktail of pentobarbital sodium and phenytoin sodium (Euthasol) and transcardially perfused with saline followed by 10% formalin. Extracted brains were stored overnight in 10% formalin and transferred to a 30% sucrose solution (in DI water) for 2-3 days, until brains sunk to bottom of storage bottles. Brains were cut to 40 μ m thick sections on a freezing microtome and mounted on glass slides for fluorescent imaging. Vectashield mounting medium with DAPI stain (Vector laboratories, Item # H-1200) was used to provide a cell body counterstain. Slides were imaged using a Zeiss 780 confocal microscope.

2.3 Results

Electrode targeting accuracy within the NAc was verified using T₂-weighted anatomical scans (**Figure 2.1B**). Given the possibility of current spread to the shell region during DBS, we did not differentiate between these anatomical subdivisions in this study.

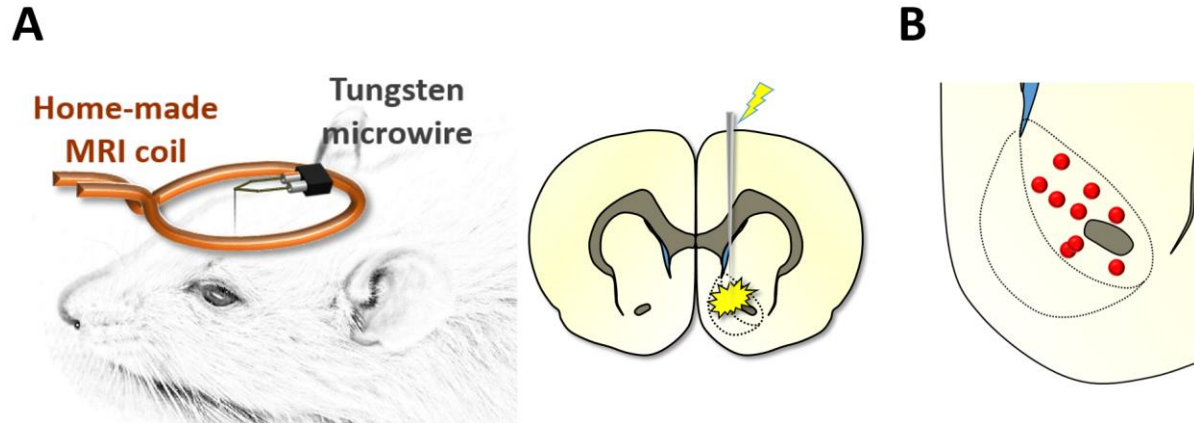


Figure 2.1. (A) Schematic of experimental imaging setup with a custom single loop surface coil and a tungsten microwire electrode. **(B)** Electrode tip mapping to the NAc for all electrical DBS subjects ($n = 9$). Tip placements were estimated using T_2 -weighted anatomical scans, which we deemed satisfactory given the relatively large size of the NAc (including anteroposterior distance), as well as the reduced electrode artifact.

To evaluate the downstream neural circuitry modulated by NAc-DBS at 130 Hz (300 μ A), CBV functional activation maps were generated using an evoked-fMRI acute stimulation paradigm (**Figure 2.2**). These maps revealed positive CBV responses to NAc-DBS in many brain regions with known executive and/or limbic functions; these included: amygdala, infralimbic cortex, lateral hypothalamus, NAc, prelimbic cortex, septum, ventral hippocampus, and ventral pallidum. Positive CBV changes observed along the electrode tract were time-locked to the stimulation period, and not present in DBS-fMRI studies conducted with the same electrode at different targets (e.g., thalamus) (132), strongly suggesting a neural origin. Minor CBV decreases were also detected in a small subregion of the dorsolateral striatum. Interestingly, although each of these regions has known anatomical connectivity with the NAc (in many cases as nonreciprocal glutamatergic inputs to the NAc) (177), anatomical connectivity alone was insufficient to predict responsive brain regions. For example, the ventral tegmental area, which is densely and reciprocally

connected to the NAc (178, 179), did not show detectable CBV modulation by 130 Hz NAc-DBS (see **Figure 2.2** and **Supplemental Figure S2.3**).

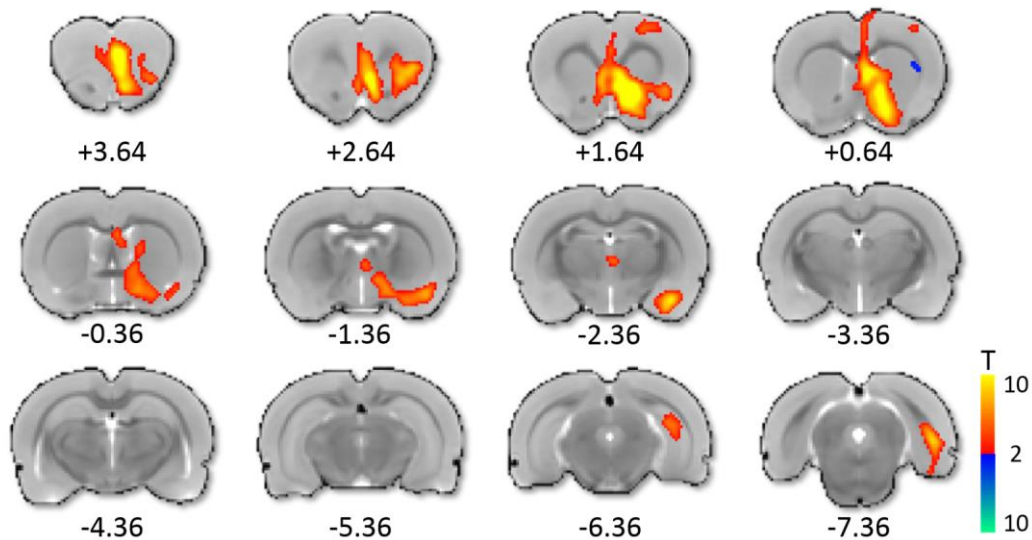


Figure 2.2. Functional CBV activation maps by 130 Hz NAc-DBS (300 μ A; $n = 5$). CBV modulation was largely ipsilateral to the stimulated hemisphere, was predominantly positive in direction, and included both cortical and subcortical CBV modulation. Notable regions demonstrating CBV increases included the prefrontal cortex, NAc, lateral hypothalamus, amygdala, ventral hippocampus and others. CBV decreases were also detected within a small region of the ipsilateral dorsal striatum. 12 slices were acquired in each scan, with numbers below slices denoting relative distance from bregma (in mm). Color bar denotes t score values obtained by GLM analyses, with a significance threshold of $p < 0.05$. Functional activation maps for all additional tested frequencies are located in **Supplemental Figures S2.4**.

Next, we undertook fcMRI experiments to study the effects of NAc-DBS over longer time periods (minutes). Previous electrophysiological and neuroimaging studies have provided evidence of network synchrony modulation by high frequency NAc-DBS (156, 180). Exploiting the capability of fcMRI to measure functional connectivity on a whole-brain scale, we mapped global network changes induced by NAc-DBS at 130 Hz (300 μ A). Mean correlation matrices were generated for each stimulus condition (Pre-DBS, DBS,

Post-DBS) across 90 anatomically-defined ROIs (45 ROI's per brain hemisphere) (**Figure 2.3A**). These ROIs were grouped into two pre-defined networks, based on our evoked fMRI findings (see Methods; NAc-DBS [#s 1-15] and Other [#'s 16-45]). A complete listing of ROIs and network groupings is provided in the **Figure 2.3** key and associated figure caption. For the Pre-DBS condition, bilateral connectivity was evident between homologous ROIs, and for certain structures appeared more robust (i.e. PLC, ILC, OFC, CC, Insula, Motor, etc). The presence of bilateral functional connectivity, as displayed in our datasets, represents a key feature of fcMRI (181). Except for a small number of ROIs (i.e. NAc↔OFC), within hemisphere connectivity was overall low in the Pre-DBS condition, possibly due to the short sampling period (5 mins per trial). However, during NAc-DBS of the RH NAc, within RH connectivity (i.e. ipsilateral to the DBS site) increased between many of the “NAc-DBS related network” ROIs, whereas there was little apparent modulation in the “Other network”. Between NAc-DBS network connectivity also appeared slightly modulated in the DBS condition but for a smaller number of ROIs (i.e. PLC, ILC). Post-DBS connectivity for the DBS-NAc network was similar, or perhaps intermittent to the pre-DBS / DBS conditions. Next, histograms were generated (**Figure 2.3B**) and fit as t-distributions for each stimulus condition, network, and connectivity grouping (within and between hemispheres) using average measures from the connectivity matrices. Consistent with the previous observations, NAc-DBS network connectivity within the RH was the only distribution to show enhanced positive correlations during DBS stimulation of the RH NAc. Repeated measures analyses of variance (rANOVA) were used to statistically validate these results across animals. For the NAc-DBS network, the stimulus condition (Pre-DBS, DBS, Post-DBS) and interaction between condition and connectivity (RH, LH, RH↔LH) were

significant ($p_{lb} \leq 0.05$); *Condition* $F(2,41) = 7.45$, $p_{lb} = 0.014$ and *Condition*Connectivity* $F(4,41) = 4.15$, $p_{lb} = 0.033$.

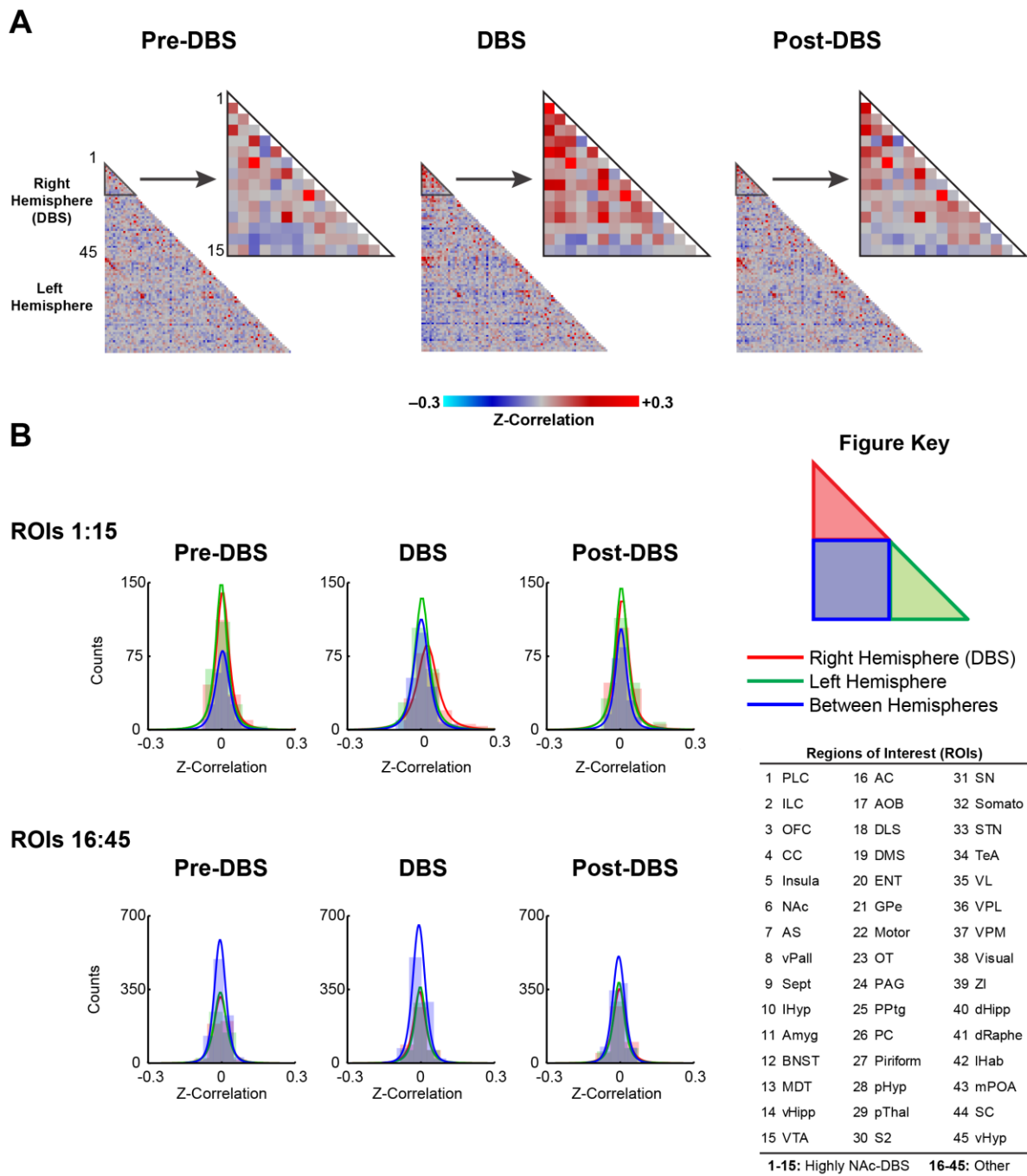


Figure 2.3. fcMRI modulation by 130 Hz NAc-DBS. **(A)** Mean correlation matrices ($n = 7$) for each stimulus condition (Pre-DBS, DBS, Post-DBS) using 45 regions-of-interest (ROIs, see Figure Key). ROIs were chosen *a priori*, with reference to anatomical regions described in a standard rat brain atlas (176). Note the presence of between-hemispheric regional connectivity (displayed as a red diagonal line) in all matrices. **(B)** Histograms and t-distribution fits for each stimulus condition, network (NAc-DBS [ROIs #s 1-15] and Other [ROIs #'s 16-45]) and connectivity grouping (within and between hemispheres) using correlation measures from the average correlation matrices. Abbreviations: **PLC:** Prelimbic Cortex; **ILC:** Infralimbic Cortex; **OFC:** Orbitofrontal Cortex; **CC:** Cingulate Cortex; **Insula:** Insular Cortex; **NAc:** Nucleus Accumbens; **AS:** Anterior Striatum; **vPall:** Ventral Pallidum; **Sept:** Septum; **IHyp:** Lateral Hypothalamus; **Amyg:** Amygdala; **BNST:** Bed Nucleus of the Stria Terminalis; **MDT:** Mediodorsal Thalamus; **vHipp:** Ventral Hippocampus; **VTA:** Ventral Tegmental Area; **AC:** Auditory Cortex; **AOB:** Accessory Olfactory Bulb; **DLS:** Dorsolateral Striatum; **DMS:** Dorsomedial Striatum; **ENT:** Entorhinal Cortex; **GPe:** External Globus Pallidus; **Motor:** Motor Cortex (Primary and Secondary); **OT:** Olfactory Tubercle; **PAG:** Periaqueductal Grey; **PPTg:** Pedunculopontine Tegmental Nucleus; **PC:** Parietal Cortex; **Piriform:** Piriform Cortex; **pHyp:** Posterior Hypothalamus; **pThal:** Posterior Thalamus; **S2:** Secondary Somatosensory Cortex; **SN:** Substantia Nigra; **Somato:** Primary Somatosensory Cortex; **STN:** Subthalamic Nucleus; **TeA:** Temporal Association Cortex; **VL:** Ventrolateral Thalamus; **VPL:** Ventral Posterolateral Thalamus; **Visual:** Visual Cortex (Primary and Secondary); **ZI:** Zona Incerta; **dHipp:** Dorsal Hippocampus; **dRaph:** Dorsal Raphe Nucleus; **IHab:** Lateral Habenula; **mPOA:** Medial Preoptic Area; **SC:** Superior Colliculus; **vHyp:** Ventral Hypothalamus.

Visualization of significantly (rANOVA, $p < 0.05$ uncorrected, $\Delta Z_{\text{Corr}} > 0.10$) enhanced (increased correlation) or suppressed (decreased correlation or increased anti-correlation) individual pair-wise connections grouped by functionally-defined networks (Sensorimotor, Executive, Limbic, and Between Network Connections) paralleled the above observations and revealed additional information that was not readily apparent in the original classification of the data (**Figure 2.4**; blue-suppressed, red-enhanced). Enhancement was primarily restricted to connections between RH limbic structures, however consistent suppression was also evident, mainly within the sensorimotor network and between limbic and motor regions. The sensorimotor network showed no significant enhancement, and moreover, the executive network was devoid of suppressed connections. Enhancement was

relatively robust (**Figure 2.4**, $\Delta Z_{\text{Corr}} > 0.20$ thick red lines) for the following connections; R-Nac \leftrightarrow R-Sept, R-PLC and R-ILC \leftrightarrow R-PLC. Additional analyses of fcMRI data are provided in **Supplemental Figures S2.5-6**.

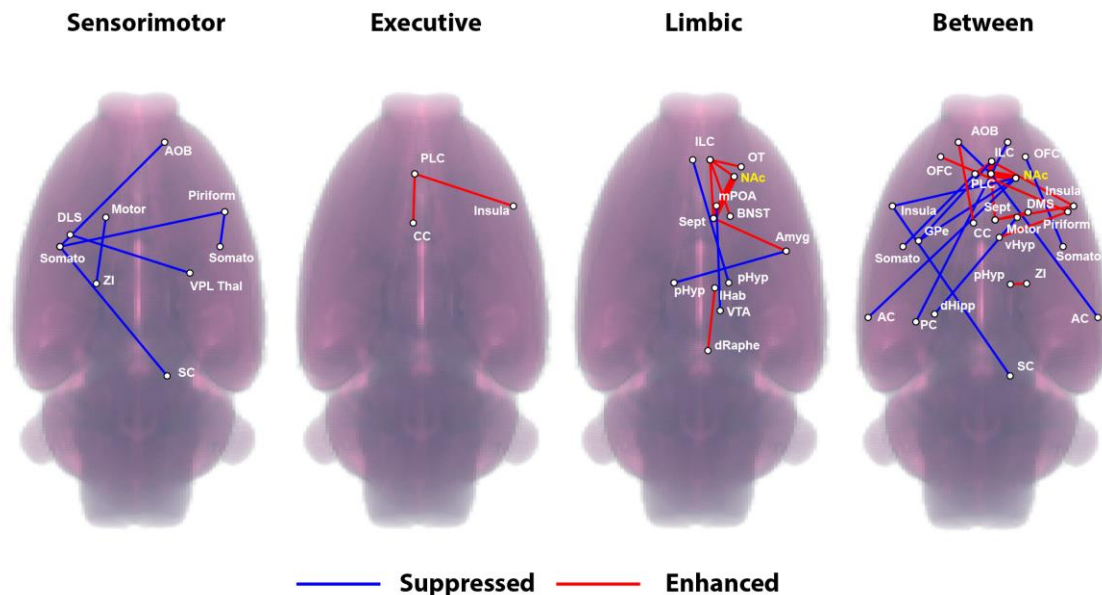


Figure 2.4. Network-level visualization of pair-wise fcMRI modulations during 130 Hz Nac-DBS. Significant (rANOVA, $p \leq 0.05$ uncorrected, $\Delta Z_{\text{Corr}} > 0.10$) enhanced (red) or suppressed (blue) individual pair-wise connections grouped by functionally-defined networks (Sensorimotor, Executive, Limbic, and Between Network Connections). Thick red lines represent $\Delta Z_{\text{Corr}} > 0.20$ at R-Nac \leftrightarrow R-Sept, R-PLC and R-ILC \leftrightarrow R-PLC.

To investigate the frequency-dependency of CBV responses to Nac-DBS, we next conducted additional evoked-fMRI experiments with five DBS frequencies (10, 40, 70, 130 and 200 Hz). To achieve a more robust measurement of the frequency effects and circumvent the issue of low DBS-fMRI sensitivity at low stimulus amplitude (182) this experiment was conducted using a slightly higher current intensity at 500 μ A. The results generated CBV response patterns that were qualitatively similar, yet more robust responses than 300 μ A (see **Supplemental Figure S2.4**). This current remains to be lower

than in many previously reported DBS-fMRI studies (*132, 140, 182, 183*), and we thus do not expect significant off-target effects. To further reduce bias towards characterizing off-target areas with this stronger current amplitude, we only evaluated anatomical ROIs that were significantly modulated with 300 μ A stimulation (at 130 Hz; **Figure 2.2**). This ROI-based analysis included two complementary measures of regional activity modulation: CBV time-courses and amplitudes; both are quantitative measures of percent CBV changes. CBV time-courses generated from 10 Hz NAc-DBS resulted in weak or no change in CBV (though see **Supplemental Figure S2.4** demonstrating sparse CBV increases in and surrounding the NAc), whereas all other frequencies resulted in region-specific CBV increases of similar amplitudes and rise/decay kinetics (**Figure 2.5A**). The absence of distal CBV responses with 10 Hz NAc-DBS is remarkable, as DBS at this stimulation frequency has been shown to generate robust downstream fMRI signals at other target locations (e.g., the ventroposteromedial thalamus) (*182*). In general, NAc-DBS induced sharp rises in CBV that returned to baseline values by the end of the test period (i.e., with 40 s of recovery). The largest CBV increases were detected in the NAc, infralimbic, and prelimbic cortices, each displaying maximal increases in CBV \sim 20% above baseline values. Among all regions showing significant and detectable responses, the ventral hippocampus displayed perhaps the weakest, with a maximal CBV increase of just over \sim 5% from baseline. Interestingly, the duration to peak CBV amplitude varied in a region-specific manner. For example, CBV continued to increase in the lateral hypothalamus and septum for the duration of the stimulation period, while CBV values peaked and decayed more rapidly in prefrontal cortex. Quantitative comparisons of CBV amplitude modulation by NAc-DBS at varying frequencies are shown in **Figure 2.5B**. One-way ANOVAs revealed a significant main effect

of NAc-DBS frequency on the amplitude of CBV change for all regions examined. Remarkably, post-hoc testing revealed that while 40-200 Hz NAc-DBS significantly increased CBV compared to the 10 Hz condition, no other significant frequency-dependent effects of NAc-DBS on CBV amplitude were noted. That is, increasing the frequency of NAc-DBS from 40 to 200 Hz, a five-fold difference, did not further modulate the functional circuit responses in the structures that we investigated. Critically, evoked responses were generally consistent across multiple stimulation trials, arguing against the possibility of stimulation-induced neural damage.

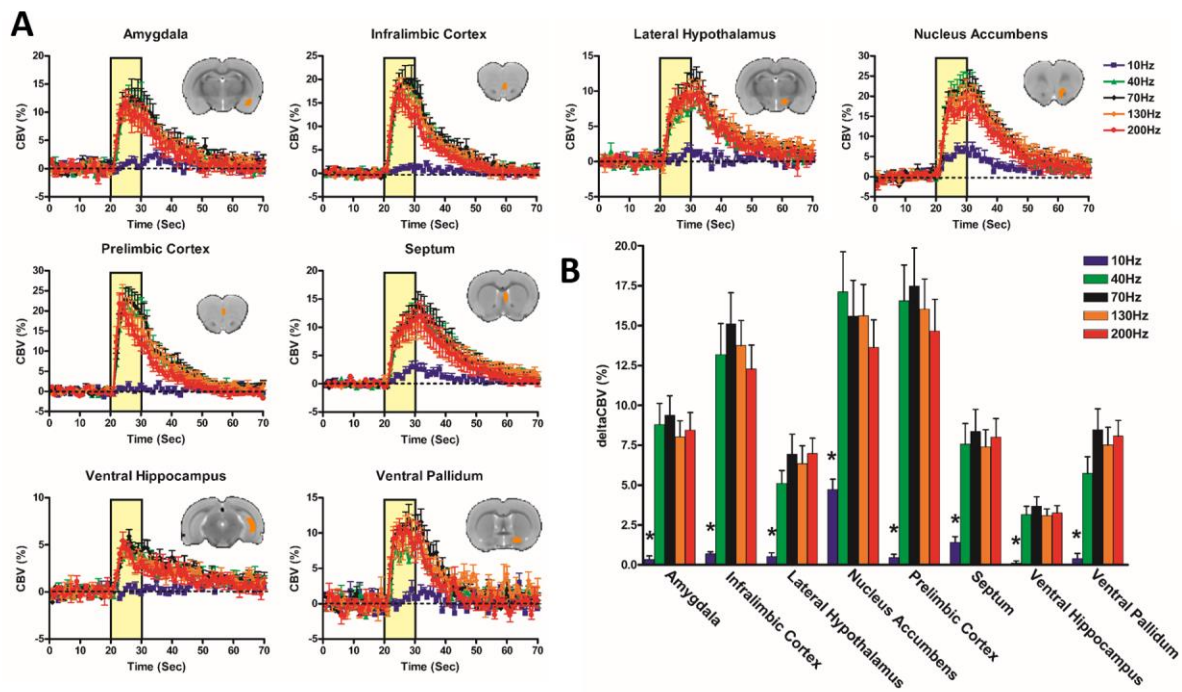


Figure 5. Temporal dynamics (**A**) and amplitudes (**B**) of CBV responses to NAc-DBS across five stimulation frequencies (10, 40, 70, 130, 200 Hz; $n = 8$ per frequency), demonstrating that CBV responses to NAc-DBS were largely stimulation frequency-insensitive. All subjects were scanned with 500 μ A DBS, except one subject with 600 μ A. CBV responses are expressed as a percent change from pre-stimulation baseline values. Amplitudes were calculated as mean percent CBV changes during stimulation epochs (10 seconds; scan frames 21-30). Anatomically-defined ROIs are highlighted as figure inserts in **5A** (Single slice shown; note that many ROIs encompassed multiple slices). * $p \leq 0.05$ for 10 Hz compared to

all other frequencies (no other statistically significant comparisons). Datapoints are presented as mean \pm SEM.

In addition to electrical stimulation, optogenetic tools are being increasingly exploited for mapping functional connectivity among neural circuits. Several studies have also employed optogenetic stimulation to elucidate potential mechanisms of therapeutic DBS action, including at the nucleus accumbens target (184). In preliminary experiments reported here, we explored the possibility of using optogenetic NAc stimulation to induce detectable downstream fMRI signals. This pilot experiment was performed in rats that received viral injections of an adeno-associated virus encoding ChR2 under the neuron-specific CaMKII α promoter. A representative example of virally-mediated ChR2 expression in NAc neurons is provided in **Figure 2.6A**. Optogenetic stimulation at 40 Hz evoked a local positive CBV signal in the NAc, with no significant CBV modulation observed outside the target region (**Figure 2.6B-C**). Ongoing studies in our laboratory using a completely identical experimental setup and analysis pipeline have revealed robust optogenetic-induced responses in downstream areas far from the stimulation site (172, 173). Thus, we are confident that our findings do not reflect a technical failure to manipulate NAc neurons optogenetically.

A recent study has demonstrated hemodynamic changes following blue light laser stimulation (50% duty cycle) in naïve rat brain, possibly due to a laser heating artifact (185). To evaluate the possibility of such an artifact as the source of the observed optogenetic response at the NAc, we repeated our optogenetic-fMRI experiments in control rats expressing an inert EYFP fluorophore in the NAc. In these animals, no significant CBV modulation by NAc-DBS was observed (**Figure 2.6B-C**). It is worth noting that our laser

pulse duration was substantially shorter than that previously reported to induce laser artifacts, likely explaining the absence of such a response caused by laser heating. Local heating artifacts in optogenetic-fMRI experiments have since been examined in greater detail, including suggested control experiments to rule out such artifacts as causal in fMRI signal generation (186).

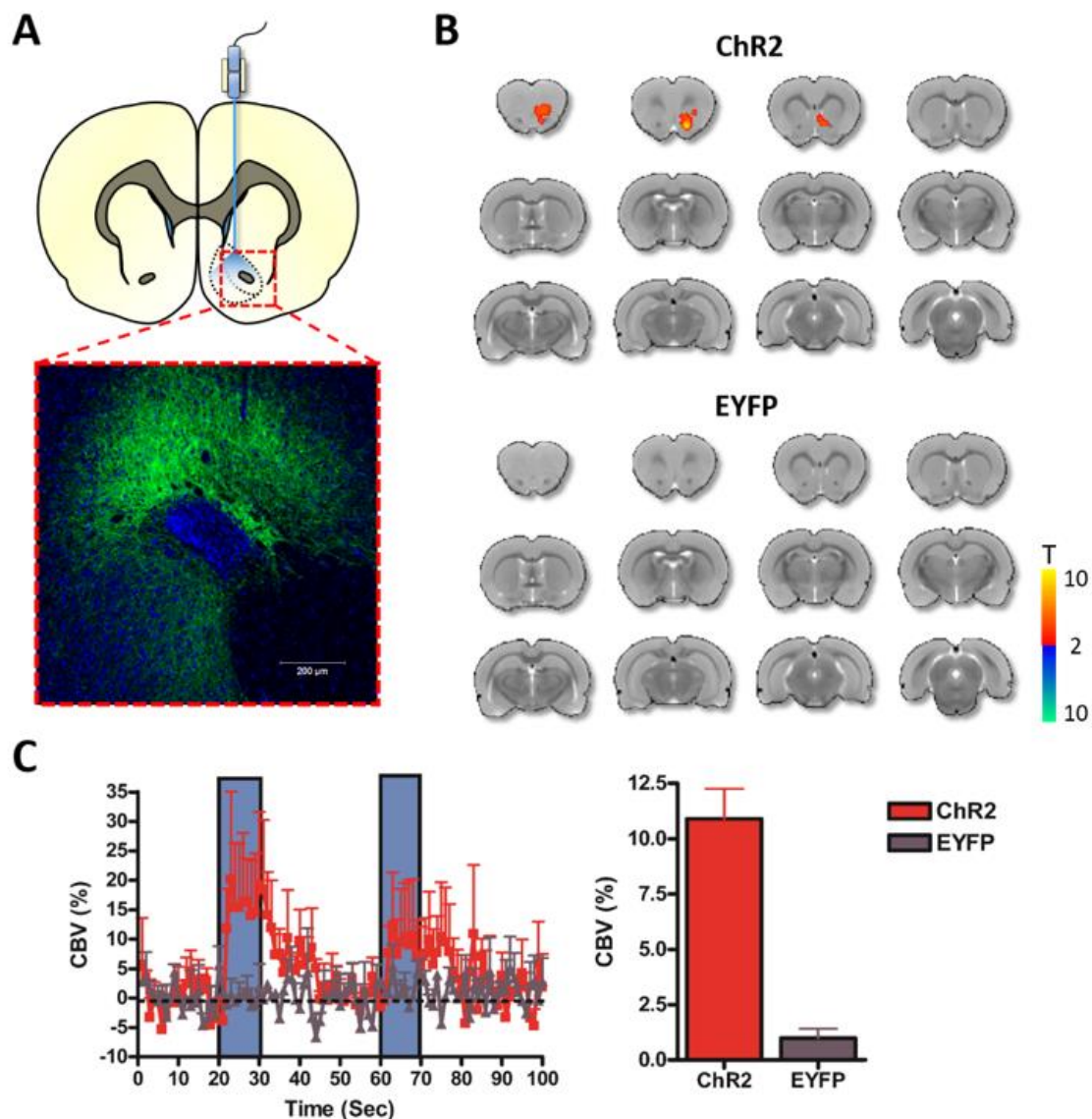


Figure 2.6. Optogenetic stimulation at NAc evokes local CBV increases. **(A)** Schematic of optogenetic stimulation at NAc (top), representative confocal image confirming ChR2 expression (green) in the NAc (bottom). Counterstain is DAPI (blue). ChR2 expression

appeared strongest in the core subregion of the NAc. **(B)** Functional CBV responses induced by 40 Hz optogenetic stimulation at NAc in animals expressing ChR2 or EYFP (AAV5 using the CaMKII α promoter; $n = 4$ and 2 , respectively). Note that optogenetic stimulation of the NAc resulted in CBV increases locally within the stimulated region, with no detected downstream responses. No responses were observed in EYFP subjects. Anteroposterior slice coordinates are as described for **Figure 2.2**. Temporal CBV dynamics **(C)** and amplitudes **(D)** within the NAc during local optogenetic stimulation. Stimulation-evoked CBV amplitude changes were calculated as described in Methods.

2.4 Discussion

In this study, we performed multimodal fMRI procedures to identify neural circuitry modulated by NAc-DBS in a healthy rat model. Evoked fMRI with electrical DBS uncovered a broad range of cortical and subcortical regions displaying stimulation-induced CBV increases, including prefrontal cortex, lateral hypothalamus, amygdala, septum, and ventral hippocampus. fcMRI provided corroborative evidence of robust network modulation by NAc-DBS, including suppression of sensorimotor and enhancement of executive and limbic network connectivity. Lastly, we performed opto-fMRI with selective and direct stimulation of NAc neurons, showing time-locked CBV increases exclusively localized in the NAc during 40 Hz optical stimulation.

Although high frequency DBS is generally reported to locally silence neuronal activity (*187, 188*), we noted only CBV increases in the target region (i.e., the NAc) across all tested stimulation frequencies. This finding is consistent with a number of human neuroimaging studies reporting increases in hemodynamic responses or glucose metabolism in the subthalamic nucleus (STN) during STN-DBS (*152*). Notably, each of these studies (including our own) uses indirect measures of neuronal activity, and thus this seeming paradox may possibly be explained by an uncoupling of hemodynamic responses from neuronal spiking during high frequency stimulation. DBS may induce both

depolarization blockade and augmented presynaptic activity, either of which may potentially increase local metabolic demand in the absence of somatic spiking (189). In this context, it is also interesting to note several reports of local increases in c-fos expression following DBS of the NAc, STN, or pedunculopontine tegmental nucleus in rats (190-192). Future studies may determine the nature and extent of this possible uncoupling, which has strong implications for the interpretations of neuronal activity based on indirect experimental measures such as fMRI or immediate early gene expression.

Complementing our evoked-fMRI findings of direct limbic circuit modulation by NAc-DBS, fcMRI measurements revealed robust enhancements in functional connectivity between many of these same regions. More generally, limbic and executive network connections were primarily enhanced but those in the sensorimotor network were largely suppressed. These findings suggest that NAc-DBS modulates multiple functional network domains, spanning the entire brain. Although these functional connectivity maps alone do not allow for causal inferences relating to the therapeutic mechanism of NAc-DBS, they should provide an invaluable resource for the generation of future, hypothesis-driven DBS studies.

A central tenet of DBS therapy is its dependence upon high stimulation frequencies. One widely held hypothesis of DBS action posits that high frequency stimulation masks pathological endogenous circuit activity, thus creating an “informational lesion” at the DBS target (although other mechanisms have also been posited) (193-195). We were thus surprised to find that the functional activation profile obtained by NAc-DBS in rats was remarkably insensitive to a wide range of stimulation frequencies; indeed, 40 Hz stimulation modulated CBV across all tested areas in a manner quantitatively similar to all

higher frequencies tested, including 200 Hz. Although we used a healthy rodent model, precluding behavioral tests of DBS efficacy, our evoked-fMRI results highlight strong parallels in circuit modulation by either moderate or high frequency stimulation of the NAc. Further, a recent preclinical study of NAc-DBS for cocaine addiction reported similar attenuation of reinstated drug-seeking behavior at 20 or 160 Hz, suggesting that some behavioral effects of NAc-DBS may also be frequency-insensitive (158). The frequency sensitivity of symptom amelioration by NAc-DBS would be interesting to study in the clinical setting, particularly in light of the possibility of prolonging the battery life of DBS pulse generators using lower frequency stimulation protocols.

In this study, we have also provided preliminary data concerning the fMRI signal pattern generated by optogenetic stimulation of the NAc in a small number of subjects. We were surprised to discover that, in our setup, optogenetic NAc stimulation evoked detectable CBV increases solely within the NAc, whereas identical parameters used at other target regions revealed significant downstream responses (172, 173). The lack of distal responses in the present experiment is particularly perplexing in that neural activity within the target region itself was clearly and robustly modulated by optogenetic stimulation. The reason for such large differences in circuit modulation patterns between optogenetic and electrical NAc stimulation is unclear, although several possibilities exist. First, stimulus intensity differed between optogenetic and electrical DBS in this study, which may contribute to the differing activation patterns. Second, although we have assumed that both electrical and optogenetic stimulation delivered at 40 Hz would activate (rather than suppress) neural circuits, this was not formally tested. Another possibility concerns more fundamental differences between these stimulation approaches, such as the confinement of

optogenetic stimulation to the opsin-expressing neurons and their efferent fibers.

However, we also cannot entirely rule out the possibility that Chr2 was expressed in a small population of non-neuronal cells. The most likely explanation for our findings, in our opinion, is that most of the circuits recruited by NAc-DBS arose from antidromic activation of axons or fibers of passage. In this scenario, no modulation of these circuits (i.e., those that send nonreciprocal afferents to the NAc) would be expected during optogenetic NAc stimulation. Future studies, more comprehensively mapping fMRI (and electrophysiological) responses to optogenetic vs. electrical NAc stimulation, may be undertaken to more directly test this hypothesis .

There are several limitations to the present study to consider. First, although the NAc is generally considered to be comprised of two related, yet distinct subdivisions (core and shell) each with distinct circuit features (46, 177). We did not distinguish between these two areas in our experiments. Indeed based on the obtained functional response profiles, both regions were likely recruited by our stimulation paradigm. The core and shell subregions are both candidate therapeutic targets for neuropsychiatric DBS, but the efficacy of each may strongly depend upon the disorder being treated. For example, NAc-DBS for OCD generally targets the core region (196, 197), while some preclinical studies suggest that the shell is more effective for addictive disorders (160, 191, 198). Other behavioral phenotypes, such as quinpirole-induced checking behavior (a pharmacological model of OCD symptoms), are similarly influenced by NAc-DBS of the core or shell (199). Further studies are necessary to elucidate the downstream circuitry that confers unique therapeutic properties of DBS at either NAc subdivision.

A second major limitation of our study was the usage of dexmedetomidine sedation (168, 181), which may alter the responsivity of neural circuits to the effects of DBS. Related to this point, we were unable to reliably achieve robust fMRI responses with current amplitudes below 300 μ A (data not shown), and thus our experiments relied upon higher amplitudes than those generally used in preclinical DBS studies in awake rodents (typically 100-150 μ A) (156, 157, 160), although amplitudes higher than 150 μ A have been reported for studies in both awake and anesthetized states (159, 200). We postulate that the relatively higher current amplitudes needed for DBS effects in our model may have been necessitated by the sedation state, the detection sensitivity of our fMRI measurements, or both.

A third limitation concerns the use of an acute stimulation paradigm, which was necessary in the context of our experimental MR setup. Similar OFF-ON-OFF paradigms are traditionally used in DBS-fMRI studies (140, 141, 155, 201), although they may provide a biased perspective on DBS-evoked changes in functional connectivity. A recent report by Ewing and Grace highlights the importance of studying DBS network effects under chronic stimulation conditions (156). In that study, local field potentials (LFPs) were recorded in multiple brain regions of rats receiving continuous NAc-DBS for a period of 5 days. Some of the observed DBS-induced network changes were transient, including enhanced delta power in the mediodorsal thalamus and orbitofrontal cortex, whereas other network effects emerged over time (e.g., decreased alpha power in the mediodorsal thalamus). This work highlights the importance of studying DBS effects over more translationally-relevant timespans (days or weeks, if experimentally feasible). fcMRI, which does not require

within-session baseline (“OFF”) periods, provides an ideal experimental measure for future longitudinal examinations of DBS effects across time and brain regions.

In the present study, we identified a robustly recruited network of cortical and subcortical circuits modulated by NAc-DBS, many of which are likely to be antidromically-stimulated. Remarkably, the extent of this circuit modulation was relatively frequency-insensitive, as demonstrated by our evoked-fMRI findings. Collectively, our findings should facilitate the understanding of DBS mechanisms and mapping of therapeutic circuits at this important clinical target. Future NAc-DBS fMRI studies should examine the circuit- and network-level responses to therapeutic stimulation in neuropsychiatric disease models, wherein pathology-specific circuit disruptions (and putative amelioration by DBS) may be explored.

CHAPTER 3: FUNCTIONAL CIRCUIT MAPPING OF STRIATAL OUTPUT NUCLEI USING SIMULTANEOUS DBS-FMRI

3.1 Introduction

The striatum represents the major input nucleus of the basal ganglia, critical for the processing and regulation of motor, cognitive, and limbic functions. Striatal output pathways within the basal ganglia are classified as “direct” or “indirect”, based on neurochemical phenotype and axonal projection patterns. Specifically, direct pathway striatal neurons express the D1 dopamine receptor and project to the substantia nigra pars reticulata (SNr) and/or internal globus pallidus (GPi) (i.e., the canonical basal ganglia outputs), whereas indirect pathway striatal neurons express the D2 dopamine receptor and innervate the external globus pallidus (GPe). Both the direct and indirect pathways ultimately converge upon thalamocortical relays, through direct innervation of the basal ganglia outputs (SNr/GPi), or a polysynaptic route (GPe -> STN), respectively. According to long-upheld models of the basal ganglia, these pathways are functionally antagonistic; the direct pathway activates thalamocortical circuits, whereas the indirect pathway facilitates their suppression (via disinhibition of the SNr/GPi) (38, 202).

In recent years, this relatively simplistic framework of direct/indirect pathway function has come under increasing scrutiny (22, 42, 115, 116, 203-205). Although evidence continues to support the notion of functional antagonism between these pathways (36, 39, 206), additional anatomical and functional studies have identified unanticipated circuit

connectivity in both the SNr and GPe (among other basal ganglia nuclei). Recent examples in the GPe include the identification of a pallidocortical projection that entirely bypasses thalamic relays to modulate frontal cortex (76, 77), as well as pallidostriatal innervation by so-called “arkypallidal” GPe neurons (70, 72). The SNr, generally conceptualized as an inhibitory nucleus, contains a subset of glutamatergic neurons recently mapped to innervate and excite the reticular thalamus, a higher-order non-relay region (207). The functional roles of these novel circuit elements are likely complex and not easily predicted. Experimental approaches that allow for the large-scale characterization of functional circuit connections will greatly facilitate our understanding of SNr and GPe connectivity, further elucidating the functional roles of both traditional and newly-established circuits.

Functional magnetic resonance imaging (fMRI) represents a powerful tool to study neural circuit modulation on a global scale. When combined with neural stimulation approaches (e.g., deep brain stimulation; DBS), fMRI allows for the relatively unbiased identification of brain areas functionally interconnected with the stimulation target (133, 140, 146, 152, 155, 163, 182, 207-209). Electrical DBS is notable as a neural stimulation method for its ability to modulate activity within both inputs and outputs of the target nucleus (the former through antidromic signal propagation), although it does lack cell-type specificity and is also capable of affecting fibers of passage (171). In addition to identifying putatively connected areas, DBS-fMRI might also shed light on their functional excitatory and/or inhibitory relationships (based on whether the hemodynamic change is positive or negative). Importantly, both the recruitment of select circuits, as well as the directionality of their fMRI responses, may be strongly contingent upon stimulation frequency. For example, low frequency (10 Hz) electrical stimulation of the ventrolateral thalamus in pigs

generated a positive blood-oxygen-level-dependent (BOLD) response in motor cortex, whereas high frequency (130 Hz) stimulation evoked a negative BOLD response in the same region (210). Thus, in varying stimulation parameters, DBS-fMRI can shed light on the tuning properties of functionally connected circuits. To our knowledge, neither the SNr nor GPe have previously been studied by DBS-fMRI.

In the present study, we employed simultaneous DBS-fMRI in the normal rat to map the functional circuits of the SNr and GPe. These areas represent the major striatal output nuclei of the rat direct and indirect pathways, respectively. Evoked-fMRI revealed cerebral blood volume (CBV) modulation by GPe- or SNr-DBS in a diverse complement of both overlapping and distinct brain regions, including convergent and unexpected CBV decreases within striatum, and GPe-DBS-evoked positive modulation of frontal cortex. Functional connectivity, measured with functional connectivity fMRI (fcMRI) (122, 211), was preferentially modulated in the hemisphere ipsilateral to SNr- or GPe-DBS, and readily reversed following cessation of stimulation. Notably, both circuit and network modulation by DBS at both targets (measured by evoked- and fcMRI, respectively) was sensitive to stimulation frequency.

3.2 Materials and Methods

Subjects

Thirteen adult male Sprague-Dawley rats (300–500 g body weight; Charles River Laboratories, Wilmington, MA, USA) were used in this study. All procedures were performed in accordance with the National Institutes of Health Guidelines for Animal Research (Guide for the Care and Use of Laboratory Animals) and approved by the University of North Carolina Institutional Animal Care and Use Committee. Animals were

housed under environmentally-controlled conditions (12 h normal light/dark cycles, 20-23°C and 40-60% relative humidity), with food and water provided *ad libitum*.

DBS Electrode Implantation Surgery

Rats were anesthetized using nosecone-supplied isoflurane (1.5-2%), and head-fixed within a stereotaxic frame (Model 962, Kopf Instruments, Tujunga, CA, USA). Following head shaving and exposure of the skull, four small burr holes were drilled: three for the positioning of MR-compatible miniature brass screws (Item #94070A031, McMaster Carr, Atlanta, GA, USA) and one for the insertion of a bipolar DBS electrode. Each electrode was custom-made using two-channel tungsten microelectrodes (A-M Systems, WA, U.S.A.), with a 50 µm diameter (single lead), as previously described (132). These electrodes were fully insulated with polyimide except at the tips, and the leads were adhered for direct contact using a saturated sucrose solution. The *in vitro* impedance of these electrodes was previously measured as 18-22 kΩ at 1 kHz (132).

Electrodes were implanted targeting either the right SNr or GPe ($n = 6$ and 7 , respectively). Stereotactic implantation coordinates were generated using a standard rat brain atlas (176), and are described as follows, in reference to bregma (anteroposterior, AP; mediolateral, ML) and cortical surface (dorsoventral, DV): SNr (AP -5.5 mm, ML +2.2 mm, DV -7.7 mm); GPe (AP -0.96 mm, ML +2.8 mm, DV -5.8 mm). Following electrode implantation, the placement was sealed using dental acrylic and the wound site was further protected with surgical sutures. A post-surgical recovery period of at least 24 hours was given prior to fMRI acquisition for each subject.

Functional MRI

The DBS-fMRI experimental protocol is illustrated in **Supplemental Figure S3.1**. Detailed fMRI procedures, including animal handling and scan optimization, are as described in Chapter 2 Methods.

Deep Brain Stimulation (DBS)

Simultaneous DBS with CBV fMRI was acquired in the same manner for all subjects, with bipolar and uniformly-distributed unilateral stimulation of the SNr or GPe. Each stimulation period consisted of a series of TTL-triggered biphasic, charge-balanced square-wave pulses with a pulse width of 500 μ s and a stimulation intensity of 300 μ A. A 90 second block design paradigm was implemented, consisting of a 20 second baseline period (stimulation OFF) followed by 10 seconds of stimulation ON, and an additional 60 seconds of rest (stimulation OFF). An additional rest period of at least two minutes was given between each DBS scan to allow for neurovascular recovery. Stimulation frequencies were varied in a pseudo-randomized order (10, 40, 70, 130, 200 and 400 Hz), and each DBS frequency scan was repeated 5-times per rat for within-subject/session averaging (see Section 2.5).

Immediately following evoked-fMRI scan acquisition, fcMRI scans were conducted in each subject. These scan series consisted of five, 5 minute scans during which either no stimulation or continuous DBS was applied (OFF and ON, respectively; ON consisted of stimulation of 300 μ A, 500 μ s pulse width, varied frequency). The fcMRI scans were conducted in succession without rest periods in the following order: Rest₁, Stim 40 Hz, Rest₂, Stim 130 Hz, and Rest₃.

Evoked-fMRI Data Processing and Statistical Analyses

Preprocessing and image analysis was performed using SPM codes and custom-written Matlab (MathWorks Inc., Natick, MA). Details concerning functional response map generation are as described in Chapter 2 Methods.

For temporal analysis of DBS-evoked CBV changes, 3-dimensional regions of interest (ROIs) were defined *a priori* according to anatomical structural boundaries (174, 176), and applied onto the coregistered data. The ROIs were chosen according to the anatomical areas showing statistically significant modulation in the functional response maps. Nineteen ROIs were identified for analysis, all ipsilateral to the DBS target unless otherwise noted: cingulate cortex, dorsolateral striatum (ipsi- and contralateral), dorsomedial striatum (ipsi- and contralateral), GPe, infralimbic cortex, motor cortex, nucleus accumbens, orbitofrontal cortex, pedunculo pontine tegmental nucleus, posterior hypothalamus, prelimbic cortex, SNr, somatosensory cortex, superior colliculus, ventral tegmental area, ventrolateral thalamus, and zona incerta (see **Supplemental Figure S3.2**). The baseline and stimulus evoked ΔR_2^* values were calculated as described in Chapter 2 Methods. For each ROI, the CBV signal time-course was plotted across all 90 time frames.

DBS-evoked changes in CBV amplitude were also compared across stimulation frequencies and ROIs. Stimulus-evoked CBV responses were averaged across the stimulation period for each DBS frequency and ROI. These data are presented as mean \pm SEM. Statistical comparisons of DBS frequency effects on Δ CBV for each ROI were conducted using Graphpad Prism software (San Diego, CA). Two-tailed, one-way repeated measures ANOVA (rANOVA) tests with Tukey post-hoc analyses were conducted to evaluate frequency-dependent responses. Significance level was set at $p < 0.05$.

fcMRI Data Processing and Statistical Analyses

Functional connectivity MRI datasets were preprocessed using the Analysis of Functional NeuroImages software suite (AFNI v2011-12-21-1014). The workflow included discarding the first 20 volumes, slice-timing correction, motion correction, alignment to a pre-existing high-resolution T₂-weighted template, spatial smoothing (Gaussian kernel FWHM = 1.5 mm), band-pass filtering (0.001 – 0.5 Hz), and regression of whole brain signal and the six motion parameters. The number of volumes discarded was increased from the traditional number (approximately 3-10) in order to ensure DBS-related changes from the initial stimulation were minimized. Furthermore, warping in the alignment procedure was limited to shifts and rotations to avoid unnecessary shearing and scaling of brain regions with signal drop-out associated with the DBS electrode. fcMRI analyses were conducted using the temporal correlation method. Fisher-Z transformed correlation matrices were generated using the average functional time series extracted for each region-of-interest (ROI) in the template atlas. Ipsilateral and contralateral hemispheres ROIs were analyzed separately yielding correlation matrices detailing mean within and between hemisphere connectivity (SNr: $n = 6$, GPe: $n = 7$). Individual connections were further evaluated across animals using repeated measures ANOVA models and categorized based on direction of effect. For each significant pairwise connection (rANOVA, $p < 0.01$) a basic correlation analysis was carried using a tent function and the resulting sign was used to categorize connections as either enhanced (increased correlation) or suppressed (increased anti-correlation). Each set of significantly modulated connections (enhanced or suppressed) was then reanalyzed using post-hoc ANOVAs in order to test the overall effect of condition:

Rest₁₋₃, 40 Hz, and 130 Hz. Pair-wise connections with weak modulation ($|\Delta Z\text{-corr.}| < 0.10$) were ignored. Significant main-effects were followed by pair-wise comparisons to test for significant differences between conditions. Furthermore, in order to assess the potential contribution of global signal regression (GSR), these analyses were repeated using data without GSR. The global signal across conditions and animals was also compared. Specifically, we calculated the pairwise Fisher's Z-correlation of the global signal across stimulation conditions (Rest₁₋₃, 40 Hz, and 130 Hz) and animals resulting in 10 pairs per animal. These values were then analyzed using repeated measures ANOVA to determine if there was an overall effect, i.e. a difference in the temporal correlation, which would suggest that one or more of the global signals vary as a function of condition. Finally, connections were grouped based on network classifications (sensorimotor, executive, limbic, and between network connections).

3.3 Results

The setup for the surface coil and implanted tungsten microwire is shown in Figure 1A. Electrode tip placements within the SNr and GPe were verified for each subject using T₂-weighted RARE anatomical images using methods described previously (132, 133, 140) (Figure 3.1B-C). Animals with electrode placements outside of the target regions were discarded from the study and excluded from all further experimental analyses.

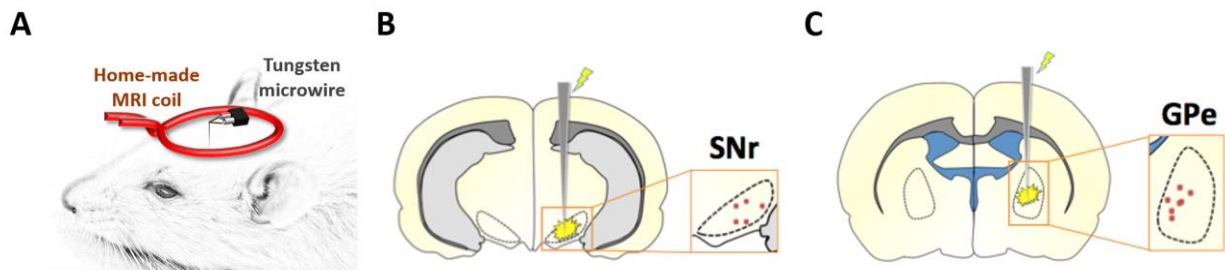


Figure 3.1. (A) Schematic of the experimental setup, including custom surface coil and microwire DBS electrode. **(B-C)** Electrode tip placements within the SNr **(B)** and GPe **(C)** of all experimental subjects. Tip placements were estimated using T₂-weighted anatomical scans, which we deemed satisfactory given the relatively large size (including anteroposterior distance) of our targets, as well as the minimal electrode artifact.

Evoked fMRI

Both SNr- and GPe-DBS produced significant and frequency-dependent CBV responses in several brain structures both within and outside the basal ganglia (Functional response maps: **Figure 3.2:** 40 and 130 Hz; **Supplemental Figures S3.4-5:** all other frequencies; **Supplemental Figure S3.3:** 130Hz SNr-DBS displayed on EPI). In addition to generating functional response maps, CBV time-courses for each DBS target and stimulation frequency were calculated for 19 anatomical ROIs (**Figures 3.3-4 and Supplemental Figures S3.6-7**).

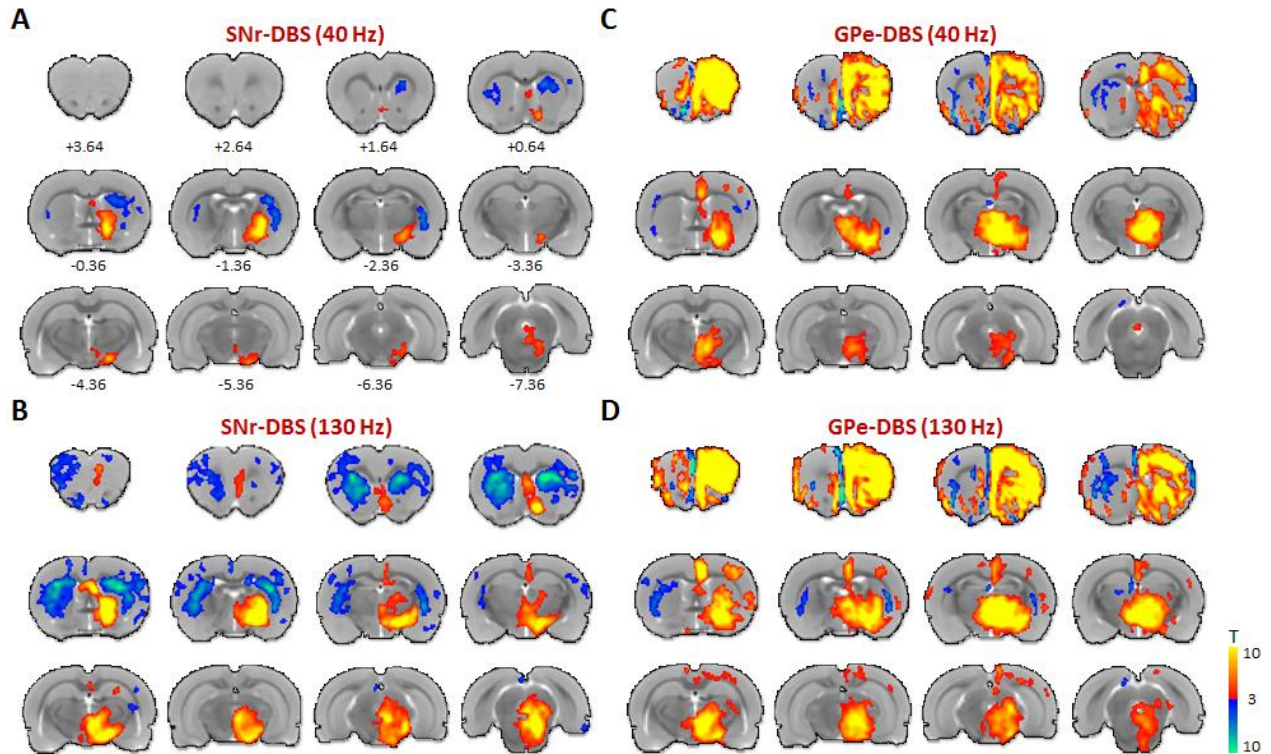


Figure 3.2. Functional activation maps of CBV modulation by SNr- and GPe-DBS. Two DBS stimulation frequencies are shown for each target: SNr- DBS at 40 or 130 Hz (**A** and **B**, respectively), GPe-DBS at 40 or 130 Hz (**C** and **D**, respectively). Notable observations include CBV decreases in the striatum at both targets, as well as large, ipsilateral frontal cortical modulation by GPe-DBS. At both targets, stimulation responses were largely ipsilateral and stronger at 130 Hz compared to 40 Hz. 12 slices were acquired in each scan, with numbers below slices denoting relative distance from bregma (in mm). Color bar denotes t score values obtained by GLM analyses, with a significance threshold of $p < 0.05$. Functional activation maps for all additional tested frequencies are located in **Supplemental Figures S3.4-5**.

10 Hz DBS at either target produced no significantly modulated voxels, including within the electrode target region. In contrast, significant and extensive CBV modulation was noted at all other frequencies tested (40-400 Hz). The spatial pattern of CBV modulation was qualitatively similar across stimulation frequencies, and in some respects also similar between SNr and GPe stimulation targets. For example, both GPe- and SNr-DBS resulted in CBV changes predominantly ipsilateral to the stimulation site, with the exception of the dorsal striatum, which was bilaterally modulated by DBS at either target.

SNr-DBS produced negative CBV changes bilaterally in striatum, whereas GPe-DBS produced a pattern of positive and negative CBV changes in the ipsi- and contralateral dorsal striatum, respectively. Also of note, a “double peak” of CBV modulation was a characteristic response to DBS in certain regions, including the ipsilateral somatosensory cortex (both DBS targets), and dorsal striatum (SNr-DBS) (**Figures 3.3-4**), possibly due to the recruitment of two distinct circuitries or a delayed neurotransmission effect. Future work is necessary to confirm the neuronal mechanism(s) underlying this double-peak response.

SNr-DBS (40-400 Hz) evoked positive CBV changes in multiple basal ganglia nuclei (GPe, substantia nigra striatum), as well as additional areas intimately tied to the basal ganglia (pedunculopontine tegmental nucleus, zona incerta, ventral tegmental area) (see **Figure 3.3** and **Supplemental Figure S3.6**). Of all regions examined, the substantia nigra showed the largest CBV changes (nearly 30% CBV increases at 200 or 400 Hz DBS). In stark contrast to GPe-DBS, frontal and prefrontal cortical modulation by SNr-DBS was relatively sparse; functional activation maps revealed spatially restricted vasodilation (e.g., in cingulate cortex), as well as contralateral vasoconstriction in prefrontal cortex (most apparent at 130 Hz). However, a closer examination of this data by means of CBV traces revealed that many of these areas (e.g., motor, somatosensory, prelimbic cortices) were likely positively modulated by 200 Hz SNr-DBS, albeit with a long delay (and thus not detected with our functional activation maps). Also of note, the superior colliculus, which receives direct innervation from the SNr (1, 212), had little to no detectable CBV changes during SNr-DBS.

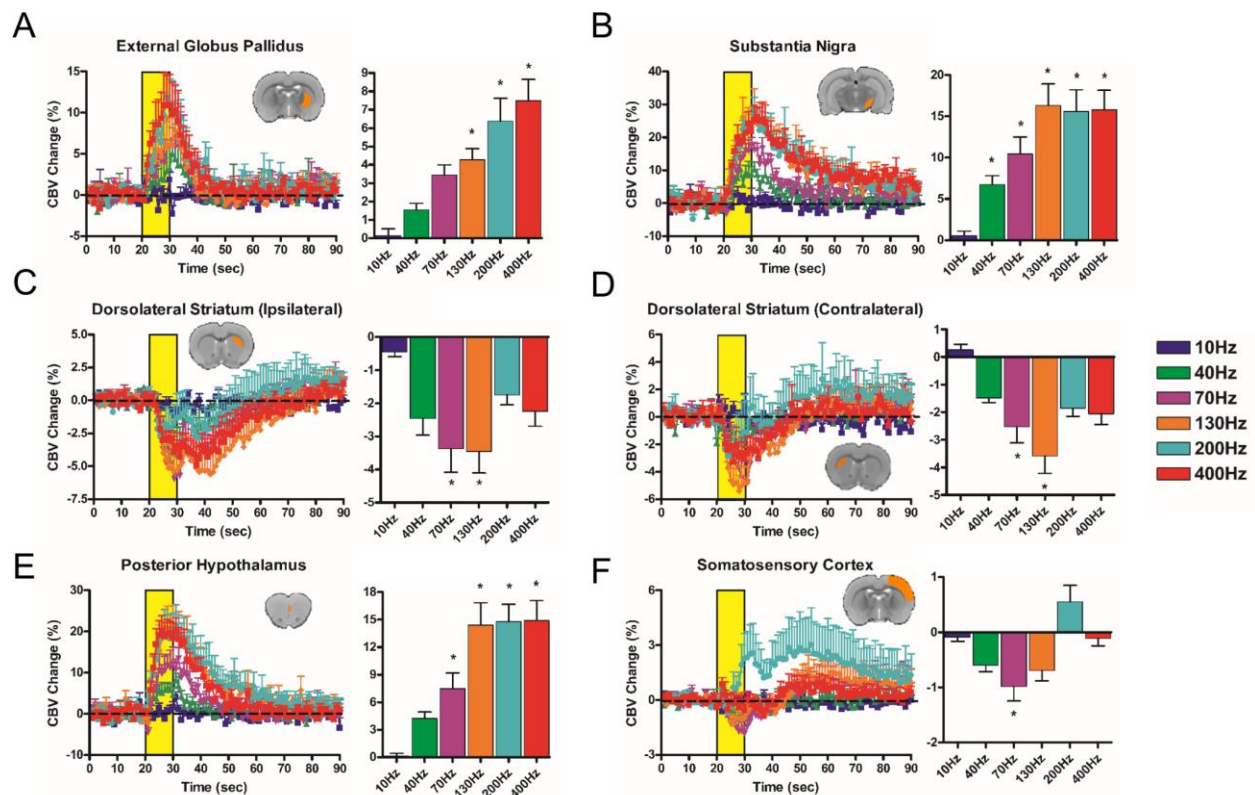


Figure 3.3. SNr-DBS evoked CBV changes at select, anatomically-defined regions of interest. CBV traces (10-400 Hz; yellow bar denotes stimulation epoch; note different Y axis scales across ROIs) are accompanied by bar graphs displaying percent changes in CBV amplitude changes during the stimulation period (mean \pm SEM CBV values for the DBS stimulation period). *'s denote significant differences in CBV amplitude from 10 Hz ($p < 0.05$). Insert depicts representative slice example for each pre-defined ROI (note that most ROIs encompassed multiple slices). Unless otherwise denoted, all ROIs are ipsilateral to the DBS hemisphere. **(A)** External globus pallidus **(B)** Substantia nigra **(C)** Ipsilateral dorsolateral striatum **(D)** Contralateral dorsolateral striatum **(E)** Posterior hypothalamus **(F)** Somatosensory cortex. Additional ROIs (total = 19) are located in **Supplemental Figure S3.6**.

During GPe-DBS (40-400 Hz), robust CBV increases were observed in ipsilateral frontal and prefrontal cortices, including cingulate, motor, prelimbic, infralimbic, and orbitofrontal cortices. A wealth of subcortical areas also showed positive CBV responses, including the substantia nigra, nucleus accumbens, ventral tegmental area, zona incerta, and others (see **Figure 3.4** and **Supplemental Figure S3.7**). Of all regions examined, peak

CBV responses to GPe-DBS were strongest in orbitofrontal cortex, reaching nearly 30% CBV increases with 400 Hz stimulation.

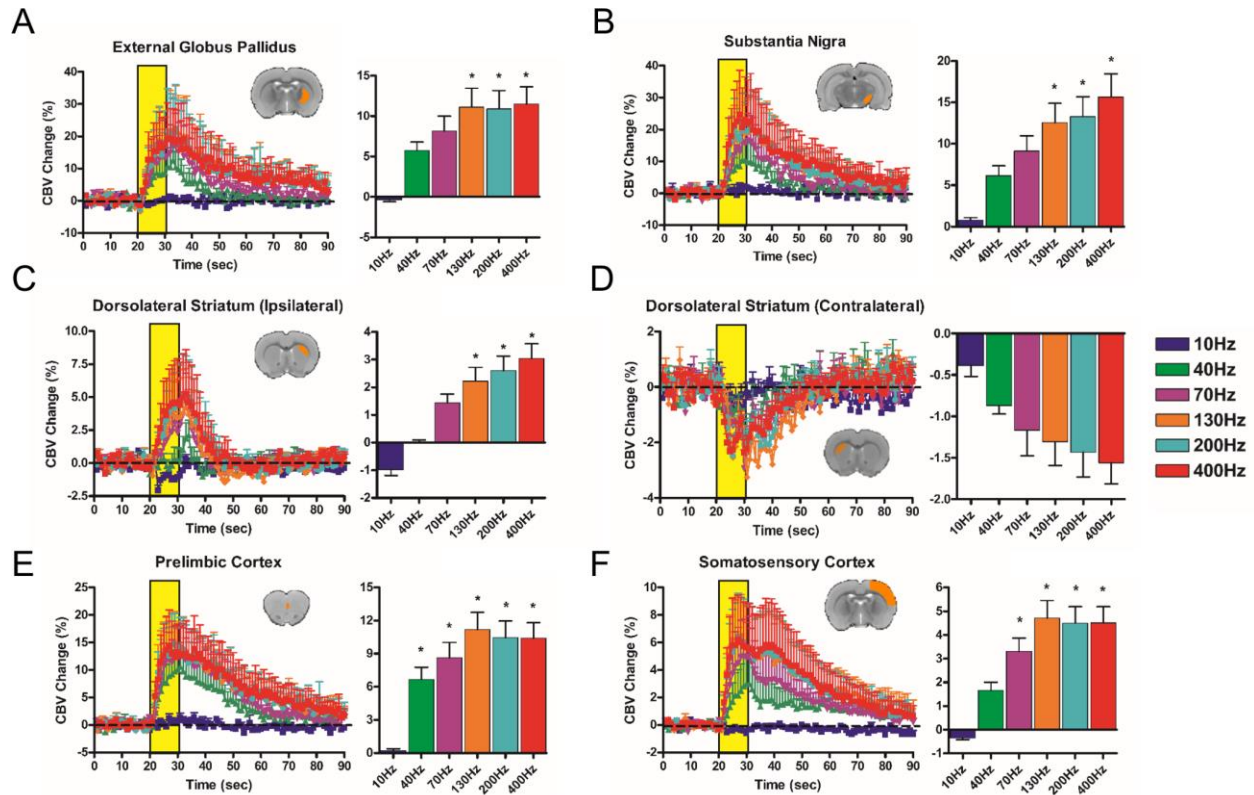


Figure 3.4. GPe-DBS evoked CBV changes at select, anatomically-defined regions of interest. CBV traces (10-400 Hz; yellow bar denotes stimulation epoch; note different Y axis scales across ROIs) are accompanied by bar graphs displaying percent changes in CBV amplitude changes during the stimulation period (mean \pm SEM CBV values for the DBS stimulation period). * denotes significant differences in CBV amplitude from 10 Hz ($p < 0.05$). Insert depicts representative slice example for each pre-defined ROI (note that most ROIs encompassed multiple slices). Unless otherwise denoted, all ROIs are ipsilateral to the DBS hemisphere. **(A)** External globus pallidus **(B)** Substantia nigra **(C)** Ipsilateral dorsolateral striatum **(D)** Contralateral dorsolateral striatum **(E)** Prelimbic cortex **(F)** Somatosensory cortex. Note that the displayed ROI's for Panel E differ between Figures 3 and 4. Additional ROIs (total = 19; including Posterior hypothalamus) are located in **Supplemental Figure S3.7**.

Lastly, to determine the frequency-dependency of DBS responses at both targets, the amplitude of CBV responses was quantified for a subset of ROIs: GPe, substantia nigra,

dorsolateral striatum (ipsi- and contralateral, somatosensory cortex, posterior hypothalamus (SNr-DBS only), and prelimbic cortex (GPe-DBS only) (**Figure 3.3-4**). These amplitude measures correspond to the mean CBV changes during the stimulation epoch for each DBS frequency (see Methods); because of differences in the characteristic trace dynamics for each ROI (e.g., hemodynamic delays), the calculated values are best compared across frequencies but not across ROI's. A main effect of DBS frequency was found for each ROI analyzed ($p < 0.05$), and post-hoc testing revealed that 10 Hz DBS drove CBV amplitude changes that often significantly differed from other frequencies. However, as suggested by the CBV traces, the influence of stimulation frequency on CBV responses was inconsistent across ROIs. For example, CBV amplitudes for some ROIs scaled positively with DBS frequency (e.g., the GPe during SNr-DBS), whereas peak amplitudes occurred at frequencies below 400 Hz for other ROIs (e.g., prelimbic and somatosensory cortices during SNr-DBS) (see **Figures 3.3 and S3.6**).

fcMRI

Complementing our evoked-fMRI findings, fcMRI measurements revealed global and frequency-dependent modulation by DBS at both targets. Mean correlation matrices were generated for each stimulus condition (Rest₁, Stim 40 Hz, Rest₂, Stim 130 Hz, and Rest₃) and DBS target (SNr and GPe); **Figure 3.5A**. The cross-correlational matrices, displaying functional connectivity strength between 90 discrete brain regions (45 per hemisphere), revealed modulation that appeared specific to the 130 Hz DBS condition, including both enhancements (increased correlation) and suppressions (increased anti-correlation) of connectivity. This modulation of fcMRI signals appeared moderately reversible, as the post 130 Hz stimulation “rest” scan (conducted immediately following the 130 Hz DBS fcMRI

scan), was qualitatively similar to prior non-stimulation scans. Functional connectivity modulation by 40 Hz DBS was less apparent at both targets. Significant individual fcMRI connections were computed (rANOVA, $p < 0.01$ uncorrected, $\Delta Z\text{-Corr} > 0.10$) and categorized according to modulation direction; **Supplemental Tables S3.1 (SNr) and Table S3.2 (GPe)**. Post-hoc comparison of the significantly modulated connections confirmed the qualitative observations; **Figure 3.5B**. For both DBS targets (SNr and GPe) and modulation directions (Enhanced and Suppressed) there was a significant main-effect of condition (ANOVA $p < 0.001$); SNr: $F_E(4,165) = 25.13$ and $F_S(4,75) = 11.79$, GPe: $F_E(4,190) = 24.39$ and $F_S(4,190) = 26.49$. Further post-hoc pair-wise comparisons between conditions revealed 130 Hz stimulation specificity; i.e. 130 Hz was significantly different from all rest conditions and 40 Hz stimulation, $p < 0.001$. Furthermore, no statistical differences were detected between any other conditions, including Rest₃, suggesting the stimulation effect was indeed reversible.

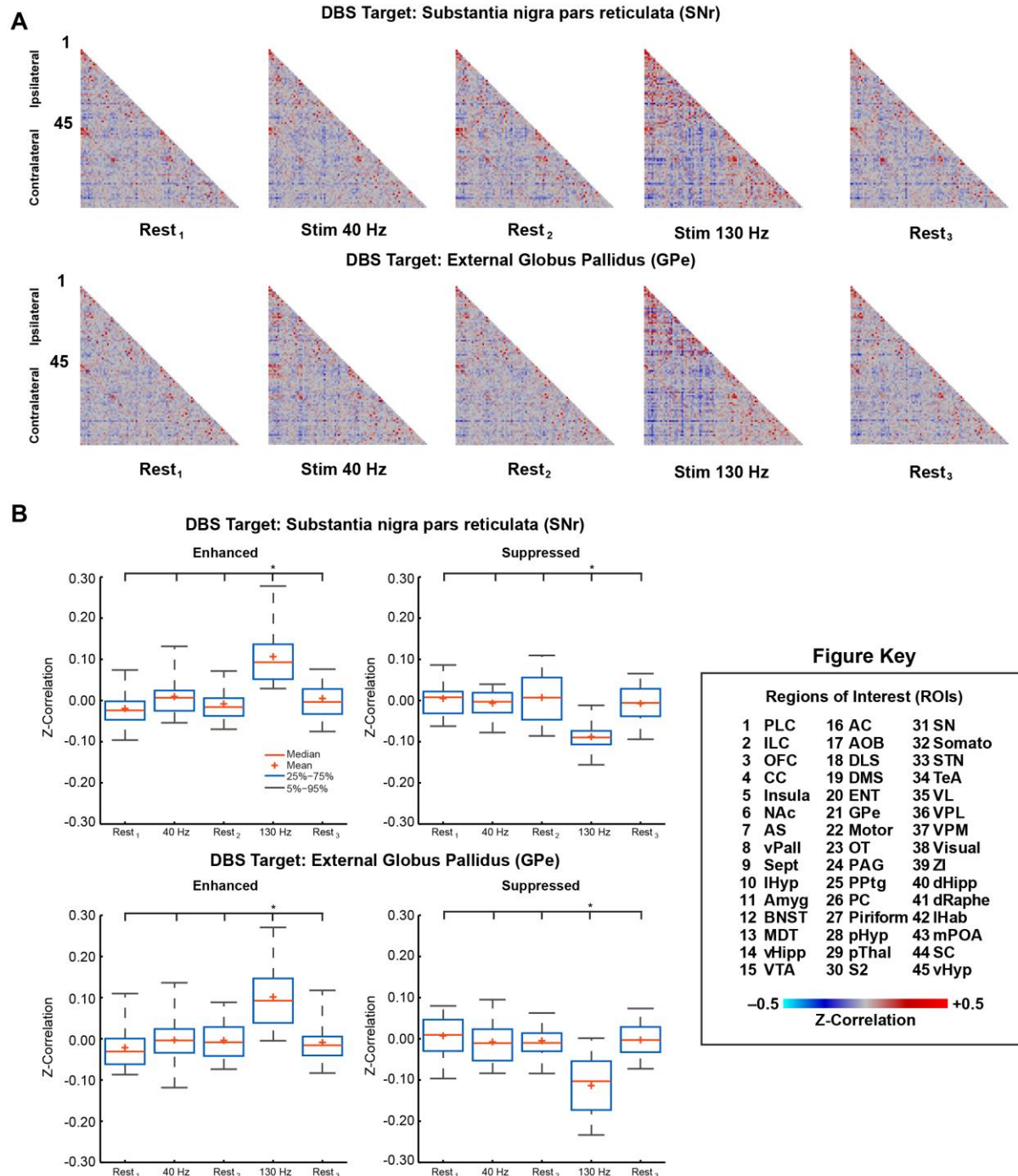


Figure 3.5. fMRI Modulation via DBS of the SNr and GPe. **(A)** Mean correlation matrices (SNr $n = 6$, GPe $n = 7$) for each stimulus condition (Rest₁, Stim 40 Hz, Rest₂, Stim 130 Hz, Rest₃) using 45 region-of-interests (ROIs: 1-45 Ipsilateral, 46-90 Contralateral, see Figure Key). **(B)** Post-hoc comparison of significantly modulated connections. Significance of individual connections (see Supporting Material: **Supplemental Tables 1-2**) was determined using repeated measures analysis of variance across animals (rANOVA, $p \leq 0.01$ uncorrected, $\Delta Z\text{-correlation} \geq 0.10$). Connections were grouped according to modulation direction (Enhanced: increased correlation; Suppressed: increased anti-correlation) and

then two-sample t-tests (see Supporting Material: **Table S3**) were used to statistically compare stimulus conditions (Rest, 40 Hz, and 130 Hz, see Figure Key). Data plotted as mean \pm standard error of the mean (SEM). *s denote pair-wise significant ($p < 0.001$) differences. **Abbreviations:** **PLC:** Prelimbic Cortex; **ILC:** Infralimbic Cortex; **OFC:** Orbitofrontal Cortex; **CC:** Cingulate Cortex; **Insula:** Insular Cortex; **NAc:** Nucleus Accumbens; **AS:** Anterior Striatum; **vPall:** Ventral Pallidum; **Sept:** Septum; **lHyp:** Lateral Hypothalamus; **Amyg:** Amygdala; **BNST:** Bed Nucleus of the Stria Terminalis; **MDT:** Mediodorsal Thalamus; **vHipp:** Ventral Hippocampus; **VTA:** Ventral Tegmental Area; **AC:** Auditory Cortex; **AOB:** Accessory Olfactory Bulb; **DLS:** Dorsolateral Striatum; **DMS:** Dorsomedial Striatum; **ENT:** Entorhinal Cortex; **GPe:** External Globus Pallidus; **Motor:** Motor Cortex (Primary and Secondary); **OT:** Olfactory Tubercle; **PAG:** Periaqueductal Grey; **PPTg:** Pedunculo pontine Tegmental Nucleus; **PC:** Parietal Cortex; **Piriform:** Piriform Cortex; **pHyp:** Posterior Hypothalamus; **pThal:** Posterior Thalamus; **S2:** Secondary Somatosensory Cortex; **SN:** Substantia Nigra; **Somato:** Primary Somatosensory Cortex; **STN:** Subthalamic Nucleus; **TeA:** Temporal Association Cortex; **VL:** Ventrolateral Thalamus; **VPL:** Ventral Posterolateral Thalamus; **Visual:** Visual Cortex (Primary and Secondary); **ZI:** Zona Incerta; **dHipp:** Dorsal Hippocampus; **dRaph:** Dorsal Raphe Nucleus; **lHab:** Lateral Habenula; **mPOA:** Medial Preoptic Area; **SC:** Superior Colliculus; **vHyp:** Ventral Hypothalamus.

Several connections showed more robust modulation (**Figure 3.6**, and see **Supplemental Tables S3.1-2:** $|\Delta Z\text{-Corr}| > 0.20$). Here, we focus on describing the enhanced connections given the potential confound of global signal regression (see next paragraph). Specifically, SNr-DBS produced several ipsilateral enhancements; VTA (#15) \leftrightarrow Insula (#5), pHyp (#28) \leftrightarrow Insula (#5), STN (#31) \leftrightarrow GPe (#21), ZI (#39) \leftrightarrow GPe (#21), ZI (#39) \leftrightarrow GPe (#STN). Only one connection demonstrated robust enhancement in the contralateral hemisphere: SNr-DBS, dHipp (#85) \leftrightarrow Somato (#77). Similarly, GPe-DBS produced robust ipsilateral enhancement for the following connections; Motor (#22) \leftrightarrow Insula (#5), ZI (#39) \leftrightarrow Insula (#5), VC (#38) \leftrightarrow AC (#16), and ZI (#39) \leftrightarrow Motor (#22).

In order to assess the sensitivity of the observed enhancements/suppressions to GSR, we re-capitulated the post-hoc comparisons of the previously defined modulated connections using pre-processed data without GSR. The main-effect of condition for both

DBS targets was maintained for enhanced but not for suppressed connections (**see Supplemental Figure S3.8**); SNr: $F_E(4,165) = 6.81$ $p < 0.001$ and $F_S(4,75) = 0.92$ $p = 0.460$, GPe: $F_E(4,190) = 5.71$ $p < 0.001$ and $F_S(4,190) = 1.85$ $p = 0.121$. Some trends were still evident for the suppressed connections however all conditions and groupings exhibited substantial shifts towards more positive values. Moreover, 130 Hz specificities were maintained for the enhanced connections; SNr $p \leq 0.016$, GPe $p \leq 0.006$. Finally, we further evaluated the similarity (cross-correlation) of the global signal (GS) across conditions. The main-effect of condition was insignificant for both DBS targets suggesting there was a high degree of similarity in the GS regardless of condition (rANOVA); SNr: $F(9,45) = 1.63$ $P = 0.134$, GPe: $F(9,54) = 0.85$ $P = 0.572$.

Next, significant modulations were considered in the context of functional network groupings: Sensorimotor, Executive, Limbic, and Between network connections. Categorical listing for each brain region are provided in the supporting material; **Supplemental Tables S3.1-2**. Between network connections reflect connections that crossed functional category (e.g., between sensorimotor and limbic regions). Of connections meeting significance criteria, a larger proportion of enhancements were observed for the SNr: 34 enhanced, 16 suppressed. Enhancement and suppression were equivalent for GPe stimulation; 39 enhanced and suppressed. In terms of overall network modulation, most DBS-sensitive connections fell within the Between network category (SNr: 33; GPe, 48) followed by the Sensorimotor, Limbic, Executive networks, respectively. Finally, many of the robust modulations either localized to the Sensorimotor network, or involved sensorimotor regions.

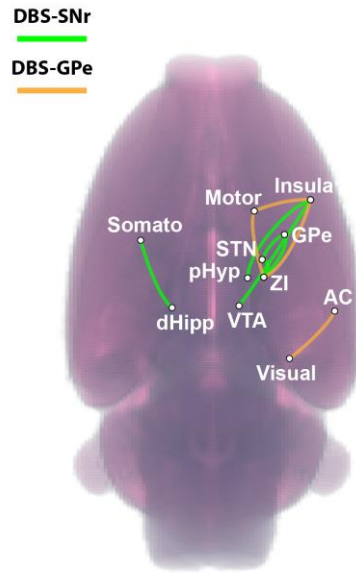


Figure 3.6. Robust Functional Connectivity Modulation. Enhanced connections demonstrating more robust modulation ($\Delta Z\text{-Corr} > 0.20$) overlaid on volume rendering of the rat brain (also see **Tables S3.1-2**). Green – SNr-DBS, Orange – GPe-DBS.

3.4 Discussion

The present study was undertaken to map the functional circuit and network connectivity of the SNr and GPe, and to further evaluate the influence of stimulation frequency on the measured connectivity profiles. Although both regions have traditionally been classified as simple relay nuclei, our DBS results reveal extensive functional circuit and network interconnectivity, consistent with “extra-relay” processing power. Below, we highlight the major findings and limitations of this work.

Frequency-dependency of evoked DBS responses

The usage of multiple stimulation frequencies in DBS-fMRI studies allows for the characterization of frequency tuning in neural circuits (132, 140, 170, 182, 210, 213). The demonstration of DBS frequency-sensitive fMRI signals is likely due to both passive and

active electrical membrane properties, including voltage-sensitive ion channel complements and their associated channel refractory periods (171). 10 Hz stimulation of either the SNr or GPe did not result in any detectable fMRI signal changes, while the stimulation frequency that evoked the largest CBV responses varied considerably by region. Perhaps the most compelling example of frequency selective circuit modulation in the present study occurred with 200 Hz SNr-DBS. At both lower and higher frequencies (40-130, 400 Hz), prefrontal and frontal cortical regions (e.g., infralimbic, motor, cingulate cortices) responded to SNr-DBS with CBV increases that were modest and time-locked to the stimulation period. However, these brain regions responded to 200 Hz stimulation with CBV increases that were much larger than at other frequencies, and peaked with a long delay (in certain case, after the cessation of stimulation). The reasoning behind such remarkably frequency selectivity in these responses, with highly unique temporal characteristics (in relation to the stimulation period), is an interesting area for future study. Finally, the inclusion of very high stimulation frequencies in the present study (e.g., 130 Hz) is notable in the context of therapeutic DBS (see below section on Translational Relevance).

Striatal and Thalamic CBV modulation by SNr- and GPe-DBS

Both the GPe- and SNr are downstream targets of the striatum, receiving GABAergic input through the so-called indirect and direct pathways, respectively. Although striatal activity changes may thus be anticipated during either GPe- or SNr-DBS, our demonstration of striatal modulation by DBS at each target is of remarkable interest for several reasons. First, although the basal ganglia are frequently modeled as intrahemispheric systems, we observed pronounced bilaterality in striatal modulation by GPe- or SNr-DBS. Irrespective of

whether this modulation occurs through feedforward thalamo-cortico-striatal loops, antidromic recruitment of striatal fibers, or other means, our results strongly suggest that presence of powerful bilateral connectivity within the basal ganglia systems. Of further interest is the directionality of this striatal hemodynamic response; prominent CBV decreases were noted within the dorsal striatum during DBS of either the SNr or GPe, and occurred across a wide range of stimulation frequencies (40Hz and higher). Such striatal vasoconstriction is highly reminiscent of fMRI responses obtained during evoked nociceptive peripheral stimulation (214, 215). The extent and magnitude of the DBS-evoked signals was greater at the SNr target compared to the GPe, and was also greater in the hemisphere contralateral to stimulation (although ipsilateral decreases were also observed with both DBS targets). Although it may be intuitive to interpret our data as DBS-evoked neuronal inhibition, the situation appears to be particularly muddled in striatum, wherein dopaminergic neurotransmission has been hypothesized to induce vasoconstriction independent of direct activity changes within striatal neurons (216) or regional metabolism (217). In addition, striatal CBV decreases have previously been shown with heightened local neuronal activity, as observed in rats during noxious forepaw stimulation (215, 218), or epileptic slow-wave discharge (219). In light of these complexities, further work will be necessary to determine the underlying mechanism of striatal CBV decreases evoked during GPe- and SNr-DBS.

The directionality of CBV responses was also perplexing in the basal ganglia output-receiving thalamic areas (e.g., ventral thalamus), which are modeled as receiving functionally antagonistic modulation by the GPe and SNr (38, 202). The framework of this model, and the observation that electrical stimulation of the rat SNr generates GABA-

mediated inhibition in ventral thalamus (220), suggest that SNr-DBS should drive CBV signal decreases in ventral thalamus (and other nigral outputs) consistent with neuronal inhibition. Yet, we observed only positive CBV responses in thalamic regions during DBS delivered at either the GPe or SNr. Among the many possible explanations for SNr-DBS evoked thalamic CBV increases are: 1) bona fide thalamic activity increases downstream of non-canonical nigral circuits; 2) “off target” circuit modulation due to the nonselectivity of electrical stimulation (discussed in Section 4.6, Limitations); and 3) neurovascular uncoupling mechanisms similar to as discussed for the striatal CBV signals. Future DBS-fMRI studies coupled with more selective stimulation modalities (e.g., optogenetics) and electrophysiological recordings will be necessary to distinguish between these possibilities.

Frontal cortical CBV increases evoked by GPe-DBS

One major unexpected finding in this study was the robust modulation of frontal cortical areas (including prefrontal and motor cortices) by GPe-DBS. Historically, the GPe has been viewed primarily as a basal ganglia relay nucleus with only indirect control over cortical activity (38, 202). Very recently, however, two studies have identified a direct, ipsilateral projection from GPe to frontal cortex in mouse, rat, and monkey (76, 77). The GPe neurons that make up this projection are GABAergic and express the GABA vesicular transporter (vGAT), with a large subset additionally being cholinergic (expressing choline acetyltransferase (ChAT)). This pathway innervates all layers of cortex, targeting both pyramidal cells and interneurons. Unsurprisingly, selective optogenetic stimulation of this pathway results in mixed patterns of modulation among frontal cortical neurons, with both inhibition and enhanced firing rates observed *in vivo* (76). As expected based on neurochemical makeup, selective stimulation of this projection is predominantly inhibitory

for cortical neurons. However, given that this projection has been reported to biasedly innervate cortical interneurons, it is possible that inhibitory mechanisms within cortex result in enhanced cortical activity and vasodilatation. The robust modulation of frontal cortex by GPe-DBS observed in the present study may be the result of such pallido-cortical transmission, although the use of nonselective electrical stimulation precludes a definitive interpretation.

fcMRI

Complementing our evoked-fMRI findings, fcMRI measurements revealed frequency-dependent functional connectivity modulation by DBS at both targets. More specifically, we observed significant modulation of global functional connectivity (compared to baseline scans) with 130 Hz, but not 40 Hz, stimulation. This observed frequency-dependence of DBS-induced fcMRI network modulation is perplexing in that robust circuit modulation (measured with evoked-fMRI) was observed at both 40 and 130 Hz DBS. It is not clear why 40 Hz DBS of the GPe or SNr was insufficient to significantly modulate fcMRI networks, however this finding suggests that fcMRI networks may be more rigid than evoked-fMRI circuits (although this interpretation is highly speculative). The GPe and SNr are both pacemaker nuclei, with some neurons exhibiting intrinsic firing rates as high as 50 Hz (GPe) and 80 Hz (SNr) (1, 70). It is possible that, given these relatively high intrinsic firing rates, exogenous stimulation by DBS may need to be employed at very high frequencies (e.g., 130 Hz) to override the normal network contributions of the GPe and SNr.

During GPe- and SNr-DBS at 130 Hz, both enhancements and suppressions in functional connectivity were noted between a wide number of brain regions, spanning large-scale functional and anatomical boundaries. Interestingly, compared to enhanced

connections, suppressed (i.e. shifts towards negative connectivity) demonstrated much greater sensitivity to global signal regression. Increased sensitivity to “negative correlations” following GSR has been well documented in BOLD fMRI studies (221), therefore GSR may have similar effects on CBV-based connectivity. CBV-weighted functional connectivity has been shown to largely mirror BOLD-based connectivity in the rat (222), though with lower overall connectivity strength and slightly different frequency spectra. Overall, functional connectivity studies using cerebral blood measures are still relatively scarce, and thus interpretations should be made with caution. This is particularly the case given that GSR remains a controversial topic in the BOLD fMRI field (221, 223), therefore we are hesitant to draw any major conclusions from the observed “suppression” effects. Nonetheless, it is important to note that suppressed connections were only detected after accounting for large-scale CBV-weighted changes.

Focusing on enhanced connections, the most robust effects were largely ipsilateral to the DBS target and demonstrated interesting patterns. Some spatial overlap between enhanced networks was observed, with the insula and zona incerta appearing in both DBS-targeted networks (**Figure 3.6**). Consistent with the evoked responses, SNr-DBS enhanced connectivity involving the GPe and dorsal striatum (**Table S3.1**), however connectivity with the latter was not enhanced by GPe-DBS. This could be related to the fact that mixed (positive and negative) evoked responses were observed in the ipsilateral striatum during GPe-DBS, suggesting that more specific ROIs might be necessary to detect related functional connectivity modulation. Also of note, most enhanced connections did not directly involve the DBS target, but rather downstream and/or polysynaptic targets, particularly ‘between’ networks (Sensorimotor, Executive, and Limbic). The ability to

manipulate functional circuits using exogenous sources, as demonstrated here, has the potential to elucidate unique relationships between evoked signals and functional connectivity changes, and their relationships in different disease models; however, further experimentation/considerations are necessary, particularly in the context of GSR as outlined above. To our knowledge, this work provides the first example of electrical DBS-induced frequency-dependent functional connectivity modulation.

Translational Relevance

High frequency DBS targeting select brain nuclei or fiber tracts is now routinely employed in clinical settings for the treatment of certain intractable neurological and neuropsychiatric disorders (137, 148). The most prominent examples of successful DBS therapy are perhaps the targeting of the subthalamic nucleus (STN) or internal globus pallidus (GPi) for motor symptom alleviation in late-stage Parkinson's disease (139, 224). Given the dense interconnectivity of the basal ganglia, and the ability of DBS to modulate large-scale circuits and networks (135), it is not surprising that other basal ganglia nuclei have emerged as promising targets for DBS therapy (at least for those diseases involving basal ganglia dysfunction). Indeed, both GPe- and SNr-DBS have been reported to alleviate motor signs in Parkinson's disease (225-227). In certain cases, DBS at such noncanonical targets may offer some therapeutic advantages over STN/GPi-DBS for Parkinson's disease, for example, in alleviating axial motor symptoms (228). There is also emerging evidence that GPe and/or SNr-DBS may be clinically useful beyond the treatment of Parkinson's disease; for example, recent animal and patient studies of SNr-DBS have shown promise for the treatment of epilepsy (229-232).

Several findings in the present study may aid in the understanding of the neural mechanisms of GPe- and SNr-DBS therapy. Although GPe- and SNr-DBS have not been rigorously compared in the clinical setting, our findings suggest that both overlapping and distinct neural circuits may be modulated by these therapies. Among the most notable distinctions, ipsilateral prefrontal and frontal cortical areas were modulated to a far greater degree (as measured by evoked-fMRI) with GPe- compared to SNr-DBS. Given such profound differences in DBS-evoked circuit modulation, distinct therapeutic and/or adverse clinical responses would not be unexpected between DBS applied at each target. Also of interest is the presence of bilateral striatal responses during DBS at both targets. Therapeutic DBS, even applied unilaterally, can often exert bilateral behavioral responses (224), although the neural mechanisms underlying such response bilaterality are poorly understood. Our findings identify the contralateral striatal modulation as a candidate mechanism underlying bilateral clinical responses during both GPe- and SNr-DBS.

Limitations

Our study includes several limitations that are generally characteristic of preclinical fMRI-DBS experiments. The usage of anesthesia, as is commonly employed in preclinical fMRI experiments (140, 141, 213, 233), may alter the responsivity of neural circuits to the effects of DBS. One possible means by which an anesthetic effect may be evident could be in the stimulation strength threshold for detectable fMRI responses (see Chapter 2 Discussion).

With respect to our fcMRI experiments, DBS was employed continuously for 5 min durations; a stimulation length that has the potential to introduce drastic physiological changes. However, in our experiments, network responses to DBS appeared largely

reversible, as the post-DBS period connectivity was qualitatively and quantitatively similar to pre-DBS. Nonetheless, it may be beneficial in future DBS-fMRI studies to explore the use of interleaved DBS OFF-ON-OFF fMRI paradigms with shorter stimulation periods.

The use of electrical stimulation for circuit mapping may be viewed as either a strength or weakness in the present study; it is highly translationally-relevant in the context of clinical DBS therapy, yet comes with limitations of circuit recruitment specificity. As suggested above, electrical stimulation may be prone to off-target circuit recruitment, and may present another limitation to the present study. Electrical stimulation is capable of recruiting fibers of passage, and current may also spread beyond the anatomical boundaries of the target region; in either instance, “off-target” areas may be recruited by DBS. An additional, related point concerns the directionality of connectivity between the DBS target region and other modulated areas. Because DBS can recruit connected brain areas through both ortho- and antidromic signal propagation across fibers (134, 234), this approach to functional circuit mapping cannot readily distinguish between up- and downstream circuit elements. The use of opto- and/or pharmacogenetic tools should provide a more precise means for functional imaging-based circuit mapping (131, 146, 235), although at the likely expense of translational relevance in the context of therapeutic DBS in clinical settings.

Conclusions

This study implemented a simultaneous DBS-fMRI approach to investigate the functional connectivity of the GPe and SNr, the two major striatal output nuclei. Through their roles in the basal ganglia loops, these regions have a diverse number of functional roles in cognition, motor control, and emotional processing. As demonstrated here and

elsewhere, DBS-fMRI provides a global perspective of a brain region's functional connectivity profile, ultimately allowing for the identification and characterization of novel circuit connections. In the present work we identified, among other results, DBS-evoked negative fMRI signals in the bilateral striatum, as well as frequency-dependent, large-scale functional connectivity changes. Broadly, our work contributes to a growing literature demonstrating functional connectivity of the striatal outputs outside of canonical thalamic relay connections. Further, the inclusion of high frequency stimulation in our DBS experiments facilitates a translational perspective on our connectivity maps, as high frequency DBS at the GPe or SNr has demonstrated therapeutic benefits in certain neurological disease states (e.g., Parkinson's Disease).

CHAPTER 4: FUNCTIONAL CIRCUIT MAPPING OF THE EXTERNAL GLOBUS PALLIDUS IN THE HEALTHY AND PARKINSONIAN RAT: AN OPTOGENETIC-FMRI STUDY

4.1 Introduction

In Chapter 3, we have presented functional activation maps achieved by electrically stimulating the external globus pallidus (GPe) and substantia nigra pars reticulata (SNr). This work has generated several interesting findings, including the observance of bilateral striatal modulation (chiefly vasoconstriction) during electrical stimulation of either target. The neural elements responsible for such striatal modulation are not readily apparent (e.g., passing fibers, afferents, and/or efferents), in large part due to the nonspecificity of electrical stimulation methods. This is particularly the case for electrical stimulation of the GPe, which can, in principle, modulate striatal afferent fibers terminating in the GPe (indirect pathway), as well as those in route to the SNr (direct pathway). The use of more selective stimulation tools, such as optogenetics, may aid considerably in the development of functional connectivity maps concerning the striatal output nuclei. In the present study, we take such an approach, using optogenetic-fMRI to map the functional circuit connections of the GPe.

In addition to providing optogenetic-fMRI maps of the GPe in healthy rats, we also extend this research trajectory to include 6-hydroxydopamine (6-OHDA)-lesioned rats, a widely used rodent model of Parkinson's Disease (236-238). In the standard application of this model, unilateral intracranial microinjections of 6-OHDA, targeting the medial forebrain bundle or other dopamine neuron cell body/fiber sites acutely renders an

extensive lesioning of substantia nigra pars compacta neurons and their striatal afferents. This model has revealed widespread anatomical and functional circuit/network changes that occur in the basal ganglia following loss of dopaminergic tone, likely reflecting both pathological consequences of, and compensatory responses to neurodegeneration (10, 58, 237, 239, 240). With respect to the GPe, electrophysiological studies have revealed a loss of rhythmic pacemaker activity in the GPe following 6-OHDA lesioning, in favor of lower frequency bursting (237, 240, 241). Concerning GPe connectivity patterns in the parkinsonian state, most studies have focused on the GPe->STN (“prototypical”) pathway. For example, the GPe has been shown to generate proliferative inhibitory synapses in the STN, providing a potentially compensatory means of blunting activity in the pathologically overactive indirect pathway (242). Network changes involving the GPe and STN are also evident, with hypersynchronization often reported (239) and hypothesized to contribute to pathological oscillatory activity throughout the parkinsonian basal ganglia network (64).

In the present study, it is our aim to elucidate the circuit connectivity patterns of the GPe in both the healthy and parkinsonian state, using selective and spatially unbiased optogenetic-fMRI tools. We report that stimulation of GPe neurons drives downstream negative fMRI signals in the ipsilateral striatum, which are broadly attenuated in parkinsonian animals. Moreover, detectable modulation of ipsilateral prefrontal and frontal cortices (hereafter termed (pre)frontal cortex) emerges in the parkinsonian state. This work thus suggests novel features of GPe-centered circuit remodeling following chronic dopamine loss.

4.2 Materials and Methods

Subjects

Twelve adult male Sprague-Dawley rats (300–500g body weight; Charles River Laboratories, Wilmington, MA, USA) were used in this study. All procedures were performed in accordance with the National Institutes of Health Guidelines for Animal Research (Guide for the Care and Use of Laboratory Animals) and approved by the University of North Carolina Institutional Animal Care and Use Committee. Animals were housed under environmentally-controlled conditions (12h normal light/dark cycles, 20–23°C and 40–60% relative humidity), with food and water provided *ad libitum*.

Optogenetic Constructs

Neuronal opsin expression was achieved using adeno-associated viral vectors (AAV, serotype 5), encoding either a humanized variant of ChannelRhodopsin-2 (hChR2; H134R) fused to an enhanced yellow fluorescent protein (EYFP), or EYFP alone. Both constructs were placed under the human Synapsin (hSyn) promoter to target GPe neurons. All viruses were obtained from the Vector Core at the University of North Carolina at Chapel Hill.

Surgery

For all surgical procedures, rats were endotracheally intubated and mechanically ventilated using a small animal ventilator (CWE Inc., SAR-830/PA, Ardmore, PA). Anesthesia was maintained under a constant flow of 2% isoflurane mixed with medical air, and physiological parameters were continuously monitored and maintained within normal ranges using capnometry (Surgivet, Smith Medical, Waukesha, WI) and pulse oximetry (MouseOx Plus, STARR Life Science Corp., Oakmont, PA). Animals were head-fixed to a

stereotactic frame (Kopf Instruments, Model 962, Tujunga, CA) and the skull was exposed. Burr holes were drilled for the positioning of MR-compatible miniature brass screws (4 per skull; Item #94070A031, McMaster Carr, Atlanta, GA, USA), as well as for microinjections and chronic optic fiber placement (162).

For optogenetics, viral microinjections were targeted to the GPe with the following stereotactic injection coordinates (in reference to bregma and cortical surface, in mm): AP: -0.96mm, ML: +2.8mm, DV: -5.8mm. Viral injections were administered as 2 μ l volumes at a flow rate of 0.2 μ l/min, with a total infusion time of 10min. An additional 10 minutes was given for virus diffusion prior to slow retraction of the microsyringe needle. Chronically implantable optic fibers were placed 0.5mm above virus injection sites (see **Fig. 1c**). At least three weeks were given before opto-fMRI experiments were undertaken, to allow for sufficient virus expression.

In a subset of ChR2-injected rats ($n = 5$ of 10), unilateral microinjections (ipsilateral to viral microinfusions) of 6-OHDA (5 μ l volume, 3 μ g/ μ l dissolved in saline containing 0.02% ascorbic acid as an antioxidant) were targeted to the medial forebrain bundle (MFB) (see **Fig. 1b**). Stereotactic injection coordinates were as follow (in reference to bregma and cortical surface, in mm): AP: -4.5mm, ML: +1.4mm, DV: -8.0mm. Injections were made at an infusion rate of 0.5 μ l/min; the needle was left at the injected site for 10min following toxin delivery prior to being withdrawn.

Functional MRI

Detailed fMRI procedures, including animal handling and scan optimization, are as described in Chapter 2 Methods.

For anatomical referencing, a T₂-weighted RARE pilot image was taken in the mid-sagittal plane to localize the anterior commissure; this structure is located at approximately 0.8 mm posterior to the bregma and served as a reference for anteroposterior slice positioning in subsequent anatomical and functional scans. T₂-weighted anatomical images were obtained using a RARE sequence (scan parameters: TR = 2500 ms, TE = 33 ms, RARE factor = 8, slice thickness = 1 mm, matrix size= 256 x 256, FOV= 2.56 x 2.56 cm²). Twelve axial slices were acquired, with the 5th slice from the anterior direction aligned with the anterior commissure (as acquired in the previous T₂-weighted pilot scan). These images were used to confirm optic fiber placement within the GPe for each subject.

Optogenetic Stimulation

For optogenetic stimulation of the GPe ($n = 10$ for ChR2; $n = 2$ for EYFP control), a 473nm wavelength diode-pumped solid-state (DPSS) laser (model BL473T8-200, Shanghai Laser & Optics Century, Shanghai, China) was connected via a coupler to a homemade patch cable terminating above the chronically implanted optic fibers. Wavelength-specific light output at the terminating end of the patch cable was calibrated to 20mW using a wattage meter. Optogenetic stimulation periods consisted of a series of TTL-triggered light pulses with a stimulation frequency of 40Hz and pulse duration of 10ms. A 100 second block design paradigm was implemented, consisting of 20 seconds of rest (stimulation OFF) followed by two 10 seconds stimulation periods (stimulation ON), with intervening and final rest periods of 30 seconds (i.e. 20sOFF-10sON-30sOFF-10sON-30sOFF) (see **Fig. 4.1b**).

Histology

Following scan procedures, rats were deeply anesthetized with 1-2ml Euthasol and transcardially perfused with saline followed by 10% formalin. Extracted brains were stored overnight in 10% formalin and transferred to a 30% sucrose solution (in DI water) for 2-3 days, until brains sunk to bottom of storage bottles. Brains were cut to 40 μ m thick sections on a freezing microtome and GPe-containing sections were directly mounted on glass slides for fluorescent imaging. Vectashield mounting medium with DAPI stain (Vector laboratories, Item # H-1200) was used to provide a cell body counterstain. Slides were imaged using a Zeiss 780 confocal microscope to verify the transfected area. A representative example of virally-mediated ChR2 expression in GPe neurons is provided in **Fig. 1c**.

To confirm successful lesioning of dopamine neurons in 6-OHDA-treated subjects, tyrosine hydroxylase expression was examined in striatal and substantia nigra-containing brain sections. Sections were processed according to standard immunohistochemical procedures with DAB reaction, using a rabbit anti-tyrosine hydroxylase primary antibody (1:5000), and biotinylated goat anti-rabbit secondary antibody (1:50). Mounted sections were imaged by means of brightfield microscopy (Nikon Eclipse 80i) following immunohistochemical procedures.

fMRI Data Processing and Statistical Analyses

Preprocessing and image analysis was performed using SPM codes and custom-written Matlab (MathWorks Inc., Natick, MA). Evoked-fMRI datasets were first grouped by subject and DBS frequency, and realigned to the first volume of a well-positioned subject

using a least squares approach and a 6 parameter rigid body spatial transformation. Skull-stripping was next employed using a semi-automatic threshold method with manual masking, followed by image coregistration to an anatomical MRI rat atlas (174). One SNr-DBS subject was excluded for evoked-fMRI analysis after image quality control.

Functional response maps for averaged SNr- or GPe-DBS datasets were generated using the general linear model (GLM), with reference to baseline (frames 1-20) and incorporating a hemodynamic delay of 5 frames, similar to our previous DBS-fMRI studies (132, 133, 140). A Bonferroni correction was applied to adjust for the multiple comparisons of fMRI maps by the number of brain voxels (corrected $p < 0.05$ for positive and negative responses). All images were smoothed by applying a mean filter with a 3×3 kernel, and overlaid on an anatomical atlas for visualization (174).

For temporal analysis of stimulation-evoked CBV changes, 3-dimensional regions of interest (ROIs) were defined *a priori* according to anatomical structural boundaries (174, 176), and applied onto the coregistered data. The ROIs were chosen according to the anatomical areas showing statistically significant modulation in the functional response maps. Six ROIs were identified for analysis, all ipsilateral to the site of stimulation: GPe, prelimbic cortex, orbitofrontal cortex, dorsolateral striatum, dorsomedial striatum, infralimbic cortex. The baseline and stimulus evoked ΔR_2^* values were calculated as described in Chapter 2 Methods. For each ROI, the CBV signal time-course was plotted across all 100 time frames.

Stimulation-evoked changes in CBV amplitude were compared across subject groups for each ROI. These data are presented as mean \pm SEM. Statistical comparisons of DBS frequency effects on Δ CBV for each ROI were conducted using Graphpad Prism

software (San Diego, CA). Two-tailed, one-way repeated measures ANOVA (rANOVA) tests with Tukey post-hoc analyses were conducted to evaluate frequency-dependent responses. Significance level was set at $p < 0.05$.

4.3 Results

A depiction of the experimental paradigm is provided in **Figure 4.1**. Based on chosen atlas coordinates and optic fiber tract placements, optogenetic experiments were likely biased towards stimulation of the ventral portions of the GPe (see **Fig. 4.1c** for representative image of virus expression and optic fiber tract).

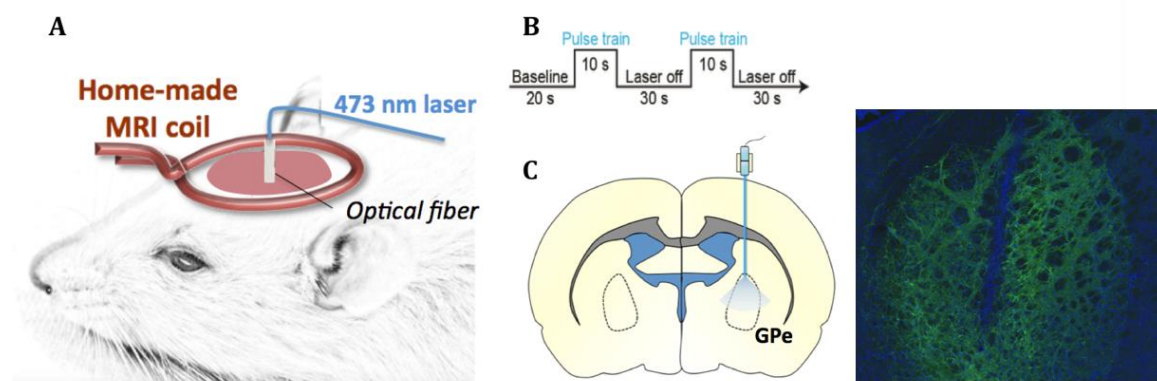


Figure 4.1. (A) Schematic of experimental imaging setup. (B) Optogenetic stimulation evoked-fMRI stimulus paradigm. (C) Cartoon of optogenetic targeting of the GPe (left), and representative image of Chr2 expression (green) in GPe (right).

Several major regions of modulation were detected during optogenetic stimulation of the GPe in healthy rats (**Figure 4.2**; top left). The GPe itself showed unilateral CBV increases, providing strong evidence that local stimulation experiments were successful. Also unilateral to the stimulation site, robust dorsal striatal CBV decreases were observed across its entire rostrocaudal axis, both within the medial and lateral subdivisions of this

nucleus. Lastly, bilateral responses were noted within canonical visual pathway sites (e.g., optic tectum), which we attribute to visual stimulation from the laser light. Note that these responses were largely present in EYFP control animals (**Figure 4.2**; top right), strongly suggesting that they are not consequences of optogenetic GPe stimulation.



Figure 4.2. 6-OHDA infusions into the medial forebrain bundle (MFB) (left) resulting in near-complete loss of TH expression in ipsilateral striatum (brown stain, right image is representative histological section from a single subject).

Following our characterization of optogenetic responses to GPe stimulation in healthy rats, we extended this study to include hemiparkinsonian rats lesioned using 6-OHDA. The surgical targeting of 6-OHDA to the medial forebrain bundle (ipsilateral to GPe manipulations), and representative image of resulting loss of tyrosine hydroxylase expression in the ipsilateral striatum, are both depicted in **Figure 4.3**. Compared to healthy rats, the evoked CBV response within the GPe during optogenetic stimulation was larger in size and intensity; this was particularly the case for the anterior portion of the GPe, which showed notable CBV increases in hemiparkinsonian, but not healthy subjects (**Figure 4.2**; bottom left). Conversely, the downstream striatal CBV response, while negative in both healthy and hemiparkinsonian subjects, was far reduced in the latter

group. Moreover, the striatal fMRI response became less distinct, exhibiting a more scattered spatial profile, particularly in the anterior half of the striatum. Finally, a negative CBV signal was observed within the ipsilateral frontal cortex, including the prelimbic, orbitofrontal, motor, and cingulate cortices; no such negative frontal cortical response was observed in healthy subjects.

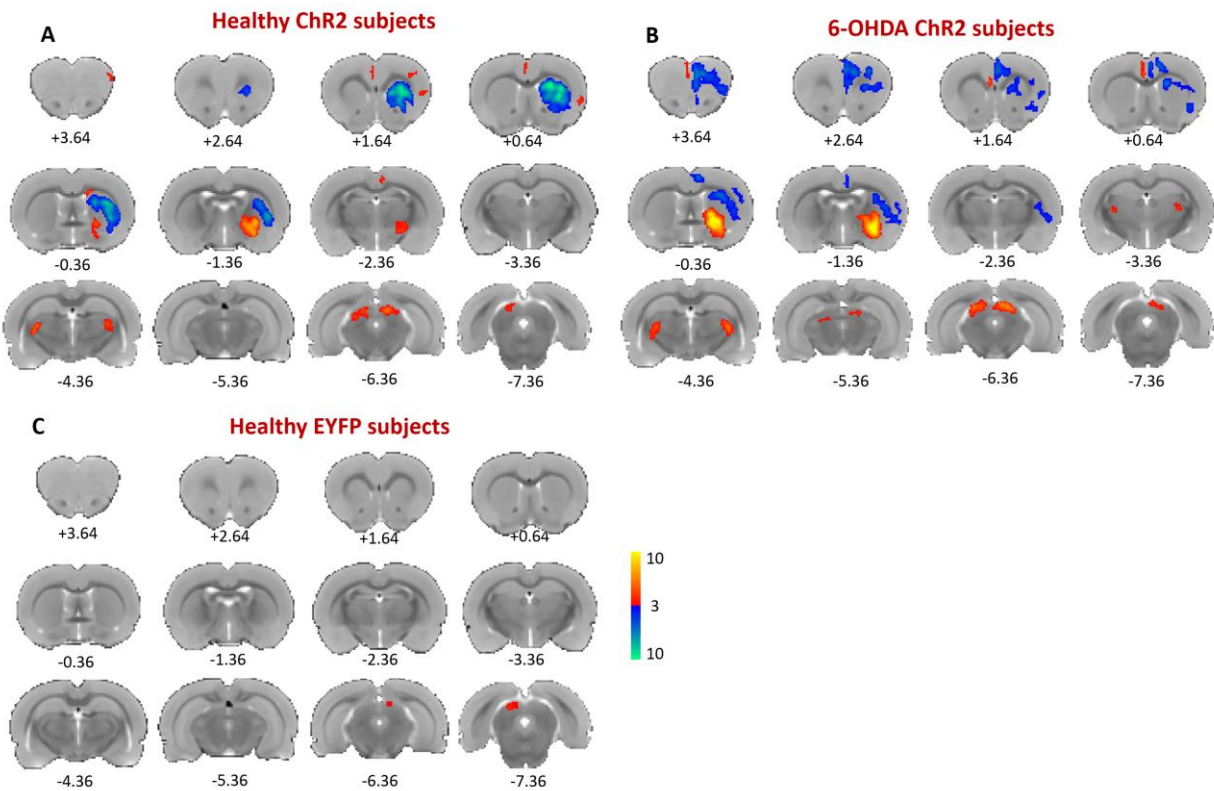


Figure 4.3. Functional activation maps of CBV modulation by optogenetic stimulation of the GPe (40 Hz). In healthy rats (top left), CBV increases were observed in the target region (GPe), whereas CBV decreases were apparent in the ipsilateral striatum. In hemiparkinsonian rats (top right), the GPe response was larger in size and magnitude, whereas the ipsilateral striatal CBV decreases were weaker and more scattered compared to healthy subjects. Moreover, a negative CBV response was noted in the ipsilateral (pre)frontal cortex. Visual pathway responses were observed in both healthy and hemiparkinsonian Chr2 subjects, and were also partially present in EYFP control rats (bottom left), likely attributable to non Chr2-mediated visual responses to laser light. 12 slices were acquired in each scan; anteroposterior distance relative to bregma (in mm) is as listed for **Figure 2.2**. Color bar denotes t score values obtained by GLM analyses, with a significance threshold of $p < 0.05$.

To further compare the obtained CBV responses across experimental conditions, we plotted the CBV time-courses and amplitudes changes across several anatomically defined regions of interest (ROI's); these are quantitative measures of percent CBV changes (**Figure 4.4**). As these ROI's were developed *a priori* based on anatomical borders rather than functional response patterns, they will underestimate CBV response magnitude in several regions. CBV increases were significantly larger in the GPe of hemiparkinsonian, compared to healthy subjects (ChR2 or EYFP), but were not significantly different between healthy ChR2 and EYFP subjects (likely attributable to effect wash-out as the response was not present throughout the entire GPe ROI). In the dorsolateral striatum, GPe stimulation evoked CBV decreases in healthy and hemiparkinsonian rats greater than 2.5 and 5% from baseline, respectively; both groups were significantly different from EYFP controls. Dorsomedial striatal CBV decreases were significant compared to control for hemiparkinsonian, but not healthy ChR2 subjects. With respect to (pre)frontal cortical regions, hemiparkinsonian subjects displayed significant decreases in CBV within the orbitofrontal, prelimbic, and infralimbic cortices. In contrast, healthy ChR2 subjects had weak but significant increases in infralimbic cortical CBV, but were not different from control in the other regions examined (prelimbic or orbitofrontal cortices).

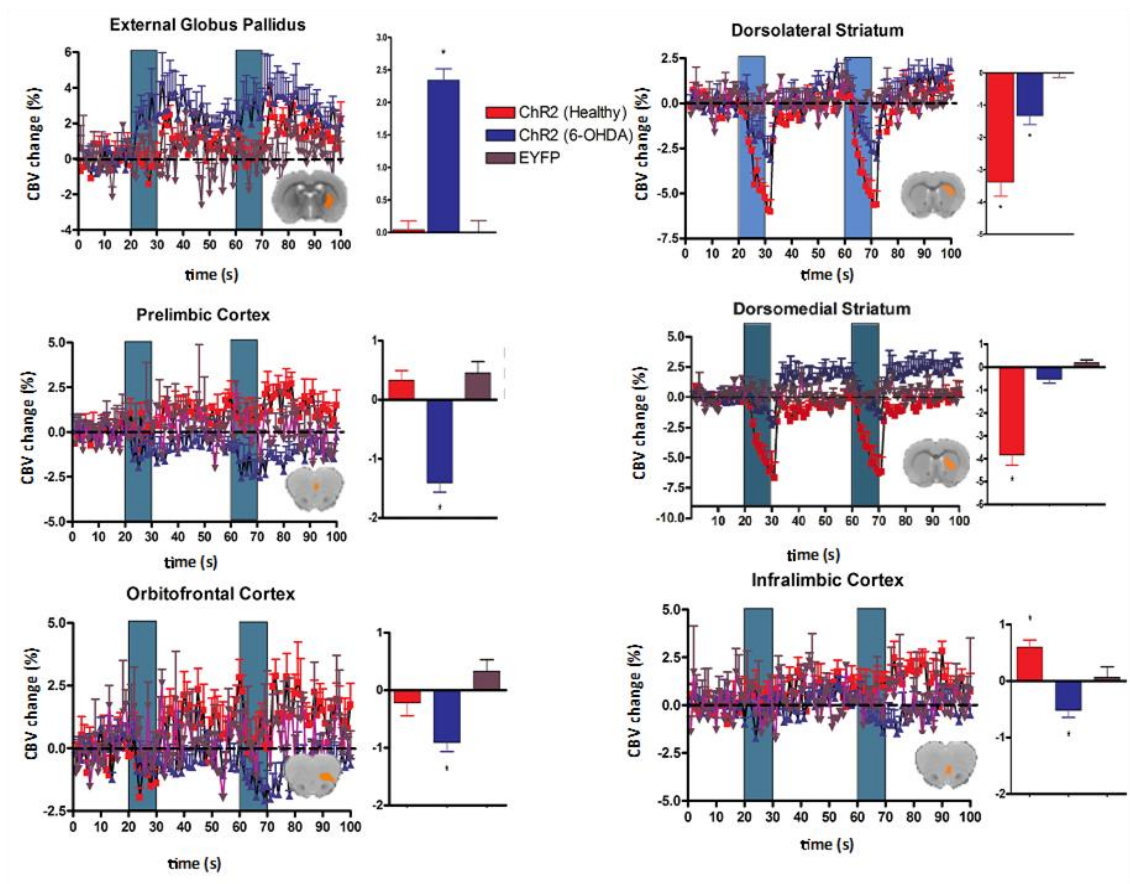


Figure 4.4. Optogenetic GPe stimulation-evoked CBV changes at select, anatomically-defined regions of interest. CBV traces (blue bars denote stimulation epochs; note different Y axis scales across ROIs) are accompanied by bar graphs displaying percent changes in CBV amplitude changes during the stimulation period (mean \pm SEM CBV values for the optogenetic stimulation period). * denotes significant differences in CBV amplitude from EYFP control subjects ($p < 0.05$). Insert depicts representative slice example for each pre-defined ROI (note that most ROIs encompassed multiple slices). All ROIs are ipsilateral to the stimulated hemisphere.

4.4 Discussion

In this study, we demonstrate that optogenetic stimulation of the GPe in healthy rats evokes local CBV increases and robust CBV decreases in the ipsilateral dorsal striatum. Remarkably, in 6-OHDA-treated hemiparkinsonian subjects, the strength of the local GPe response was increased, whereas the downstream striatal response was weaker. Moreover,

stimulation-evoked vasoconstriction was observed in several areas of the ipsilateral (pre)frontal cortex, only in hemiparkinsonian subjects.

That optogenetic stimulation of the GPe evokes positive CBV increases was an expected finding, however it is not clear why this local response was larger in hemiparkinsonian subjects. *In vivo* electrophysiological recordings have demonstrated that firing rates of prototypical GPe neurons are reduced in 6-OHDA treated rats, whereas the firing rates of arkypallidal neurons appear relatively unaltered (70). Both populations, however, fire more synchronously in the dopamine-depleted state, in each case coupled to cortical slow wave activity (70). Additional notable features of GPe activity pattern changes in the parkinsonian state concerns the loss of pacemaking in favor of burst-firing, and the emergence of beta-frequency oscillations (15-30 Hz), as measured in the local field potential; both of these changes have hypothesized causal roles in parkinsonian motor deficits (239, 240). In our data, the presence of larger local CBV increases in the optogenetically stimulated GPe may reflect (among many possibilities), changes in the efficacy of optogenetic stimulation and/or the baseline activity state of the GPe. Whereas there is no straightforward reason to expect changes in the efficacy of optogenetically-evoked neuronal spiking in healthy vs. parkinsonian rats, changes in GPe baseline activity are likely to have occurred. In particular, the reduced firing rate of prototypical neurons, coupled with periods of quiescence due to loss of pacemaking, may broadly render the GPe hypoactive in the parkinsonian state. Such reduced baseline activity, in the absence of any other changes, may in principle be sufficient to generate larger CBV responses during local GPe stimulation. Additional experiments using electrophysiological measures would be necessary to confirm this hypothesis. A more direct approach to test this hypothesis may

include manipulations to modulate inhibitory tone and/or pacemaking ability in the GPe (e.g., HCN channel knockdown), with pre-and post-manipulation opto-fMRI recordings during GPe stimulation.

The most straightforward explanation for GPe stimulation-evoked striatal vasoconstriction is the recruitment of inhibitory arkypallidal inputs. However, this hypothesis is difficult to reconcile with the attenuation of the striatal fMRI response in the parkinsonian state, where arkypallidal inputs are strengthened as opposed to reduced (75). Striatal modulation downstream of other GPe outputs, including the subthalamic nucleus and frontal cortex, are potentially also involved through more complex circuit interactions. Finally, it is worth noting that striatal fMRI signals appear relatively complex compared to other brain regions, and may not always correlate with locally recorded electrophysiological changes. This point is discussed in detail elsewhere in this dissertation (e.g., see Chapter 2 discussion, Chapter 5, and General Discussion). An important future experiment will be to determine if acute pharmacological blockade of dopaminergic transmission is sufficient to attenuate the GPe stimulation-evoked striatal response; this data will help us to evaluate whether the attenuated striatal fMRI response is due to loss of dopamine signaling *per se*, or if other circuit changes following 6-OHDA treatment are involved (e.g., compensatory circuit remodeling).

The emergence of a negative CBV response in the ipsilateral (pre)frontal cortex of parkinsonian, but not healthy rats was a largely unexpected finding. Data presented in Chapter 3 of this dissertation demonstrates that, in healthy rats, electrical stimulation of the GPe results in robust CBV increases in the ipsilateral (pre)frontal cortex. The general absence of a similar response using more selective optogenetic stimulation tools suggests

that this response may be due to circuit mechanism outside of direct recruitment of GPe outputs, such as antidromic signaling and passing fiber recruitment with electrical but not optogenetic GPe stimulation). Of course, other differences between these stimulation tools must also be considered (detailed in Chapter 2 discussion). That (pre)frontal CBV modulation emerged during optogenetic stimulation of the GPe in the parkinsonian state suggests that GPe-(pre)frontal cortical interactions may be strengthened following dopamine lesioning. Of particular interest would be the examination of pallidocortical pathway changes following dopamine lesioning, particularly as examined using anatomical and electrophysiological tools. One must also consider the possibility that 6-OHDA-mediated neurodegeneration unmasked pre-existing circuit features, which may have also contributed to the observed functional connectivity differences in the healthy vs. parkinsonian state.

CHAPTER 5: OPTOGENETIC-FMRI CIRCUIT MAPPING OF THE STRIATUM AND ITS CORTICOSTRIATAL INPUT

5.1 Introduction

The tight coupling between neuronal activity and hemodynamic signaling in brain (i.e., neurovascular coupling) is a fundamental tenet of fMRI, critical for the interpretation of nearly all fMRI data. Despite decades of research, various fundamental features of neurovascular coupling remain contentious, including the relative contribution(s) of pre- vs. postsynaptic neuronal activity to hemodynamic changes. Driven by a seminal study in the cat visual system (123), the input theory posits that presynaptic activity is the major driver of neurovascular changes (as opposed to local spiking and postsynaptic activity) (119, 126, 189). Although this and other corroborative studies of the input theory were based on evaluation of cortical fMRI signals, the input theory proposes a predominant presynaptic contribution to fMRI signals throughout the brain. Investigations of the rodent striatum suggest that neurovascular coupling in this region may not be as straightforward as in cortex, particularly as multiple studies have reported inverse coupling of striatal spike unit activity and hemodynamic changes (215, 219). With this in mind, we used optogenetic-fMRI tools to test if the input theory is valid for the corticostriatal circuit, a massive, nonreciprocal excitatory projection from cortex to striatum. We demonstrate that optogenetic activation of corticostriatal projection neurons drives negative hemodynamic changes in striatum, a finding that is at odds with the input theory. We also provide evidence that local striatal circuit interactions are responsible for activity-evoked negative

fMRI signals in striatum. Broadly, this work provides a strong challenge to the universality of the input theory of fMRI signals.

5.2 Materials and Methods

Subjects

Eleven adult male Sprague-Dawley rats (300–500g body weight; Charles River Laboratories, Wilmington, MA, USA) were used in this study. All procedures were performed in accordance with the National Institutes of Health Guidelines for Animal Research (Guide for the Care and Use of Laboratory Animals) and approved by the University of North Carolina Institutional Animal Care and Use Committee. Animals were housed under environmentally-controlled conditions (12h normal light/dark cycles, 20–23°C and 40–60% relative humidity), with food and water provided *ad libitum*.

Optogenetic Constructs

Neuronal opsin expression was achieved using adeno-associated viral vectors (AAV, serotype 5), encoding either a humanized variant of ChannelRhodopsin-2 (hChR2; H134R) fused to an enhanced yellow fluorescent protein (EYFP), or EYFP alone. Both constructs were placed under the calcium-calmodulin kinase II α (CaMKII α) promoter to target either excitatory motor cortical projection neurons or striatal neurons. Viral titers were approximately 5.0×10^{12} viral genome/ml. All viruses were obtained from the Vector Core at the University of North Carolina at Chapel Hill.

Surgery

For all surgical procedures, rats were endotracheally intubated and mechanically ventilated using a small animal ventilator (CWE Inc., SAR-830/PA, Ardmore, PA).

Anesthesia was maintained under a constant flow of 2% isoflurane mixed with medical air, and physiological parameters were continuously monitored and maintained within normal ranges using capnometry (Surgivet, Smith Medical, Waukesha, WI) and pulse oximetry (MouseOx Plus, STARR Life Science Corp., Oakmont, PA). Animals were head-fixed to a stereotactic frame (Kopf Instruments, Model 962, Tujunga, CA) and the skull was exposed. Burr holes were drilled for the positioning of MR-compatible miniature brass screws (3-4 per skull; Item #94070A031, McMaster Carr, Atlanta, GA, USA), as well as for microinjections and chronic optic fiber placement (162).

For optogenetics, viral microinjections were targeted to either deep-layer motor cortex or dorsolateral striatum. For motor cortex, a single injection was made (1 μ l volume), whereas for striatum targeting, two injections were made of either 0.5 or 1 μ l volumes. The viral injection flow rate was 1 μ l/min, with a total infusion time of 10min for all experiments. An additional 10 minutes was given for virus diffusion prior to slow retraction of the microsyringe needle. Stereotactic injection coordinates were as follows (in reference to bregma and cortical surface, in mm): *Deep-Layer Motor Cortex*: AP: +3.0mm, ML: \pm 2.5mm, DV: -1.5mm; *Dorsolateral Striatum (Site 1)*: AP: +0.0mm, ML: +3.0mm, DV: -4.5mm; *Dorsolateral Striatum (Site 2)*: AP: +1.5mm, ML: +2.8mm, DV: -4.4mm.

Chronically implantable optic fibers were placed 0.5mm above virus injection sites for cell body targeting (site 1 for striatum experiments). For targeting of the striatonigral pathway, optic fibers were placed dorsally within the substantia nigra pars reticulata (SNr), using the following stereotactic coordinates: AP: -5.5mm, ML: +2.2mm, DV: -7.2mm. At least three or five weeks were given before opto-fMRI experiments were undertaken (for

cell body and terminal stimulation experiments, respectively), to allow for sufficient virus expression.

Functional MRI

Detailed fMRI procedures, including animal handling and scan optimization, are as described in Chapter 2 Methods.

Optogenetic Stimulation

For optogenetic stimulation, a 473nm wavelength diode-pumped solid-state (DPSS) laser (model BL473T8-200, Shanghai Laser & Optics Century, Shanghai, China) was connected via a coupler to a homemade patch cable terminating above the chronically implanted optic fibers. Wavelength-specific light output at the terminating end of the patch cable was calibrated to 15-20mW using a wattage meter. Optogenetic stimulation periods consisted of a series of TTL-triggered light pulses with a stimulation frequency of 40Hz and pulse duration of 5-10ms. For motor cortical and local striatal optogenetic stimulation experiments, a 100 second block design paradigm was implemented, consisting of 20 seconds of rest (stimulation OFF) followed by two 10 seconds stimulation periods (stimulation ON), with intervening and final rest periods of 30 seconds (i.e. 20sOFF-10sON-30sOFF-10sON-30sOFF). For striatonigral afferent stimulation experiments, a 920 second block design was implemented, consisting of 120 seconds OFF followed by five 40 second epochs stimulation ON, , with intervening and final rest periods of 120 seconds (i.e. 120sOFF-40sON-120sOFF-40sON-120sOFF-40sON-120sOFF-40sON-120sOFF-40sON-120sOFF).

fMRI Data Processing and Statistical Analyses

Preprocessing and image analysis was performed using SPM codes and custom-written Matlab (MathWorks Inc., Natick, MA). Optogenetic evoked-fMRI datasets were first grouped by subject, and realigned to the first volume of a well-positioned subject using a least squares approach and a 6 parameter rigid body spatial transformation. Skull-stripping was next employed using a semi-automatic threshold method with manual masking, followed by image coregistration to an anatomical MRI rat atlas (174).

Functional response maps for averaged fMRI datasets were generated using either cross-correlation methods (motor cortical and striatonigral experiments) or the general linear model (GLM) (local striatum stimulation experiment), with reference to baseline (frames 1-20) and incorporating a hemodynamic delay of 5 frames, similar to our previous DBS-fMRI studies (132, 133, 140). A Bonferroni correction was applied to adjust for the multiple comparisons of fMRI maps by the number of brain voxels (corrected $p < 0.05$ for positive and negative responses). All images were smoothed by applying a mean filter with a 3×3 kernel, and overlaid on an anatomical atlas for visualization (174).

For temporal analysis of stimulation-evoked CBV changes, functionally-defined cubic ROIs (5x5 voxels) were applied onto the coregistered data. The ROIs were chosen according to the anatomical areas showing statistically significant modulation in the functional response maps. The baseline and stimulus evoked ΔR_2^* values were calculated as described in Chapter 2 Methods. For each ROI, the CBV signal time-course was plotted across all time frames.

In some cases, stimulation-evoked changes in CBV amplitude were compared across subject groups at functionally-defined ROIs. These data are presented as mean \pm SEM.

Statistical comparisons of DBS frequency effects on Δ CBV for each ROI were conducted using Graphpad Prism software (San Diego, CA). Two-tailed, one-way repeated measures ANOVA (rANOVA) tests with Tukey post-hoc analyses were conducted to evaluate frequency-dependent responses. Significance level was set at $p < 0.05$.

Histology

Following scan procedures, rats were deeply anesthetized with a 1-2 ml cocktail of pentobarbital sodium and phenytoin sodium (Euthasol) and transcardially perfused with saline followed by 10% formalin. Extracted brains were stored overnight in 10% formalin and transferred to a 30% sucrose solution (in DI water) for 2-3 days, until brains sunk to bottom of storage bottles. Brains were cut to 40 μ m thick sections on a freezing microtome and mounted on glass slides for fluorescent imaging. Vectashield mounting medium with DAPI stain (Vector laboratories, Item # H-1200) was used to provide a cell body counterstain. Slides were imaged using a Zeiss 780 confocal microscope.

5.3 Results

Deep-Layer Motor Cortex Opto-fMRI

Transient optogenetic stimulation of the motor cortex elicited robust positive CBV responses locally, maximally reaching above 20% CBV increases from baseline (**Figure 5.1b**). In the dorsolateral striatum, which receives large-scale excitatory input from cortex (preferentially motor cortex), CBV decreased. This downstream striatal vasoconstriction was generally weak (less than 5% maximal change from CBV baseline), and lagged behind the motor cortical response. For this study, a within-subject EYFP control was employed

targeting the contralateral motor cortex. No significant responses were noted in either motor cortex or dorsolateral striatum during stimulation of the EYFP injected region (Figure 5.1c).

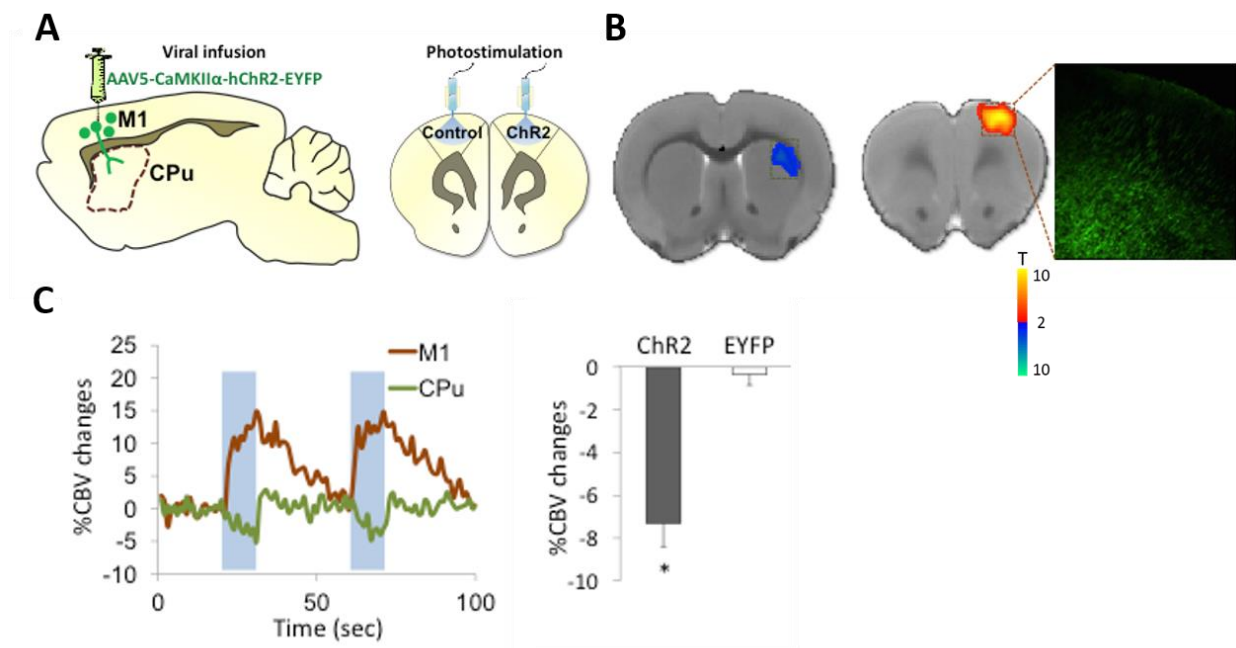


Figure 5.1. (A) Schematic of optogenetic targeting of deep layer motor cortical projection neurons ($n = 4$ for ChR2, $n = 2$ for EYFP controls). For this portion of the study, EYFP control experiments were conducted in a subset of experimental subjects, in the hemisphere contralateral to ChR2 stimulation. **(B)** Functional activation maps of CBV modulation by optogenetic stimulation of motor cortex (40 Hz), displaying marked CBV increases in motor cortex (right slice), and concomitant CBV decreases in the ipsilateral dorsolateral striatum (left slice). Insert image is of ChR2 expression (green) in motor cortex. Anteroposterior slice locations relative to bregma (in mm) are as follows: +2.64 right slice, +1.64 left slice. Color bar denotes t score values obtained by cross-correlational analyses, with a significance threshold of $p < 0.05$. **(C)** Temporal traces (left) and amplitudes (right) of CBV responses to optogenetic motor cortical stimulation at functionally-defined ROIs. Blue bars on graph of CBV traces denotes stimulation epochs. CBV changes induced by motor cortical stimulation in healthy subjects was significantly different from the EYFP control condition (* $p < 0.05$).

Compared to other optogenetic-fMRI targets discussed within this dissertation, local motor cortical responses to optogenetic stimulation were the most reliably elicited. The downstream dorsal striatal response, in contrast, was not consistently elicited- even in cases where motor cortical CBV increases were evident (data not shown). Preliminary data obtained from follow-up experiments in which larger portions of motor cortex were optogenetically stimulated (by use of multiple 1 μ l viral injections) suggests that this approach may more reliably evoke dorsal striatal vasoconstriction (data not shown).

Striatonigral Pathway Opto-fMRI

The demonstration of dorsal striatal vasoconstriction in response to recruitment of cortical excitatory input suggests that excitation, rather than inhibition of striatal neurons may contribute to striatal vasoconstriction. Thus, we next evaluated if stimulating striatal projection neurons of the direct pathway could similarly elicit a striatal negative CBV response. Due to the absence of experimental tools for direct delivery of opsins selectively to direct pathway MSNs, we took an alternative approach, virally infecting striatal neurons nonselectively, but stimulating striatal afferent fibers within the SNr. This approach thus selectively targets direct pathway MSNs selectively, at the level of their presynaptic terminals.

Optogenetic stimulation of striatonigral afferents elicited a robust negative CBV response that was qualitative similar, yet larger than that elicited by motor cortical stimulation (although the stimulation periods were also longer in this experiment; 40 sec here vs. 10 sec for motor cortical stimulation) (**Figure 5.2b**). Striatal CBV decreases grew in magnitude over the course of each stimulation epoch, reaching maximal values near 15% reductions from baseline, and rapidly returned to baseline following cessation of

stimulation (see **Figure 5.2c**). In EYFP control animals, no significant CBV responses were noted in the striatum.

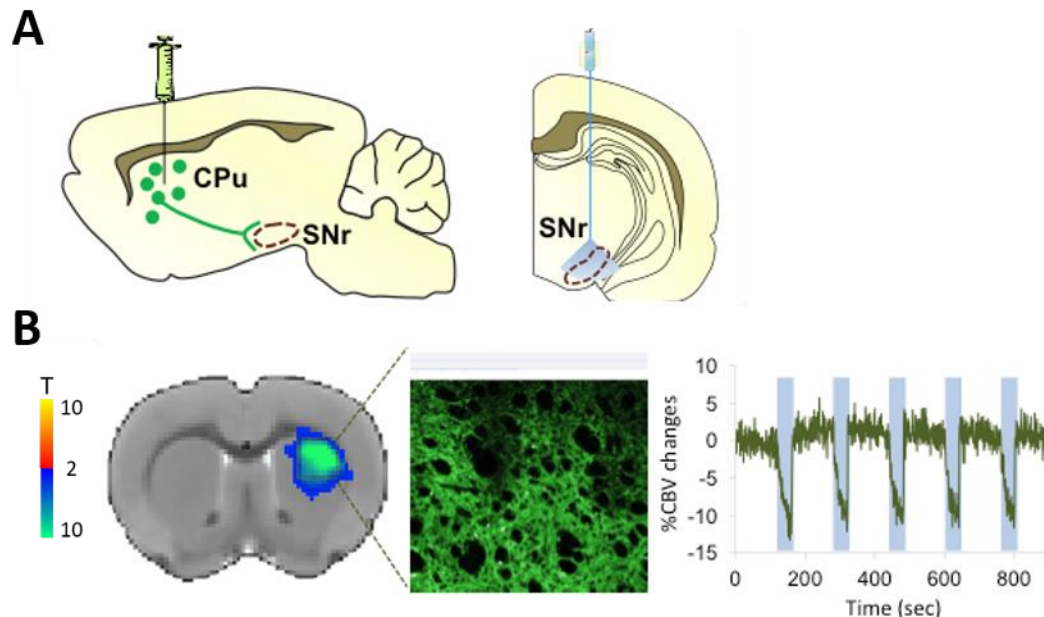


Figure 5.2. (A) Schematic of optogenetic targeting of striatonigral afferents ($n=4$). (B) Functional activation maps of CBV modulation by optogenetic stimulation of striatonigral afferents (40 Hz), displaying marked CBV decreases in the ipsilateral dorsal striatum. Insert image is of ChR2 expression (green) in striatum. Anteroposterior slice location relative to bregma (in mm) is +1.64 for displayed imaging slice. Color bar denotes t score values obtained by cross-correlational analyses, with a significance threshold of $p < 0.05$. Temporal CBV trace of striatal CBV response is displayed on right; blue bars denote stimulation epochs.

Striatal Cell Body Opto-fMRI

Striatonigral afferent stimulation could potentially elicit striatal vasoconstriction via multiple circuit mechanisms, including antidromic stimulation of direct pathway MSN somata, or orthodromic signaling through the cortico-basal ganglia loops. Thus, we next undertook a complementary experiment, examining the local fMRI response to optogenetic stimulation of striatal neurons at the cell body-level. This experiment revealed a unique mixture of striatal responses, characterized by vasodilation at the fiber stimulation site,

surrounded by a ring of widespread vasoconstriction (**Figure 5.3**). This data thus confirms our hypothesis that activation of striatal neurons is sufficient to elicit local striatal vasoconstriction. Additional downstream responses were also observed, including CBV increases within the GPe. This finding is particularly notable, as striatal activation would be expected to suppress GPe activity (through inhibitory indirect pathway inputs).

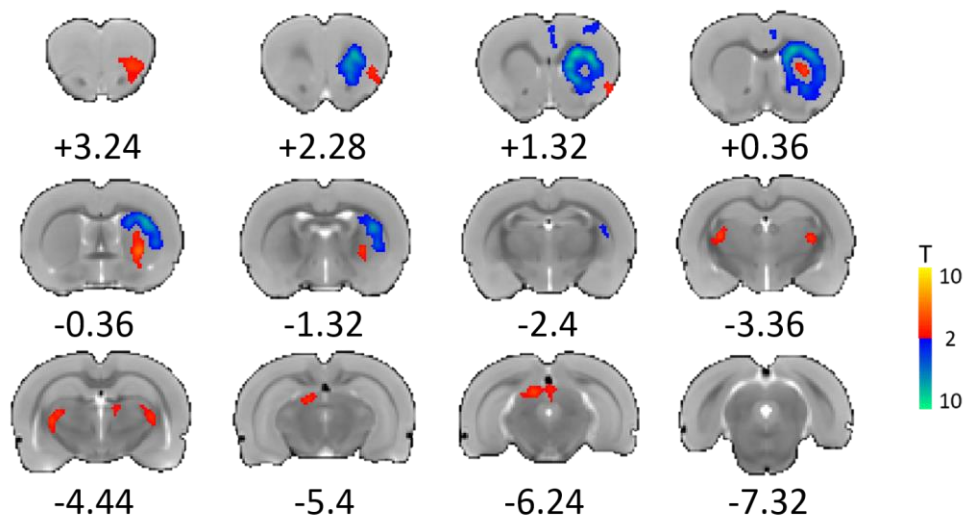


Figure 5.3. Functional activation maps of CBV modulation by optogenetic stimulation of the striatum (40 Hz). CBV increases were observed in a spatially confined region of striatum (proximal to the optic fiber), and surrounded by a “ring” of vasoconstriction that enveloped the surrounding area. CBV increases were also observed in the GPe, as were visual pathway responses (the latter likely attributable to non ChR2-mediated visual responses to laser light). 12 slices were acquired in each scan; anteroposterior distance relative to bregma (in mm) is listed below each slice. Color bar denotes t score values obtained by GLM analyses, with a significance threshold of $p < 0.05$

5.4 Discussion

The data presented in this chapter broadly challenges the universality of the input theory of fMRI signals. Specifically, we have demonstrated that optogenetic stimulation of motor cortical projection neurons, which nonreciprocally innervate dorsal striatum, drives

negative CBV changes in the dorsolateral striatum. Thus, the input theory-based prediction that input activity predominates fMRI signal generation does not hold in striatum, as recruitment of excitatory inputs drives negative fMRI signals in this nucleus. Moreover, preliminary data not reported here demonstrates that dorsal striatal blood-oxygen-level-dependent (BOLD) signal decreases similarly emerge during optogenetic stimulation of motor cortical projection neurons. This is an important point, as CBV and BOLD signals may in certain cases be dissociated (243).

Although the neural correlates of this negative striatal response cannot be fully explained based on our data, additional optogenetic-fMRI experiments reported here provide some important clues. Specifically, we show that optogenetic stimulation of either striatal neuronal somata (nonselectively) or striatonigral terminals each drives striatal CBV decreases. The latter experimental approach, likely resulting in antidromic stimulation of direct pathway striatal MSNs, suggests that recruitment of striatal projection neurons is sufficient to generate negative fMRI signals. Thus, it is exceedingly likely that postsynaptically-mediated circuit interactions, rather than cortical input activity, mediates corticostriatal pathway stimulation-evoked striatal vasoconstriction.

Optogenetic-fMRI experiments in which striatal neuronal subtypes are targeted more selectively would likely be helpful in evaluating the microcircuit-level mechanisms of excitation-evoked striatal fMRI signal decreases. In addition to evaluating the fMRI signals generated by stimulation of striatal interneurons vs. MSNs, direct and indirect pathway MSNs may be selectively targeted using cell type-specific gene promoters. A recent study by the Lee lab has done just that, reporting local BOLD signal increases following selective optogenetic stimulation of either direct or indirect pathway MSNs (244). This data is quite

difficult to reconcile with our findings, although our studies substantially differ in many ways, including animal model (rat vs. mouse), as well as methods of data acquisition and analysis. In the final chapter of this dissertation (Chapter 6; General Discussion), I propose several potential mechanisms for the seemingly paradoxical striatal vasoconstriction observed in our work.

CHAPTER 6: GENERAL DISCUSSION

6.1 Patterns and Putative Sources of Dorsal Striatal Vasoconstriction

A common theme observed among all of the studies presented in this dissertation is the observance of dorsal striatal vasoconstriction during electrical or optogenetic stimulation of various basal ganglia circuit elements. Specifically, dorsal striatal vasoconstriction was observed in response to the following stimulations: motor cortex (optogenetic), dorsal striatum (optogenetic), striatonigral afferents (optogenetic), ventral striatum (electrical), GPe (optogenetic and electrical), and the SNr (electrical). Thus, local excitation as well as modulation of various inputs (motor cortex and GPe) and outputs (striatonigral terminals) is all capable of driving dorsal striatal vasoconstriction. Even if we assume that similar downstream mechanisms are involved in each of these cases, the identification of the circuit-level underpinnings of the vasoconstrictive response is a tremendous task. Below, I describe a few clues, and suggest future studies aimed to elucidate potential mechanisms.

The possibility that dopamine signaling is involved in striatal vasoconstriction is raised by data from our group as well as others. Noxious forepaw stimulation evokes bilateral striatal vasoconstriction that is strongly attenuated by D2 receptor antagonism (215). Further, pharmacological-fMRI studies in rat and monkey have shown that D2 receptor agonists drive striatal vasoconstriction, whereas antagonism drives vasodilation (245, 246). Taken together, these results suggest D2 receptor activation as a potential

source of the observed striatal vasoconstriction in our studies. At least one finding from the present set of experiments also hints at a potential dopaminergic mechanism. Specifically data presented in Chapter 4 shows that optogenetic stimulation of GPe neurons drives ipsilateral striatal vasoconstriction that is greatly reduced in 6-OHDA-treated hemiparkinsonian rats. Although other acute and chronic neurological changes occur in this model, this work certainly suggests further exploration of the dopamine system. Such future studies will have to take into account that, in addition to the direct and modulatory properties of dopaminergic signaling on neuronal activity in striatum, dopamine is also a vasoactive compound (one of perhaps many in striatum, e.g., adenosine signaling), with D1 and D5 receptors being present on striatal microvessels (245). It should also be noted in this context that multiple groups (including our own) have observed positive dorsal striatal fMRI signals (CBV and BOLD) in response to selective optogenetic stimulation of midbrain dopamine neurons (131, 172). Thus, bulk dopamine release (as likely elicited by optogenetic stimulation of dopamine neurons), is an unlikely inductor of striatal vasoconstriction.

Lateral inhibition among striatal MSNs provides another attractive possible means for the excitation-driven vasoconstriction in the dorsal striatum. As elaborated upon in the General Introduction, striatal MSNs are interconnected via inhibitory collaterals. If a subset of striatal MSNs were excited by, e.g., local excitation, excitation of excitatory inputs, or disinhibition of inhibitory inputs, MSN collateral GABA release could, in theory, drive striatal vasoconstriction. The CBV response pattern observed in response to direct optogenetic stimulation of the dorsal striatum (see **Figure 5.3**) is particularly interesting in the context of this hypothesis. A similar ring-shaped border of negative fMRI signals has

been reported in response to selective stimulation of cortical parvalbumin interneurons, the shape of which was attributed to lateral inhibitory mechanisms (146).

There are potential criticisms to both dopamine signaling and lateral inhibition as putative mechanisms for the dorsal striatal vasoconstriction observed in our studies. Chief among them, as dopamine signaling and lateral inhibition are fundamental circuit features of the entire striatum, it is difficult to resolve why local optogenetic stimulation of the ventral striatum drives vasodilation instead of constriction (compare **Figures 2.6** and **5.3**). This finding is corroborated by the observance of ventral striatal BOLD signal increases driven by optogenetic stimulation of the rat prefrontal cortex (247). Perhaps this regional discrepancy in stimulation-evoked fMRI responses reflects generally understudied variations in the micro- and long-range circuit architecture of striatal subterritories, including differences in neurotransmitter receptor expression (e.g., acetylcholine receptor subtypes) (248), presence or absence of dopamine/glutamate corelease (109), and direct/indirect pathway striatal projection specificity (44).

6.2 Suggestions for Future Experimental Directions

The data presented in this dissertation both raise questions and suggest experimental directions for future fMRI-based circuit/network mapping studies of the basal ganglia. Here, I will discuss three major future study directions: 1) the determination of electrophysiological correlates to observed fMRI signals, 2) pharmacological fMRI interrogations of circuit stimulation-induced fMRI signals and 3) the application of more selective transgenic approaches to target basal ganglia nuclei subpopulations for optogenetic-fMRI experiments. Many of the technical weaknesses of our fMRI-based approach to circuit and network mapping, and associated alternative approaches (e.g.,

awake animal imaging to avoid anesthesia confounds) are described in detail elsewhere and will not be reviewed here (e.g., see Discussion sections for Chapters 2 and 3).

Determination of Electrophysiological Correlates

Because fMRI-based measurements describe neuronal activity patterns only very indirectly, the implementation of *in vivo* electrophysiological procedures would greatly benefit all of the studies described in this dissertation. For example, data presented in Chapter 2 suggests that neural circuit responses to NAc-DBS may be relatively frequency-insensitive; thus, it would be highly interesting to determine if unit activity or LFP modulation by DBS at certain downstream regions (e.g., amygdala, prefrontal cortex) is similarly DBS frequency-insensitive. Perhaps none of the observed evoked-fMRI signals could benefit more greatly from corroborative *in vivo* electrophysiological studies than the striatal vasoconstriction observed during several basal ganglia circuit manipulations. As discussed elsewhere (e.g., see Chapter 3 Discussion), neurovascular uncoupling has been previously reported in rodent striatum (215, 219); thus, in the absence of any electrophysiological data, only the most conservative interpretations can be made regarding neuronal contributions to striatal vasoconstriction. Ideally, the complementary electrophysiological examinations would take place simultaneously with fMRI data acquisition, a technical feat given the electrical noise introduced by the MR scanner environment. A suitable alternative would be to conduct electrophysiological studies outside the scanner in a separate group of animals, using identical anesthesia/sedative regimens and neural circuit stimulation protocols.

Pharmacological-fMRI Studies

Pharmacological-fMRI studies, combined with optogenetic tools, may allow for the generation of experiments to test the causal roles of dopaminergic and/or GABAergic signaling (among other transmission mechanism) in striatal vasoconstriction. For example, dopaminergic receptor antagonists may be injected acutely in the scanner following the observation of optogenetically-evoked striatal vasoconstriction. Modulation of the presence and/or intensity of the striatal fMRI signal post-drug may then be used to argue a role for the dopamine system in striatal vasoconstriction. Similarly, to test the role of lateral inhibitory mechanisms of action, pharmacological modulators of GABAergic signaling (eg., benzodiazepines), or histaminergic antagonists may be used (reported to selectively block lateral inhibition in striatum (66)). Although such experiments may provide corroborative evidence for a chosen hypothesis, this pharmacological-fMRI approach also suffers from caveats that will preclude definitive identification of a mechanism of striatal vasoconstriction. For example, as fMRI signals reflect changes from a hemodynamic baseline, any drug that persistently alters the baseline has the potential to induce a floor or ceiling effect regarding evoked fMRI signal changes. Pharmacological interrogations also generally suffer from varying levels of nonselectivity with respect to modulation of targeted vs. off-target circuits, an issue that may be reduced, but not eliminated by intracranial as opposed to systemic administration of the experimental compound. Finally, anecdotally, in many cases optogenetic-fMRI signals could not be reliably evoked across longer experimental scan sessions (i.e., optogenetic responses may dissipate, even when physiological parameters are within normal range and light-evoked

visual responses persist); this observation suggests that caution needs to be taken in the interpretation of drug-induced losses of optogenetically-evoked fMRI signals.

Selective Targeting Approaches for Optogenetic-fMRI

Many of the optogenetic experiments described in this work could generally benefit from more selective targeting of neuronal populations. This is particularly the case for the GPe and striatum, each of which holds large, intermingled populations of projection neurons that differ in both molecular phenotypes and input/output patterns. The fMRI signal reflects the spatially-summed activity within each voxel (with likely biased contributions from different classes of neurons; e.g., due to differing metabolic demand (119)); thus, when intermingled neuronal populations are simultaneously modulated (e.g., from optogenetic stimulation), cell-type-specific contributions to the resulting fMRI signal are exceedingly difficult to resolve. Even in cases such as with optogenetic-fMRI stimulation of the GPe (Chapter 4), wherein anatomical considerations provide relatively straightforward interpretations of downstream fMRI signal origins (i.e, prominent striatal vasoconstriction due to stimulation of striatum-projecting arkypallidal neurons), the independent contributions of other stimulated cell classes, as well as interactions between stimulated cell classes, cannot be easily ruled out. For example, with respect to the above example of optogenetic GPe stimulation, the observed striatal vasoconstriction could also be due to recruitment of STN-projecting prototypical GPe neurons via less straightforward polysynaptic route(s). Similarly, it would be highly informative to know the contributions of direct vs. indirect pathway MSNs to striatal stimulation-evoked vasoconstriction (see Chapter 5).

How can more selective opsin expression be achieved in these complex nuclei? In mice, which at present are far more genetically tractable than rats, the common approach is to employ transgenic animals in which recombination enzymes (e.g., Cre-recombinase) with germline transmission are placed under the gene promoter of interest. Viral vectors encoding recombination-inducible constructs then allow for straightforward targeting of selective cell populations. Unfortunately, such technology has generally been lacking in rats, where few such transgenic models are available (249). Some transgenic rat lines of interest (with respect to the present work) have been developed through the National Institute of Drug Addiction's Transgenic Rat Project (National Institutes of Health), including Cre-lines under the parvalbumin and dopamine D1 and D2 receptor promoters (<http://irp.drugabuse.gov/OTTC/rats.php>). Employing this parvalbumin-Cre line, it may be possible to selectively target prototypical neurons of the GPe; to the author's knowledge, no similar Cre lines exist for the complementary targeting of the arkypallidal GPe neurons (which are labeled by both Lim homeobox x-6 (Lhx6) and Npas1 (74, 75).

A second, conceptually similar approach is to target molecularly-defined neural subclasses using a selective gene promoter incorporated directly into the viral vector. For example, our motor cortical optogenetic-fMRI experiments took advantage of the CaMKII α promoter based on its ability to preferentially target excitatory principal cells in cortex (144). Although the flexibility of promoter choice using this approach is largely limited by gene size considerations (250), some useful viruses may be available for extending the present work. For example, Neumaier and colleagues have developed lentiviral vectors, encoding DREADD-based pharmacogenetic constructs (251), that selectively target direct and indirect pathway MSNs (via the use of enkephalin and dynorphin promoters,

respectively) (252). Pharmacogenetic-fMRI experiments using this viral vector, or optogenetic-fMRI experiments using a similar vector, may allow for the extension of our striatum circuit-mapping fMRI experiments (Chapter 5) to evaluate the contribution of both MSN subtypes in stimulation-evoked local vasoconstriction. Unfortunately, a pilot fMRI study using these lentiviral DREADD-encoding viruses was unsuccessful (data not shown).

Lastly, neuronal subclasses may be optogenetically-targeted based on their projection patterns, for example, via local stimulation of opsin-expressing fibers, or cell targeting using retrograde viral vectors (e.g., Cre-encoding canine adeno virus[CAV] (253)) infused in terminal fields. Using the former approach, I have demonstrated striatal vasoconstriction in response to optogenetic stimulation of the direct pathway striatonigral projection (see **Figure 5.2**). Although antidromic spiking following fiber stimulation may have, in principle, allowed for selective modulation of direct pathway MSNs in this experiment, the interpretability and physiological relevance of somatic activity induced in such a manner is debatable. The use of retrograde viral tools to induce somatic opsin expression (either directly or through the dual-targeting approach of terminal infusion of Cre-encoding retrograde viruses and cell body infusion of Cre-inducible opsin-encoding vectors (254)) is a more attractive approach. A pilot study by the author to induce Cre expression in direct and indirect pathway MSNs using this method was unsuccessful (data not shown). Future experimental attempts, perhaps using larger CAV viral volumes for GPe and SNr infusions (greater than 0.5ul), would be worth pursuing. This approach could also be easily employed for targeting the arkypallidal and prototypical GPe neurons by infusing the retrograde virus into the striatum or STN, respectively.

6.3 Summary

The studies described in this dissertation have employed preclinical fMRI measures of neural circuit and network connectivity, focusing on the basal ganglia network. Among the major findings of this work, we have reported that NAc-DBS may modulate neural circuits in a relatively frequency-insensitive manner (Chapter 2), and that striatal vasoconstriction is a broad consequence of activation of multiple basal ganglia circuit elements (motor cortical inputs, GPe, dorsal striatum). With respect to GPe stimulation-evoked striatal vasoconstriction (Chapter 4), we also report that this downstream response is modified in a widely used Parkinson's model. Future studies, particularly electrophysiological assessments, should aid considerably in determining the neuronal activity correlates of this disease-sensitive striatal fMRI signal.

APPENDIX 2.1: SUPPLEMENTAL MATERIALS FOR CHAPTER 2

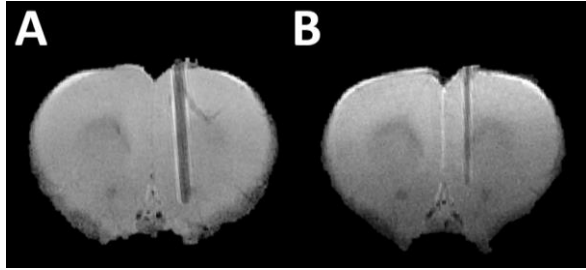


Figure S2.1. Representative T₂-weighted anatomical images displaying electrode placement in the NAc (**A**) and optic fiber placement above the NAc (**B**). Note the minimal electrode artifact with the tungsten microwire electrode.

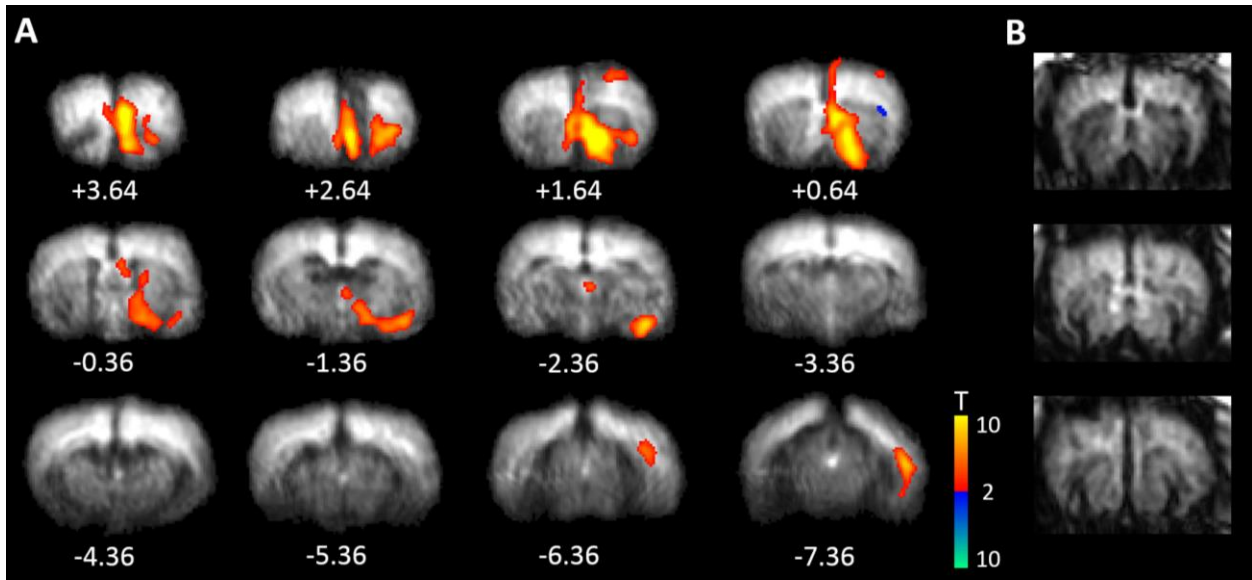


Figure S2.2. NAc-DBS-evoked functional activation maps (130 Hz; 300 μ A) overlaying on group-averaged EPI images ($n = 5$), presented on group-averaged EPI data (**A**). For comparison, the template-overlaid images are presented in **Figure 2.2B**. A sample of raw, unaveraged EPI images from 3 subjects is provided in (**B**). As we achieved robust evoked-fMRI responses in all animals, no data was discarded, including subject EPI data

displaying artifacts. Additional details regarding these images are located in the **Figure 2.2** caption.

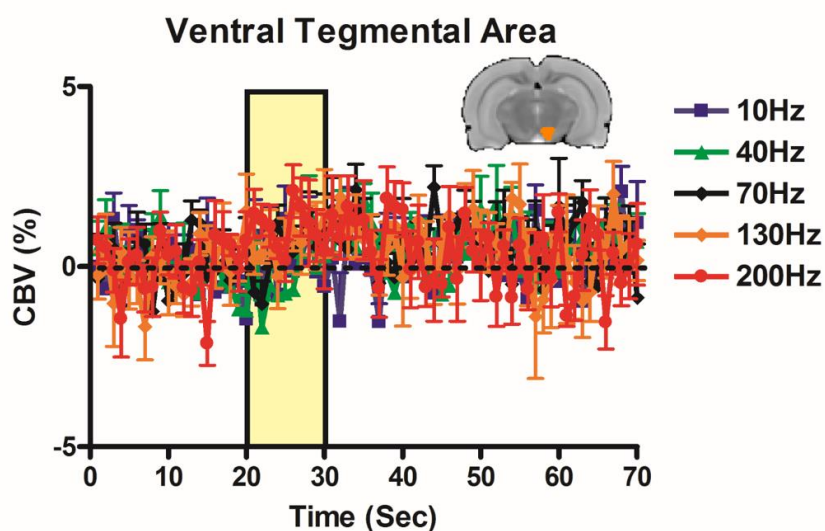


Figure S2.3. Temporal dynamics of VTA CBV responses to NAc-DBS across five stimulation frequencies (10, 40, 70, 130, 200 Hz; $n = 8$ per frequency) showing a lack of detectable evoked responses. All subjects were scanned with 500 μ A DBS, except one subject with 600 μ A. Additional details are provided in the **Figure 2.5** caption.

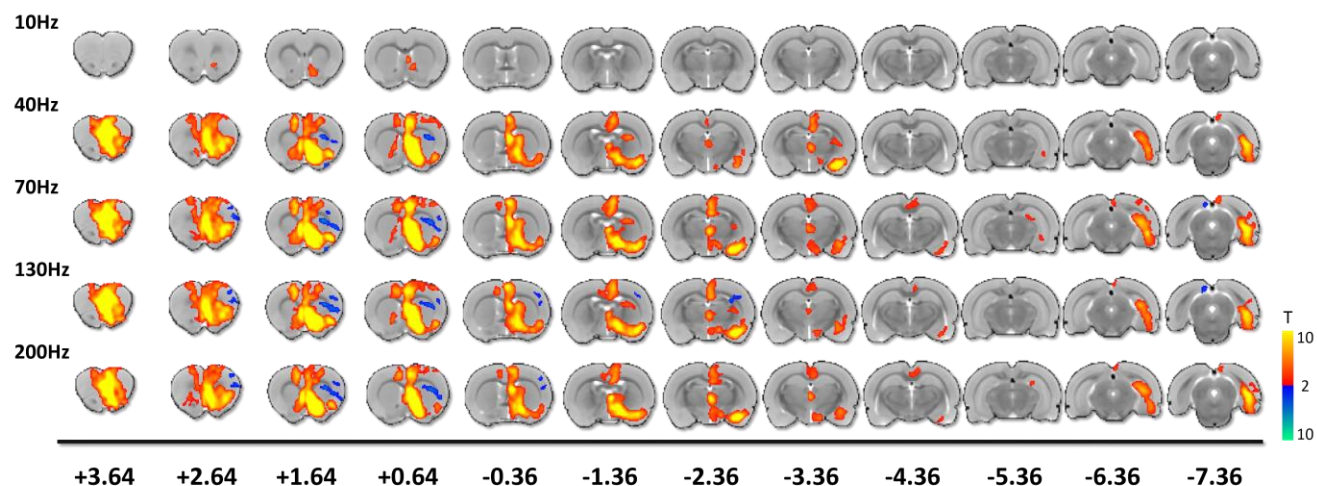


Figure S2.4. Functional activation maps of CBV modulation by NAc-DBS at 10, 40, 70, 200, and 400 Hz (500 μ A; except for one subject with 600 μ A) ($n = 8$ per frequency). NAc-DBS delivered at 10 Hz resulted in sparse CBV increases within and around the NAc.

DBS delivered at all other tested frequencies resulted in large-scale CBV modulation in both cortical and subcortical areas, which further were remarkably similar in spatial patterning across DBS frequencies (see also **Figure 2.5**). Additional details regarding these images are located in the **Figure 2.2** caption. Slice locations (reference to the Bregma in mm) are labeled at the bottom of the figure.

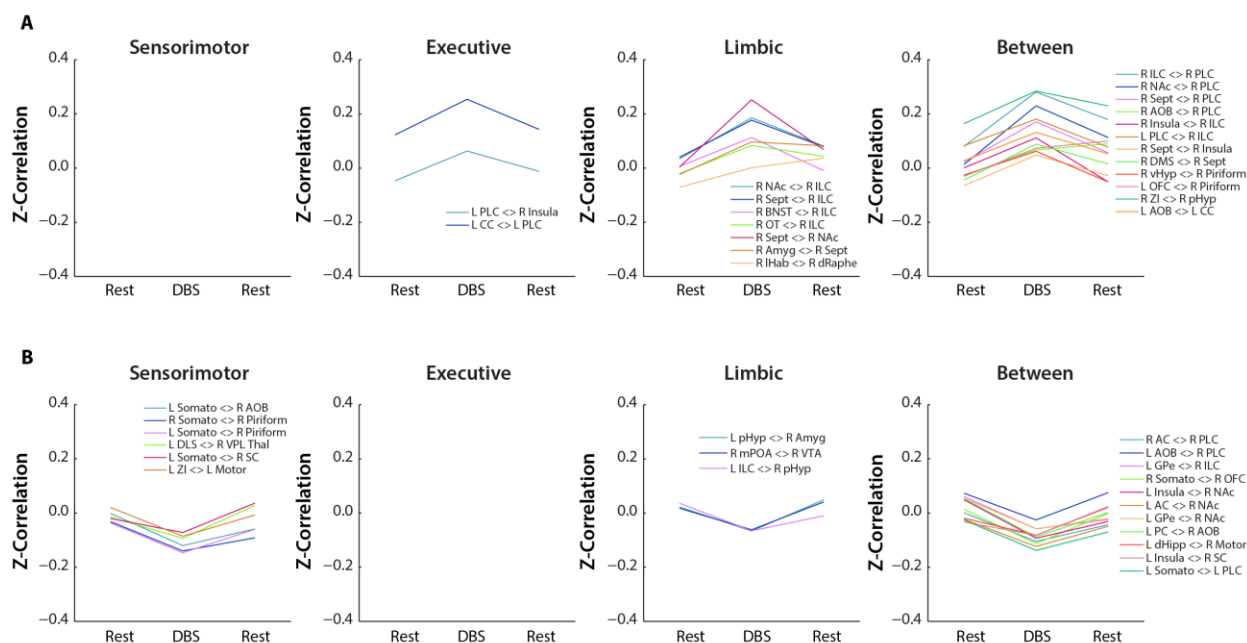


Figure S2.5. Network-level visualization of pair-wise fcMRI modulations during 130 Hz NAc-DBS. Significant (rANOVA, $p \leq 0.05$ uncorrected, $\Delta Z\text{-Corr} > 0.10$) individual pair-wise connections grouped by functionally-defined network (Sensorimotor, Executive, Limbic, and Between Network Connections) and plotted as Z-Correlation vs Stimulus Condition (Pre-DBS, DBS, Post-DBS). Pathways with enhanced connectivity are shown in **(A)** and suppressed connectivity are shown in **(B)**. Individual lines represent group means ($n = 7$).

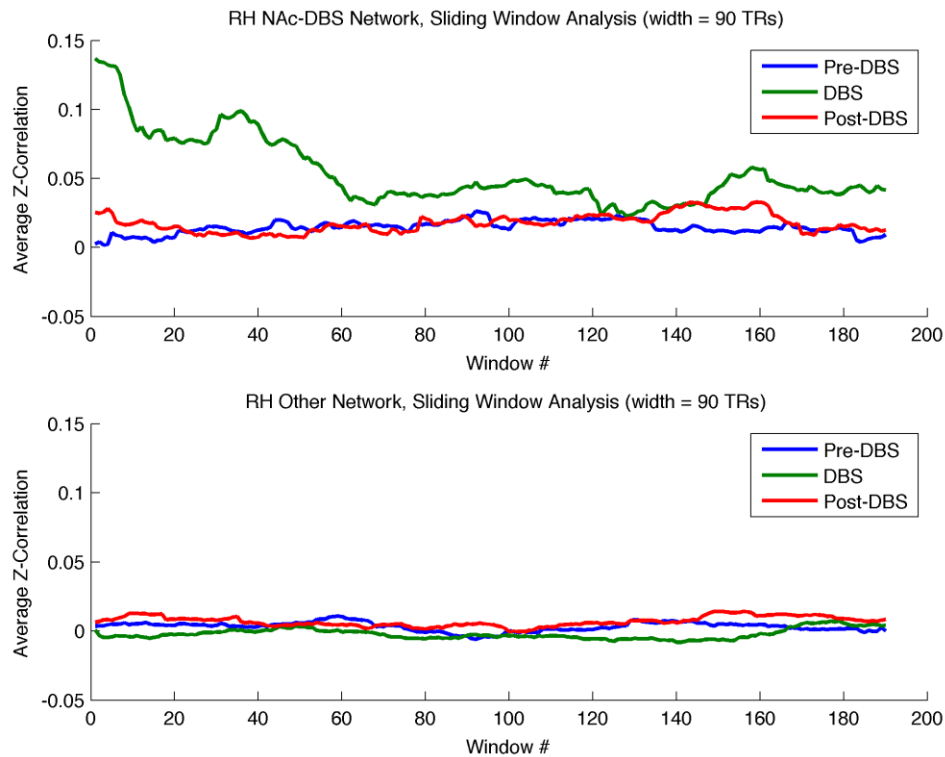


Figure S2.6. Sliding window analysis (90 s width; i.e., 1-90 s, 2-91 s...) of averaged z-correlations during the 130 Hz DBS stimulation fMRI scan period. This analysis was conducted for ROIs within the right hemisphere (RH), ipsilateral to the stimulation site. As described in the Methods, ROIs were separated into two separate networks: the NAc-DBS Network, and Other Network. Note that, for the NAc-DBS Network (top traces), average z-correlations (i.e., connectivity strength) generally remained higher for the DBS period compared to Pre/Post-DBS periods, and were highest at the onset of stimulation. However, no significant differences were detected between the first- and second-half of the data (paired t-test; $p > 0.05$). For the Other Network (bottom traces), there were no observable differences in connectivity strength between the DBS and Pre/Post periods.

APPENDIX 3.1: SUPPLEMENTAL MATERIALS FOR CHAPTER 2

Supplemental Figures

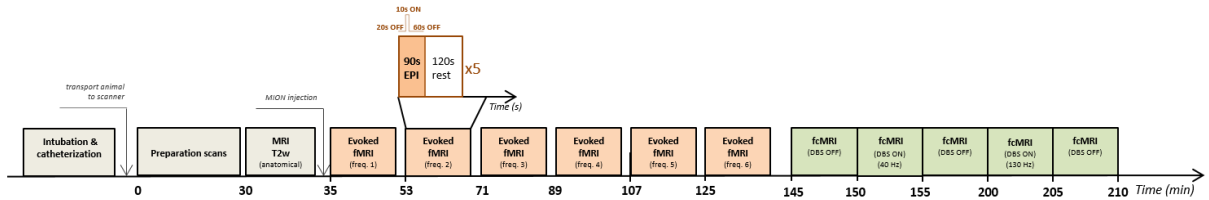


Figure S3.1. Experimental protocol. In preparation for fMRI procedures, rats were endotracheally intubated for mechanical ventilation and tail vein catheterization was applied for injection of the contrast agent (MION). Animals were then placed within a head-holder, and harnessed to a small animal cradle, after which they were transported to the MR scanner. Scanning started with a series of preparation scans to optimize location and magnetic field homogeneity. T₂-weighted images (T2w) were obtained for anatomical reference. Immediately prior to fMRI scan acquisition, rats were administered MION. A series of evoked fMRI scans with simultaneous DBS were obtained with a rest period of at least two minutes between each scan to allow for neurovascular recovery. Stimulation frequencies were varied in a pseudo-randomized order (freq. 1-6). Immediately following evoked fMRI scan acquisition, fcMRI scans were conducted in each subject. These scan series consisted of five, 5 minute scans during which either no stimulation or continuous DBS (40 or 130 Hz) was applied.

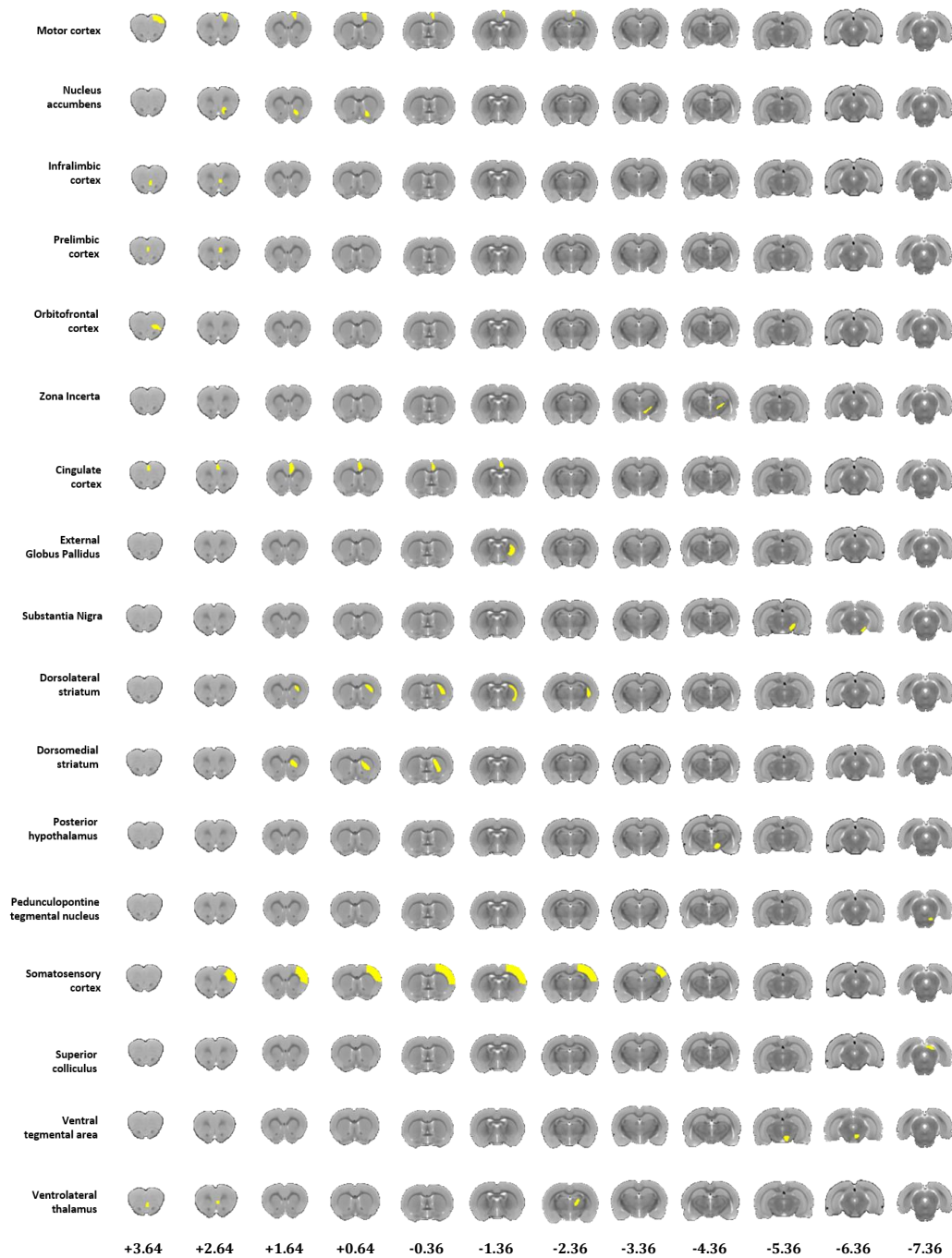


Figure S3.2. Seventeen anatomically-defined regions of interest (ROIs), used for the analysis of evoked-fMRI CBV traces (see **Figures 3.3-4, S3.6-7**), overlaid on the anatomical MR-template. Slice locations (reference to the Bregma in mm) are labeled at the bottom of the figure.

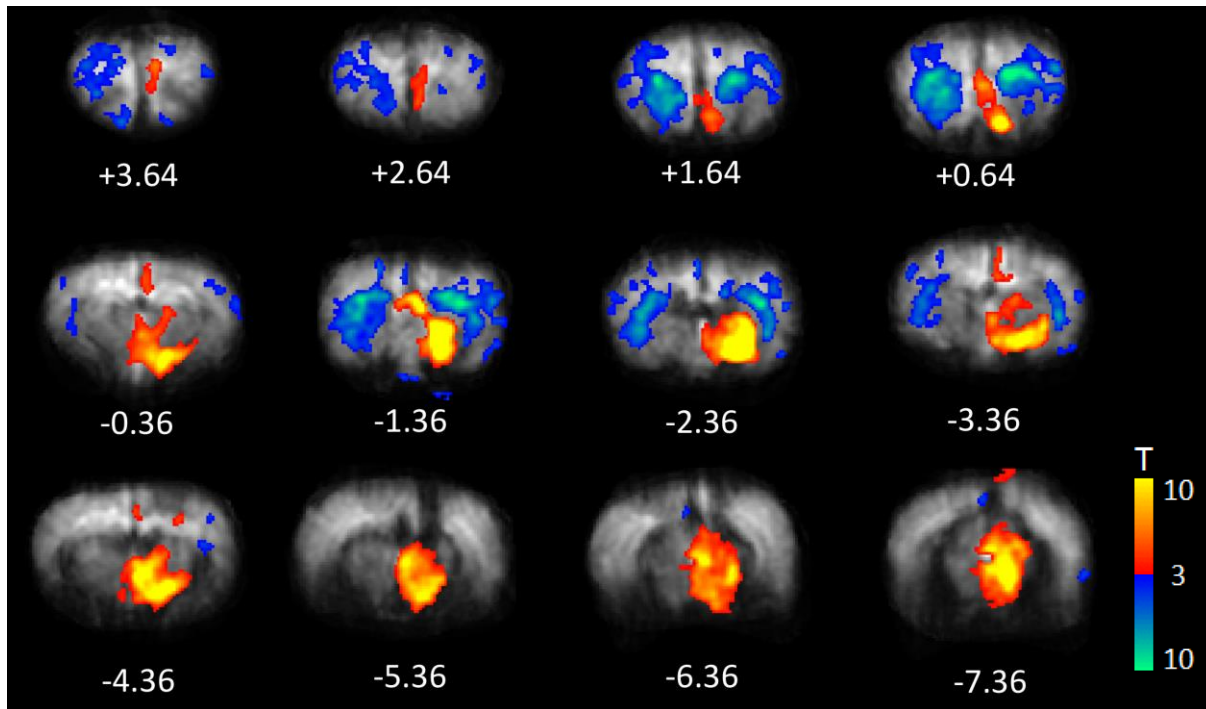


Figure S3.3. SNr-DBS-evoked functional activation maps (130 Hz) overlaying on representative group-averaged EPI images. For comparison, the template-overlaid images are presented in **Figure 3.2B**. Additional details regarding these images is located in the **Figure 3.2** caption. Numbers below each slice refer to anteroposterior slice location (reference to the Bregma in mm).

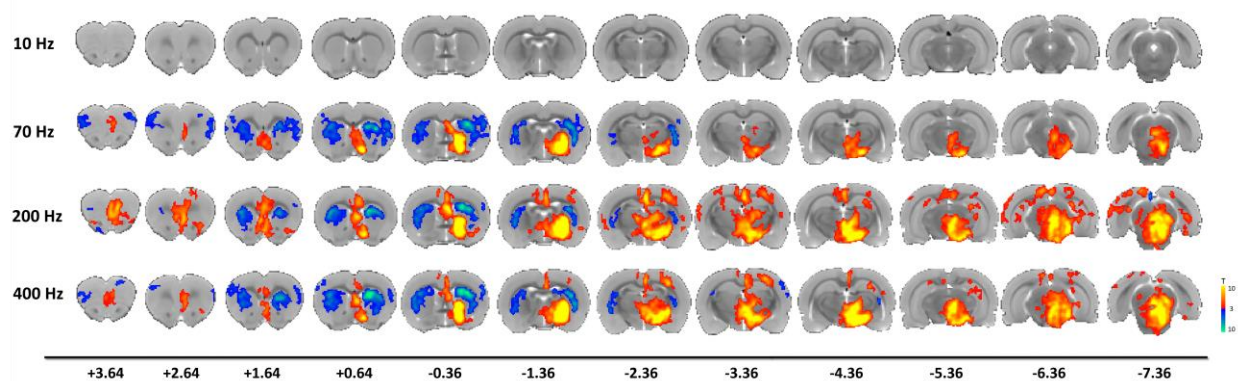


Figure S3.4. Functional activation maps of CBV modulation by SNr-DBS at 10, 70, 200, and 400 Hz. Note that SNr-DBS delivered at 10 Hz results in no significant CBV changes in any voxel. 70-200 Hz SNr-DBS resulted in CBV modulation within the targeted area as well as additional cortical and subcortical regions across the brain, including negative CBV signals within the striatum. Additional details regarding these images is located in the **Figure 3.2**

caption. Slice locations (reference to the Bregma in mm) are labeled at the bottom of the figure.

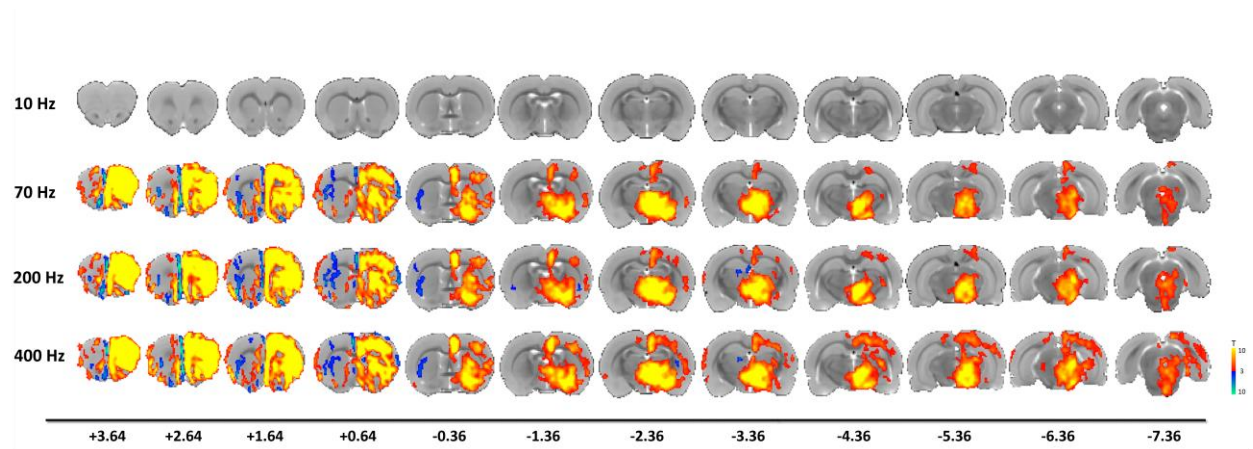


Figure S3.5. Functional activation maps of CBV modulation by GPe-DBS at 10, 70, 200, and 400 Hz. Note that GPe-DBS delivered at 10 Hz results in no significant CBV changes in any voxel. 70-200 Hz GPe-DBS resulted in CBV modulation within the targeted area as well as additional cortical and subcortical regions across the brain, including large prefrontal CBV increases and negative CBV signals within the striatum. Additional details regarding these images is located in the **Figure 3.2** caption. Slice locations (reference to the Bregma in mm) are labeled at the bottom of the figure.

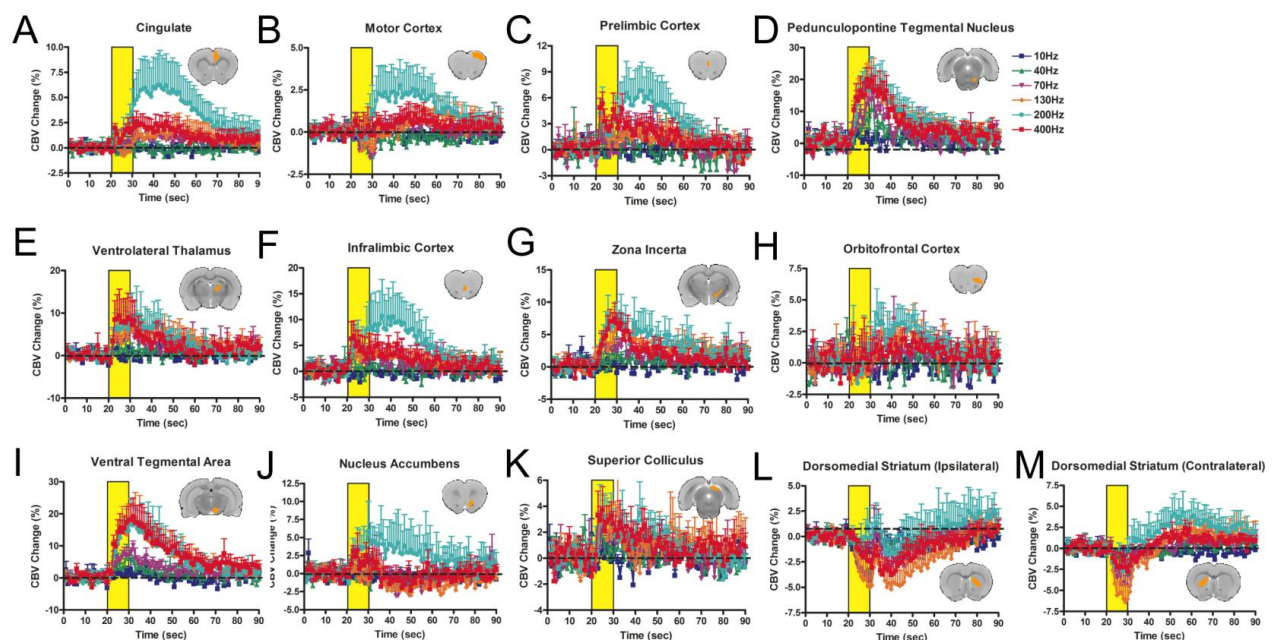


Figure S3.6. SNr-DBS evoked CBV changes at additional anatomically-defined regions of interest. (A) Cingulate (B) Motor cortex (C) Prelimbic cortex (D) Pedunclopontine tegmental nucleus (E) Ventrolateral thalamus (F) Infralimbic cortex (G) Zona incerta (H) Orbitofrontal cortex (I) Ventral tegmental area (J) Nucleus accumbens (K) Superior colliculus (L) Ipsilateral dorsomedial striatum (M) Contralateral dorsomedial striatum.

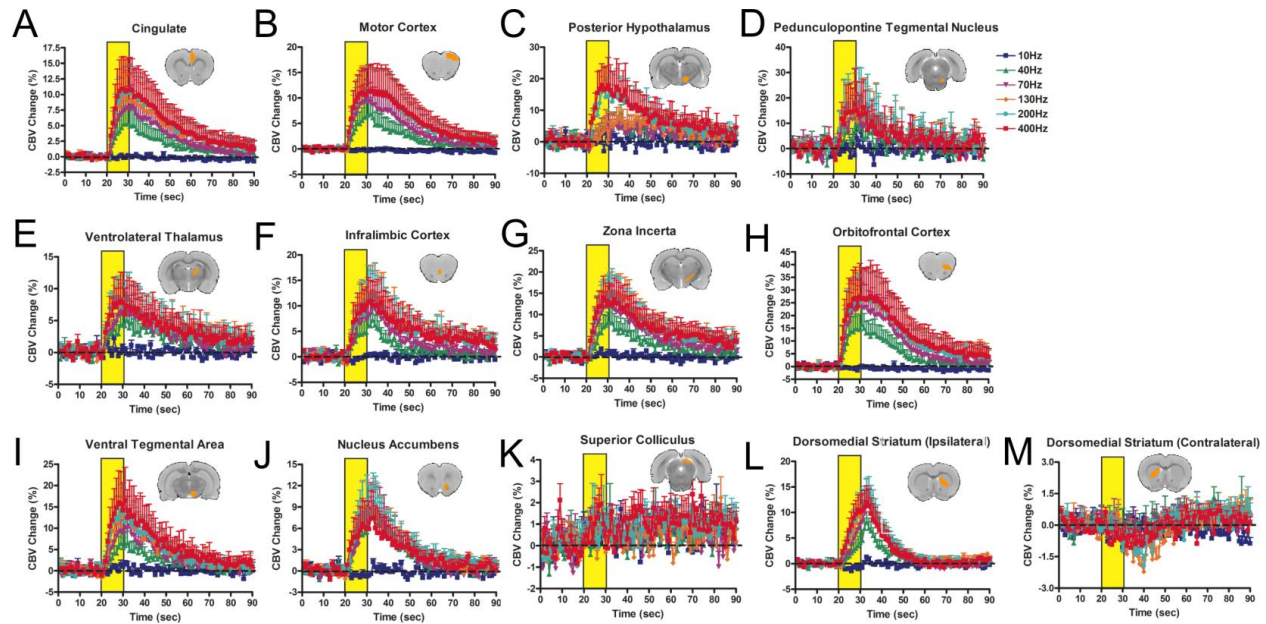


Figure S3.7. GPe-DBS evoked CBV changes at additional anatomically-defined regions of interest. (A) Cingulate (B) Motor cortex (C) Prelimbic cortex (D) Pedunclopontine tegmental nucleus (E) Ventrolateral thalamus (F) Infralimbic cortex (G) Zona incerta (H) Orbitofrontal cortex (I) Ventral tegmental area (J) Nucleus accumbens (K) Superior colliculus (L) Ipsilateral dorsomedial striatum (M) Contralateral dorsomedial striatum.

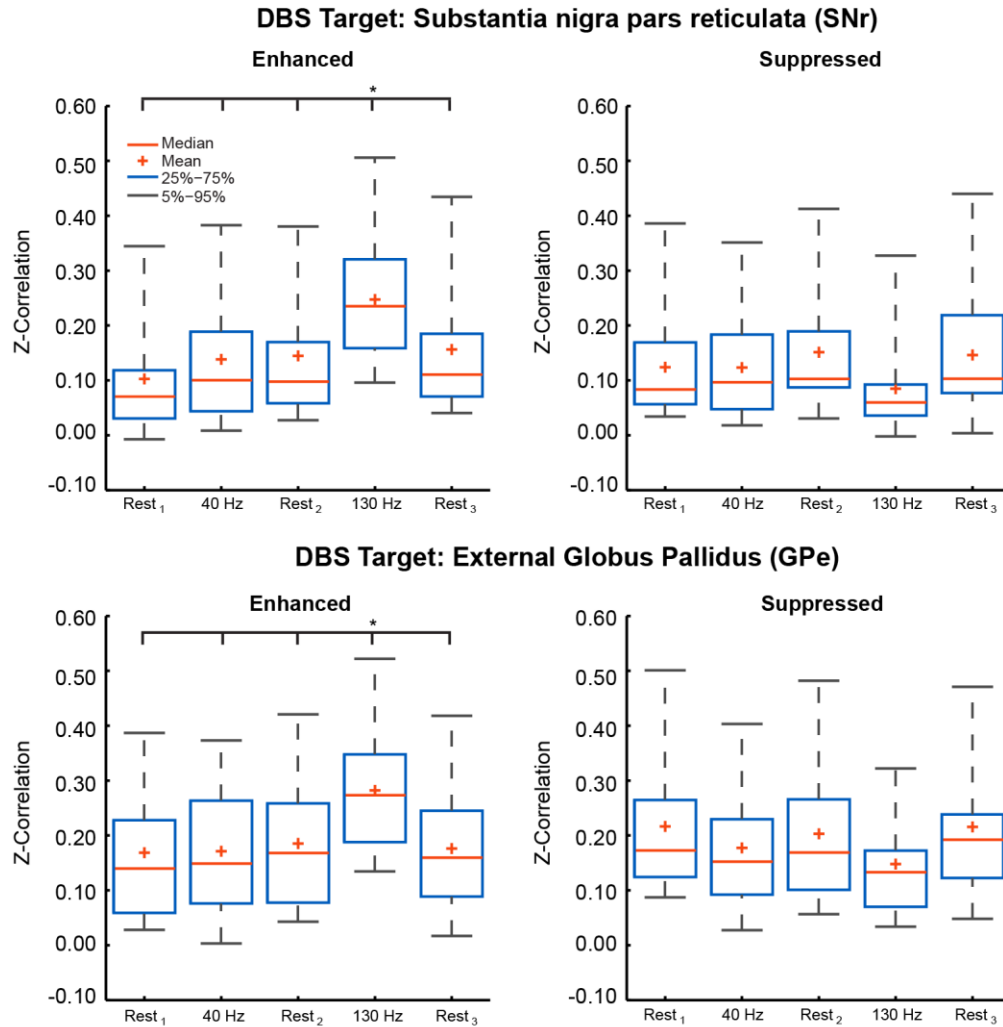


Figure S3.8. fcMRI Modulation via DBS of the SNr and GPe – without Global Signal Regression (GSR). Previously identified significant enhanced and suppressed connections (see **Figure 3.5B** and Supporting Material: **Supplemental Tables S3.1-2**) were re-analyzed using data without GSR in the pre-processing pipeline. The main-effect of condition for both DBS targets was maintained for enhanced but not for suppressed connections; SNr: $F_{\text{Enhanced}}(4,165) = 6.81, p < 0.001$ and $F_{\text{Suppressed}}(4,75) = 0.92, p = 0.460$; GPe: $F_{\text{Enhanced}}(4,190) = 5.71, p < 0.001$ and $F_{\text{Suppressed}}(4,190) = 1.85, p = 0.121$. For the enhanced connections, 130 Hz was significantly different from all other conditions for both DBS targets; * SNr $p \leq 0.016$, GPe $p \leq 0.006$.

Supplemental Tables

Table S3.1. SNr-DBS significantly (rANOVA, $p \leq 0.01$ uncorrected, $\Delta Z\text{-correlation} \geq 0.10$) modulated individual connections corresponding to **Figure 5A**. Data sorted based on

network grouping and modulation strength. ROI abbreviations are listed in **Figure 3.5 caption**.

DBS Target: Substantia nigra pars reticulata (SNr)

Enhancement - increased correlation								Connection		
Rest ₁	40Hz	Rest ₂	130Hz	Rest ₃	Δ	P-Value	Connection	Ipsilateral	ROI	Contralateral
-0.01	0.06	-0.01	0.29	-0.02	0.31	5.76E-03	33 21 1	1	PLC	46
-0.02	0.02	-0.01	0.20	0.00	0.22	1.97E-03	39 21 1	2	ILC	47
0.08	0.03	0.07	0.23	0.08	0.20	7.66E-03	39 33 1	3	OFC	48
-0.02	0.02	-0.07	0.11	0.04	0.18	5.09E-03	77 64 1	4	CC	49
-0.10	0.02	-0.05	0.03	-0.04	0.13	8.61E-03	84 72 1	5	Insula	50
0.07	0.02	0.07	0.15	0.06	0.13	7.52E-03	83 61 1	6	NAC	51
-0.04	0.00	-0.06	0.05	0.01	0.11	7.53E-03	62 29 1	7	AS	52
0.04	0.04	0.05	0.13	-0.02	0.14	9.28E-03	49 48 2	8	vPall	53
-0.08	-0.03	0.01	-0.03	0.06	0.15	4.27E-03	60 2 3	9	Sept	54
0.00	0.00	0.00	0.04	-0.10	0.14	8.86E-04	54 23 3	10	lHyp	55
0.02	-0.01	0.00	0.12	0.01	0.13	4.79E-03	90 43 3	11	Amyg	56
-0.02	-0.05	-0.02	0.07	0.01	0.12	4.34E-03	45 12 3	12	BNST	57
-0.10	-0.04	0.01	0.12	-0.02	0.22	8.79E-03	85 77 4	13	MDT	58
-0.05	0.03	-0.04	0.17	-0.04	0.22	4.53E-05	28 5 4	14	vHipp	59
-0.01	0.07	-0.09	0.12	-0.07	0.21	2.82E-05	15 5 4	15	VTA	60
0.00	0.15	-0.01	0.03	-0.05	0.19	7.96E-03	31 18 4	16	AD	61
-0.05	0.02	-0.02	0.14	-0.04	0.19	9.84E-03	15 3 4	17	AOB	62
-0.08	-0.05	-0.04	0.10	-0.02	0.18	8.01E-03	85 63 4	18	DLS	63
-0.01	0.01	-0.02	0.16	-0.01	0.18	1.28E-03	31 21 4	19	DMS	64
0.00	0.01	-0.02	0.14	-0.01	0.16	6.46E-03	25 3 4	20	ENT	65
0.00	0.01	-0.02	0.12	-0.04	0.16	4.74E-03	28 3 4	21	GPe	66
0.00	-0.09	-0.05	0.06	-0.08	0.15	1.35E-03	63 42 4	22	Motor	67
-0.05	0.01	-0.06	0.09	0.03	0.15	4.11E-03	84 69 4	23	OT	68
-0.04	0.00	-0.05	0.10	-0.03	0.14	1.44E-03	55 4 4	24	PAG	69
-0.05	-0.06	0.01	0.08	0.01	0.14	9.49E-03	17 15 4	25	PPtg	70
-0.06	-0.01	0.00	0.08	-0.01	0.13	1.15E-03	68 66 4	26	PC	71
0.18	0.21	0.17	0.30	0.26	0.13	6.23E-03	83 71 4	27	Piriform	72
-0.03	-0.03	-0.03	0.09	-0.01	0.12	7.32E-04	30 28 4	28	pHyp	73
-0.03	0.00	0.00	0.08	0.01	0.11	3.71E-03	40 9 4	29	pThal	74
-0.05	-0.05	0.03	0.03	0.07	0.11	1.42E-03	83 23 4	30	S2	75
-0.02	0.06	0.03	0.09	0.03	0.11	6.12E-03	43 1 4	31	SN	76
-0.07	-0.02	-0.04	0.04	0.04	0.11	1.86E-03	67 51 4	32	Somato	77
-0.06	-0.01	-0.01	0.05	0.00	0.11	9.74E-03	52 22 4	33	STN	78
-0.03	-0.03	-0.02	0.03	0.07	0.10	5.70E-03	44 9 4	34	TeA	79
Suppression - increased anti-correlation								35	VL	80
0.01	0.04	-0.09	-0.06	-0.03	0.13	4.21E-03	32 25 1	36	VPL Thal	81
0.00	0.03	-0.02	-0.09	-0.04	0.12	2.35E-03	70 32 1	37	VPM	82
-0.04	0.00	-0.08	-0.14	-0.07	0.14	7.08E-03	50 26 2	38	Visual	83
0.03	0.00	0.01	-0.12	0.02	0.15	6.31E-03	55 28 3	39	ZI	84
0.02	-0.03	0.07	-0.01	0.00	0.10	2.96E-03	73 65 3	40	dHipp	85
0.08	-0.03	0.12	-0.08	0.05	0.20	5.15E-04	77 5 4	41	dRaphe	86
0.09	0.03	0.10	-0.09	-0.01	0.19	6.79E-03	66 5 4	42	lHab	87
0.02	0.01	0.05	-0.12	0.04	0.17	3.20E-03	63 3 4	43	mPOA	88
0.06	-0.04	-0.04	-0.03	-0.11	0.17	1.54E-03	63 41 4	44	SC	89
-0.07	0.00	-0.06	-0.16	-0.04	0.16	7.03E-03	32 13 4	45	vHyp	90
-0.02	-0.01	0.06	-0.09	0.07	0.16	3.45E-03	55 39 4	Network		
-0.01	-0.01	0.02	-0.10	0.01	0.12	4.25E-03	84 11 4	1	Sensorimotor	
-0.05	0.02	-0.05	-0.09	0.03	0.12	4.99E-03	48 24 4	2	Executive	
0.01	-0.09	0.01	-0.10	-0.04	0.11	3.65E-03	45 19 4	3	Limbic	
-0.05	-0.03	0.00	-0.08	0.02	0.10	3.95E-03	56 5 4	4	Between	
0.00	-0.01	0.03	-0.07	-0.05	0.10	8.34E-03	87 75 4			

Table S3.2. GPe-DBS significantly (rANOVA, $p \leq 0.01$ uncorrected, $\Delta Z\text{-correlation} \geq 0.10$) modulated individual connections corresponding to **Figure 5A**. Data sorted based on network grouping and modulation strength. ROI abbreviations are listed in **Figure 5 caption**.

DBS Target: External Globus Pallidus (GPe)

Enhancement - increased correlation								Connection		
Rest ₁	40Hz	Rest ₂	130Hz	Rest ₃	Δ	P-Value		Connection	ROI	Contralateral
0.05	0.08	0.07	0.27	0.03	0.24	6.51E-03	38	16	1	PLC
-0.03	-0.04	-0.02	0.19	0.00	0.24	2.06E-03	39	22	1	ILC
-0.03	-0.01	-0.02	0.14	-0.03	0.18	3.88E-03	77	16	1	OFC
-0.06	0.01	-0.06	0.10	-0.03	0.16	5.35E-03	77	64	1	CC
0.04	0.03	0.02	0.18	0.02	0.16	3.05E-03	61	38	1	Insula
0.03	-0.03	-0.05	0.10	-0.03	0.15	4.92E-03	33	22	1	NAc
-0.06	0.06	-0.01	-0.02	-0.09	0.15	4.30E-04	62	39	1	AS
0.17	0.19	0.10	0.22	0.18	0.12	2.23E-03	66	63	1	vPall
0.05	0.01	0.03	0.18	0.05	0.18	3.47E-04	31	15	3	Sept
-0.04	-0.03	-0.05	0.08	0.00	0.13	7.92E-03	15	2	3	lHyp
-0.04	0.01	0.02	0.09	0.03	0.13	6.32E-03	58	11	3	lHyp
-0.07	0.01	0.06	0.02	-0.01	0.12	6.89E-03	68	42	3	BNST
0.00	-0.04	0.00	0.06	-0.03	0.11	5.82E-03	42	2	3	MDT
0.00	-0.03	0.04	0.27	0.04	0.31	3.10E-03	22	5	4	vHipp
0.00	-0.03	-0.01	0.14	-0.06	0.21	2.91E-03	39	5	4	VTA
0.00	-0.02	-0.03	0.17	-0.02	0.19	1.85E-04	10	5	4	AC
-0.02	0.01	0.00	0.15	-0.02	0.18	2.68E-03	33	5	4	AOB
-0.05	0.02	0.03	0.12	0.00	0.17	1.42E-05	39	12	4	DLS
-0.03	-0.07	-0.03	0.10	0.00	0.17	3.17E-04	15	3	4	DMS
-0.03	0.02	-0.06	0.11	-0.01	0.16	5.71E-03	22	15	4	ENT
0.16	0.20	0.15	0.31	0.16	0.16	3.86E-03	33	28	4	GPe
-0.06	0.00	-0.01	0.09	0.01	0.15	5.88E-03	28	3	4	Motor
0.01	0.00	0.03	0.15	0.00	0.15	5.88E-03	27	7	4	OT
-0.03	-0.02	-0.02	0.12	-0.02	0.14	6.00E-03	59	38	4	PAG
-0.08	-0.11	-0.07	0.03	-0.10	0.14	4.60E-03	77	51	4	PPig
-0.10	-0.14	-0.07	-0.01	-0.08	0.13	1.33E-03	85	51	4	PC
-0.04	-0.05	-0.06	0.07	-0.03	0.13	7.99E-03	41	27	4	Pinform
0.01	0.06	0.07	0.14	0.04	0.13	1.85E-03	68	62	4	pHyp
-0.08	-0.07	-0.03	0.05	-0.07	0.13	2.06E-03	64	14	4	pThal
-0.09	-0.12	0.00	0.00	-0.04	0.12	4.00E-03	63	40	4	S2
-0.04	-0.01	-0.05	0.07	-0.04	0.12	1.84E-03	85	77	4	SN
0.01	0.02	0.00	0.05	-0.07	0.12	9.66E-04	74	43	4	Somato
-0.08	0.03	0.04	0.00	-0.02	0.11	1.10E-03	68	49	4	STN
-0.08	0.03	0.03	0.02	-0.02	0.11	2.42E-03	84	14	4	TaA
-0.06	0.00	0.00	0.05	0.00	0.11	1.81E-03	71	20	4	VL
-0.06	-0.01	-0.08	0.03	-0.04	0.11	4.93E-03	77	65	4	VPL Thal
-0.04	0.03	-0.07	0.03	-0.06	0.10	5.81E-03	87	85	4	VPM
-0.06	-0.07	-0.03	0.04	-0.06	0.10	4.41E-03	85	62	4	Visual
-0.01	-0.03	-0.02	0.05	0.07	0.10	7.58E-03	85	57	4	ZI
Suppression - increased anti-correlation										
Rest ₁	40Hz	Rest ₂	130Hz	Rest ₃	Δ	P-Value		Connection	ROI	Contralateral
0.23	0.20	0.20	-0.04	0.19	0.27	1.49E-03	77	32	1	
-0.02	-0.06	0.04	-0.18	-0.03	0.22	1.62E-03	61	22	1	
-0.04	-0.01	-0.05	-0.22	-0.01	0.21	1.25E-03	38	22	1	
0.08	0.03	0.05	-0.11	0.01	0.19	5.67E-03	67	22	1	
0.02	-0.02	0.01	-0.15	0.00	0.17	1.53E-03	39	38	1	
-0.05	-0.02	-0.08	-0.19	-0.06	0.17	2.71E-04	83	22	1	
0.01	-0.06	-0.01	0.01	0.08	0.15	7.21E-03	75	64	1	
0.01	0.00	-0.04	-0.10	0.04	0.14	3.21E-04	38	33	1	
0.05	-0.02	-0.08	0.01	0.01	0.13	2.90E-04	74	16	1	
0.04	0.02	-0.07	-0.05	-0.01	0.12	5.08E-03	83	37	1	
-0.01	0.02	0.06	-0.04	0.03	0.10	9.98E-03	44	37	1	
-0.06	-0.02	-0.02	-0.18	-0.04	0.16	4.19E-03	71	5	2	
-0.15	-0.09	-0.14	-0.24	-0.20	0.15	8.23E-03	85	5	2	
0.03	0.13	0.06	0.00	0.01	0.13	7.32E-03	88	68	3	
0.05	-0.06	0.00	-0.06	0.06	0.13	9.49E-04	65	2	3	
0.00	-0.03	-0.03	-0.12	-0.05	0.12	2.42E-03	59	8	3	
0.02	-0.07	-0.01	-0.06	0.04	0.11	1.17E-03	58	12	3	
-0.02	-0.07	-0.02	-0.26	-0.05	0.24	5.72E-03	38	5	4	
0.06	0.06	0.06	-0.18	0.03	0.24	4.67E-05	77	5	4	
0.07	0.00	-0.01	-0.16	-0.04	0.23	8.59E-04	38	28	4	
-0.05	-0.07	0.01	-0.16	0.05	0.21	1.06E-05	77	15	4	
-0.07	-0.04	-0.04	-0.21	-0.02	0.19	1.37E-03	16	3	4	
0.03	-0.06	-0.02	-0.15	-0.03	0.18	1.09E-03	71	22	4	
-0.05	0.02	0.00	-0.14	-0.01	0.16	2.57E-03	22	20	4	
0.01	0.05	-0.02	-0.11	0.02	0.16	2.81E-03	81	15	4	
-0.12	-0.04	-0.03	-0.19	-0.05	0.16	5.09E-03	61	5	4	
-0.02	-0.01	0.00	-0.15	0.00	0.16	9.54E-03	38	10	4	
-0.03	-0.03	-0.03	-0.18	-0.04	0.15	3.42E-03	85	22	4	
0.05	0.01	-0.02	-0.10	0.03	0.15	4.43E-03	85	15	4	
0.06	0.03	0.03	-0.08	0.05	0.14	6.31E-03	39	14	4	
0.01	0.04	-0.02	-0.10	0.03	0.14	9.58E-04	31	16	4	
-0.02	0.04	0.00	-0.10	-0.02	0.13	6.48E-03	34	22	4	
0.04	-0.05	0.01	-0.09	0.00	0.13	5.55E-03	24	21	4	
-0.01	-0.11	0.01	-0.04	0.02	0.13	7.19E-03	65	21	4	
0.07	-0.05	0.01	-0.05	-0.02	0.12	1.21E-03	81	31	4	
-0.05	0.01	0.04	-0.07	-0.02	0.11	9.04E-03	77	24	4	
0.01	0.01	0.03	-0.08	0.03	0.11	3.03E-03	72	5	4	
0.08	0.03	0.00	-0.02	-0.02	0.10	2.88E-03	81	41	4	
0.02	0.02	-0.04	-0.05	-0.08	0.10	4.23E-03	84	3	4	

Network	
1	Sensorimotor
2	Executive
3	Limbic
4	Between

Table S3.3. Summary statistics for post-hoc comparison (two-sample t-tests: Rest vs. 40 Hz, Rest vs. 130 Hz, and 40 Hz vs. 130 Hz) across significantly modulated connections (**Table S3.1 and S3.2**) grouped by DBS target (SNr and GPe) and modulation direction (Enhanced: increased correlation; Suppressed: increased anti-correlation).

DBS Target: Substantia nigra pars reticulata (SNr)

Enhancement - increased correlation

t-test	df	t	p-value
Rest vs 40 Hz	134	-1.56	1.20E-01
Rest vs 130 Hz	134	-9.70	3.51E-17
40 Hz vs 130 Hz	66	-6.20	4.10E-08

Suppression - increased anti-correlation

t-test	df	t	p-value
Rest vs 40 Hz	62	0.58	5.63E-01
Rest vs 130 Hz	62	6.42	2.14E-08
40 Hz vs 130 Hz	30	6.33	5.63E-07

DBS Target: External Globus Pallidus (GPe)

Enhancement - increased correlation

t-test	df	t	p-value
Rest vs 40 Hz	154	-0.79	4.30E-01
Rest vs 130 Hz	154	-9.74	9.07E-18
40 Hz vs 130 Hz	76	-6.26	2.06E-08

Suppression - increased anti-correlation

t-test	df	t	p-value
Rest vs 40 Hz	154	0.70	4.82E-01
Rest vs 130 Hz	154	10.00	1.83E-18
40 Hz vs 130 Hz	76	7.23	3.28E-10

REFERENCES

1. J. M. Deniau, P. Mailly, N. Maurice, S. Charpier, The pars reticulata of the substantia nigra: a window to basal ganglia output. *Progress in brain research* **160**, 151-172 (2007)10.1016/s0079-6123(06)60009-5).
2. A. Dahlström, K. Fuxe, Evidence for the existence of monoamine-containing neurons in the central nervous system. I. Demonstration of monoamines in the cell bodies of brain stem neurons. *Acta Physiologica Scandinavica. Supplementum*, SUPPL 232: 231 (1964).
3. M. A. Basso, M. A. Sommer, Exploring the role of the substantia nigra pars reticulata in eye movements. *Neuroscience* **198**, 205-212 (2011); published online EpubDec 15 (10.1016/j.neuroscience.2011.08.026).
4. H. H. Yin, B. J. Knowlton, The role of the basal ganglia in habit formation. *Nature reviews. Neuroscience* **7**, 464-476 (2006); published online EpubJun (10.1038/nrn1919).
5. R. S. Turner, M. Desmurget, Basal ganglia contributions to motor control: a vigorous tutor. *Current opinion in neurobiology* **20**, 704-716 (2010); published online EpubDec (10.1016/j.conb.2010.08.022).
6. L. Tremblay, Y. Worbe, S. Thobois, V. Sgambato-Faure, J. Feger, Selective dysfunction of basal ganglia subterritories: From movement to behavioral disorders. *Movement disorders : official journal of the Movement Disorder Society* **30**, 1155-1170 (2015); published online EpubAug (10.1002/mds.26199).
7. M. Jahanshahi, I. Obeso, J. C. Rothwell, J. A. Obeso, A fronto-striato-subthalamic-pallidal network for goal-directed and habitual inhibition. *Nature reviews. Neuroscience* **16**, 719-732 (2015); published online EpubDec (10.1038/nrn4038).
8. M. R. DeLong, T. Wichmann, Circuits and circuit disorders of the basal ganglia. *Archives of neurology* **64**, 20-24 (2007); published online EpubJan (10.1001/archneur.64.1.20).
9. L. Ding, Joshua I. Gold, The Basal Ganglia's Contributions to Perceptual Decision Making. *Neuron* **79**, 640-649 (2013)10.1016/j.neuron.2013.07.042)

10. A. H. Gittis, A. C. Kreitzer, Striatal microcircuitry and movement disorders. *Trends in neurosciences* **35**, 557-564 (2012); published online EpubSep (10.1016/j.tins.2012.06.008).
11. O. Hikosaka, H. F. Kim, M. Yasuda, S. Yamamoto, Basal ganglia circuits for reward value-guided behavior. *Annual review of neuroscience* **37**, 289-306 (2014)10.1146/annurev-neuro-071013-013924).
12. G. M. Shepherd, Corticostriatal connectivity and its role in disease. *Nature reviews. Neuroscience* **14**, 278-291 (2013); published online EpubApr (10.1038/nrn3469).
13. A. Mathai, Y. Smith, The corticostriatal and corticosubthalamic pathways: two entries, one target. So what? *Frontiers in systems neuroscience* **5**, 64 (2011)10.3389/fnsys.2011.00064).
14. M. Morishima, Y. Kawaguchi, Recurrent connection patterns of corticostriatal pyramidal cells in frontal cortex. *The Journal of neuroscience : the official journal of the Society for Neuroscience* **26**, 4394-4405 (2006); published online EpubApr 19 (10.1523/JNEUROSCI.0252-06.2006).
15. C. Rock, H. Zurita, C. Wilson, A. junior Apicella, An inhibitory corticostriatal pathway. *eLife* **5**, e15890 (2016).
16. A. Flaherty, A. M. Graybiel, Input-output organization of the sensorimotor striatum in the squirrel monkey. *The Journal of neuroscience* **14**, 599-610 (1994).
17. A. Ebrahimi, R. Pochet, M. Roger, Topographical organization of the projections from physiologically identified areas of the motor cortex to the striatum in the rat. *Neuroscience research* **14**, 39-60 (1992).
18. G. E. Alexander, M. R. DeLong, P. L. Strick, Parallel organization of functionally segregated circuits linking basal ganglia and cortex. *Annual review of neuroscience* **9**, 357-381 (1986).
19. N. R. Wall, M. De La Parra, E. M. Callaway, A. C. Kreitzer, Differential Innervation of Direct- and Indirect-Pathway Striatal Projection Neurons. *Neuron*, (2013); published online EpubJun 25 (10.1016/j.neuron.2013.05.014).

20. S. Lapper, J. Bolam, Input from the frontal cortex and the parafascicular nucleus to cholinergic interneurons in the dorsal striatum of the rat. *Neuroscience* **51**, 533-545 (1992).
21. G. J. Kress, N. Yamawaki, D. L. Wokosin, I. R. Wickersham, G. M. G. Shepherd, D. J. Surmeier, Convergent cortical innervation of striatal projection neurons. *Nature neuroscience* **16**, 665-667 (2013)10.1038/nn.3397).
22. S. Jahfari, L. Waldorp, W. P. van den Wildenberg, H. S. Scholte, K. R. Ridderinkhof, B. U. Forstmann, Effective connectivity reveals important roles for both the hyperdirect (fronto-subthalamic) and the indirect (fronto-striatal-pallidal) fronto-basal ganglia pathways during response inhibition. *The Journal of neuroscience : the official journal of the Society for Neuroscience* **31**, 6891-6899 (2011); published online EpubMay 4 (10.1523/JNEUROSCI.5253-10.2011).
23. A. Nambu, H. Tokuno, M. Takada, Functional significance of the cortico-subthalamo-pallidal 'hyperdirect' pathway. *Neuroscience research* **43**, 111-117 (2002).
24. T. Kita, H. Kita, The subthalamic nucleus is one of multiple innervation sites for long-range corticofugal axons: a single-axon tracing study in the rat. *The Journal of neuroscience : the official journal of the Society for Neuroscience* **32**, 5990-5999 (2012); published online EpubApr 25 (10.1523/JNEUROSCI.5717-11.2012).
25. S. Kitai, J. Deniau, Cortical inputs to the subthalamus: intracellular analysis. *Brain research* **214**, 411-415 (1981).
26. W. I. Haynes, S. N. Haber, The organization of prefrontal-subthalamic inputs in primates provides an anatomical substrate for both functional specificity and integration: implications for Basal Ganglia models and deep brain stimulation. *The Journal of neuroscience : the official journal of the Society for Neuroscience* **33**, 4804-4814 (2013); published online EpubMar 13 (10.1523/JNEUROSCI.4674-12.2013).
27. T. J. Ellender, J. Harwood, P. Kosillo, M. Capogna, J. P. Bolam, Heterogeneous properties of central lateral and parafascicular thalamic synapses in the striatum. *The Journal of physiology* **591**, 257-272 (2013); published online EpubJan 1 (10.1113/jphysiol.2012.245233).
28. Y. Smith, A. Galvan, T. J. Ellender, N. Doig, R. M. Villalba, I. Huerta-Ocampo, T. Wichmann, J. P. Bolam, The thalamostriatal system in normal and diseased states. *Frontiers in systems neuroscience* **8**, 5 (2014)10.3389/fnsys.2014.00005).

29. A. Galvan, Y. Smith, The primate thalamostriatal systems: Anatomical organization, functional roles and possible involvement in Parkinson's disease. *Basal ganglia* **1**, 179-189 (2011); published online EpubNov 1 (10.1016/j.baga.2011.09.001).
30. M. Castle, M. S. Aymerich, C. Sanchez-Escobar, N. Gonzalo, J. A. Obeso, J. L. Lanciego, Thalamic innervation of the direct and indirect basal ganglia pathways in the rat: Ipsi- and contralateral projections. *The Journal of comparative neurology* **483**, 143-153 (2005); published online EpubMar 7 (10.1002/cne.20421).
31. J. M. Tepper, T. Koos, C. J. Wilson, GABAergic microcircuits in the neostriatum. *Trends in neurosciences* **27**, 662-669 (2004); published online EpubNov (10.1016/j.tins.2004.08.007).
32. A. C. Kreitzer, Physiology and pharmacology of striatal neurons. *Annual review of neuroscience* **32**, 127-147 (2009)10.1146/annurev.neuro.051508.135422).
33. H. Steiner, C. R. Gerfen, Role of dynorphin and enkephalin in the regulation of striatal output pathways and behavior. *Experimental Brain Research* **123**, 60-76 (1998).
34. C. R. Gerfen, W. S. Young, Distribution of striatonigral and striatopallidal peptidergic neurons in both patch and matrix compartments: an in situ hybridization histochemistry and fluorescent retrograde tracing study. *Brain research* **460**, 161-167 (1988).
35. O. Aizman, H. Brismar, P. Uhlén, E. Zettergren, A. I. Levey, H. Forssberg, P. Greengard, A. Aperia, Anatomical and physiological evidence for D1 and D2 dopamine receptor colocalization in neostriatal neurons. *Nature neuroscience* **3**, 226-230 (2000).
36. A. V. Kravitz, B. S. Freeze, P. R. Parker, K. Kay, M. T. Thwin, K. Deisseroth, A. C. Kreitzer, Regulation of parkinsonian motor behaviours by optogenetic control of basal ganglia circuitry. *Nature* **466**, 622-626 (2010); published online EpubJul 29 (10.1038/nature09159).
37. C. R. Gerfen, D. J. Surmeier, Modulation of striatal projection systems by dopamine. *Annual review of neuroscience* **34**, 441-466 (2011)10.1146/annurev-neuro-061010-113641).
38. R. L. Albin, A. B. Young, J. B. Penney, The functional anatomy of basal ganglia disorders. *Trends in neurosciences* **12**, 366-375 (1989).

39. B. S. Freeze, A. V. Kravitz, N. Hammack, J. D. Berke, A. C. Kreitzer, Control of Basal Ganglia output by direct and indirect pathway projection neurons. *The Journal of neuroscience : the official journal of the Society for Neuroscience* **33**, 18531-18539 (2013); published online EpubNov 20 (10.1523/JNEUROSCI.1278-13.2013).
40. O. Hikosaka, GABAergic output of the basal ganglia. *Progress in brain research* **160**, 209-226 (2007)10.1016/s0079-6123(06)60012-5).
41. P. Robledo, J. Féger, Excitatory influence of rat subthalamic nucleus to substantia nigra pars reticulata and the pallidal complex: electrophysiological data. *Brain research* **518**, 47-54 (1990).
42. G. Cui, S. B. Jun, X. Jin, M. D. Pham, S. S. Vogel, D. M. Lovinger, R. M. Costa, Concurrent activation of striatal direct and indirect pathways during action initiation. *Nature* **494**, 238-242 (2013); published online EpubFeb 14 (10.1038/nature11846).
43. M. Levesque, A. Parent, The striatofugal fiber system in primates: a reevaluation of its organization based on single-axon tracing studies. *Proceedings of the National Academy of Sciences of the United States of America* **102**, 11888-11893 (2005); published online EpubAug 16 (10.1073/pnas.0502710102).
44. Y. M. Kupchik, R. M. Brown, J. A. Heinsbroek, M. K. Lobo, D. J. Schwartz, P. W. Kalivas, Coding the direct/indirect pathways by D1 and D2 receptors is not valid for accumbens projections. *Nature neuroscience*, (2015); published online EpubJul 27 (10.1038/nn.4068).
45. C. R. Gerfen, The neostriatal mosaic: multiple levels of compartmental organization. *Trends in neurosciences* **15**, 133-139 (1992).
46. S. B. Floresco, The nucleus accumbens: an interface between cognition, emotion, and action. *Annual review of psychology* **66**, 25-52 (2015); published online EpubJan 3 (10.1146/annurev-psych-010213-115159).
47. G. E. Alexander, M. R. DeLong, P. L. Strick, Parallel organization of functionally segregated circuits linking basal ganglia and cortex. *Annual review of neuroscience* **9**, 357-381 (1986).

48. D. Joel, I. Weiner, The connections of the dopaminergic system with the striatum in rats and primates: an analysis with respect to the functional and compartmental organization of the striatum. *Neuroscience* **96**, 451-474 (2000).
49. C. R. Gerfen, The neostriatal mosaic: compartmentalization of corticostriatal input and striatonigral output systems. (1984).
50. A. Friedman, D. Homma, L. G. Gibb, K. Amemori, S. J. Rubin, A. S. Hood, M. H. Riad, A. M. Graybiel, A Corticostriatal Path Targeting Striosomes Controls Decision-Making under Conflict. *Cell* **161**, 1320-1333 (2015); published online EpubJun 4 (10.1016/j.cell.2015.04.049).
51. A. H. Gittis, A. B. Nelson, M. T. Thwin, J. J. Palop, A. C. Kreitzer, Distinct roles of GABAergic interneurons in the regulation of striatal output pathways. *The Journal of neuroscience : the official journal of the Society for Neuroscience* **30**, 2223-2234 (2010); published online EpubFeb 10 (10.1523/JNEUROSCI.4870-09.2010).
52. I. B. Witten, S. C. Lin, M. Brodsky, R. Prakash, I. Diester, P. Anikeeva, V. Gradinaru, C. Ramakrishnan, K. Deisseroth, Cholinergic interneurons control local circuit activity and cocaine conditioning. *Science* **330**, 1677-1681 (2010); published online EpubDec 17 (10.1126/science.1193771).
53. S. J. Cragg, Meaningful silences: how dopamine listens to the ACh pause. *Trends in neurosciences* **29**, 125-131 (2006); published online EpubMar (10.1016/j.tins.2006.01.003).
54. M. Xu, A. Kobets, J. C. Du, J. Lenington, L. Li, M. Banasr, R. S. Duman, F. M. Vaccarino, R. J. DiLeone, C. Pittenger, Targeted ablation of cholinergic interneurons in the dorsolateral striatum produces behavioral manifestations of Tourette syndrome. *Proceedings of the National Academy of Sciences of the United States of America* **112**, 893-898 (2015); published online EpubJan 20 (10.1073/pnas.1419533112).
55. H. Inokawa, H. Yamada, N. Matsumoto, M. Muranishi, M. Kimura, Juxtacellular labeling of tonically active neurons and phasically active neurons in the rat striatum. *Neuroscience* **168**, 395-404 (2010); published online EpubJun 30 (10.1016/j.neuroscience.2010.03.062).
56. Alexandra B. Nelson, N. Hammack, Cindy F. Yang, Nirao M. Shah, Rebecca P. Seal, Anatol C. Kreitzer, Striatal Cholinergic Interneurons Drive GABA Release from Dopamine Terminals. *Neuron*, (2014)10.1016/j.neuron.2014.01.023).

57. S. Threlfell, T. Lalic, N. J. Platt, K. A. Jennings, K. Deisseroth, S. J. Cragg, Striatal dopamine release is triggered by synchronized activity in cholinergic interneurons. *Neuron* **75**, 58-64 (2012); published online EpubJul 12 (10.1016/j.neuron.2012.04.038).
58. A. H. Gittis, G. B. Hang, E. S. LaDow, L. R. Shoenfeld, B. V. Atallah, S. Finkbeiner, A. C. Kreitzer, Rapid target-specific remodeling of fast-spiking inhibitory circuits after loss of dopamine. *Neuron* **71**, 858-868 (2011); published online EpubSep 8 (10.1016/j.neuron.2011.06.035).
59. T. Koos, J. M. Tepper, C. J. Wilson, Comparison of IPSCs evoked by spiny and fast-spiking neurons in the neostriatum. *The Journal of neuroscience : the official journal of the Society for Neuroscience* **24**, 7916-7922 (2004); published online EpubSep 8 (10.1523/JNEUROSCI.2163-04.2004).
60. U. Czubayko, D. Plenz, Fast synaptic transmission between striatal spiny projection neurons. *Proceedings of the National Academy of Sciences of the United States of America* **99**, 15764-15769 (2002); published online EpubNov 26 (10.1073/pnas.242428599).
61. S. Taverna, Y. C. Van Dongen, H. J. Groenewegen, C. M. Pennartz, Direct physiological evidence for synaptic connectivity between medium-sized spiny neurons in rat nucleus accumbens in situ. *Journal of neurophysiology* **91**, 1111-1121 (2004).
62. S. Taverna, B. Canciani, C. M. Pennartz, Dopamine D1-receptors modulate lateral inhibition between principal cells of the nucleus accumbens. *Journal of neurophysiology* **93**, 1816-1819 (2005).
63. M. J. Tunstall, D. E. Oorschot, A. Kean, J. R. Wickens, Inhibitory interactions between spiny projection neurons in the rat striatum. *Journal of neurophysiology* **88**, 1263-1269 (2002).
64. C. J. Wilson, Active decorrelation in the basal ganglia. *Neuroscience* **250C**, 467-482 (2013); published online EpubJul 24 (10.1016/j.neuroscience.2013.07.032).
65. D. Jaeger, H. Kita, C. J. Wilson, Surround inhibition among projection neurons is weak or nonexistent in the rat neostriatum. *Journal of neurophysiology* **72**, 2555-2558 (1994).
66. T. J. Ellender, I. Huerta-Ocampo, K. Deisseroth, M. Capogna, J. P. Bolam, Differential modulation of excitatory and inhibitory striatal synaptic transmission by histamine. *The*

Journal of neuroscience : the official journal of the Society for Neuroscience **31**, 15340-15351 (2011); published online EpubOct 26 (10.1523/JNEUROSCI.3144-11.2011).

67. S. Taverna, E. Ilijic, D. J. Surmeier, Recurrent collateral connections of striatal medium spiny neurons are disrupted in models of Parkinson's disease. *The Journal of neuroscience : the official journal of the Society for Neuroscience* **28**, 5504-5512 (2008); published online EpubMay 21 (10.1523/JNEUROSCI.5493-07.2008).
68. J. T. McKenna, C. Yang, S. Franciosi, S. Winston, K. K. Abarr, M. S. Rigby, Y. Yanagawa, R. W. McCarley, R. E. Brown, Distribution and intrinsic membrane properties of basal forebrain GABAergic and parvalbumin neurons in the mouse. *The Journal of comparative neurology* **521**, 1225-1250 (2013); published online EpubApr 15 (10.1002/cne.23290).
69. D. J. Hegeman, E. S. Hong, V. M. Hernandez, C. S. Chan, The External Globus Pallidus: Progress and Perspectives. *The European journal of neuroscience*, (2016); published online EpubFeb 3 (10.1111/ejn.13196).
70. A. Abdi, N. Mallet, F. Y. Mohamed, A. Sharott, P. D. Dodson, K. C. Nakamura, S. Suri, S. V. Avery, J. T. Larvin, F. N. Garas, S. N. Garas, F. Vinciati, S. Morin, E. Bezard, J. Baufreton, P. J. Magill, Prototypic and arkypallidal neurons in the dopamine-intact external globus pallidus. *The Journal of neuroscience : the official journal of the Society for Neuroscience* **35**, 6667-6688 (2015); published online EpubApr 29 (10.1523/JNEUROSCI.4662-14.2015).
71. M. DeLong, Activity of pallidal neurons during movement. *Journal of neurophysiology* **34**, 414-427 (1971).
72. N. Mallet, B. R. Micklem, P. Henny, M. T. Brown, C. Williams, J. P. Bolam, K. C. Nakamura, P. J. Magill, Dichotomous organization of the external globus pallidus. *Neuron* **74**, 1075-1086 (2012); published online EpubJun 21 (10.1016/j.neuron.2012.04.027).
73. P. D. Dodson, J. T. Larvin, J. M. Duffell, F. N. Garas, N. M. Doig, N. Kessar, I. C. Duguid, R. Bogacz, S. J. Butt, P. J. Magill, Distinct developmental origins manifest in the specialized encoding of movement by adult neurons of the external globus pallidus. *Neuron* **86**, 501-513 (2015); published online EpubApr 22 (10.1016/j.neuron.2015.03.007).
74. K. J. Mastro, R. S. Bouchard, H. A. Holt, A. H. Gittis, Transgenic Mouse Lines Subdivide External Segment of the Globus Pallidus (GPe) Neurons and Reveal Distinct GPe Output Pathways. *The Journal of neuroscience : the official journal of the Society for Neuroscience*

- 34**, 2087-2099 (2014); published online EpubFeb 5 (10.1523/JNEUROSCI.4646-13.2014).
75. K. E. Glajch, D. A. Kelter, D. J. Hegeman, Q. Cui, H. S. Xenias, E. C. Augustine, V. M. Hernandez, N. Verma, T. Y. Huang, M. Luo, N. J. Justice, C. S. Chan, Npas1+ Pallidal Neurons Target Striatal Projection Neurons. *The Journal of neuroscience : the official journal of the Society for Neuroscience* **36**, 5472-5488 (2016); published online EpubMay 18 (10.1523/JNEUROSCI.1720-15.2016).
 76. A. Saunders, I. A. Oldenburg, V. K. Berezovskii, C. A. Johnson, N. D. Kingery, H. L. Elliott, T. Xie, C. R. Gerfen, B. L. Sabatini, A direct GABAergic output from the basal ganglia to frontal cortex. *Nature* **521**, 85-89 (2015); published online EpubMay 7 (10.1038/nature14179).
 77. M. C. Chen, L. Ferrari, M. D. Sacchet, L. C. Foland-Ross, M. H. Qiu, I. H. Gotlib, P. M. Fuller, E. Arrigoni, J. Lu, Identification of a direct GABAergic pallidocortical pathway in rodents. *The European journal of neuroscience* **41**, 748-759 (2015); published online EpubMar (10.1111/ejn.12822).
 78. J. Baufreton, E. Kirkham, J. F. Atherton, A. Menard, P. J. Magill, J. P. Bolam, M. D. Bevan, Sparse but selective and potent synaptic transmission from the globus pallidus to the subthalamic nucleus. *Journal of neurophysiology* **102**, 532-545 (2009); published online EpubJul (10.1152/jn.00305.2009).
 79. D. Joel, I. Weiner, The connections of the primate subthalamic nucleus: indirect pathways and the open-interconnected scheme of basal ganglia-thalamocortical circuitry. *Brain research reviews* **23**, 62-78 (1997).
 80. F. Sato, M. Parent, M. Levesque, A. Parent, Axonal branching pattern of neurons of the subthalamic nucleus in primates. *Journal of Comparative Neurology* **424**, 142-152 (2000).
 81. T. Wichmann, H. Bergman, M. DeLong, The primate subthalamic nucleus. I. Functional properties in intact animals. *Journal of neurophysiology* **72**, 494-506 (1994).
 82. A. Mathai, T. Wichmann, Y. Smith, More than meets the Eye-Myelinated axons crowd the subthalamic nucleus. *Movement disorders : official journal of the Movement Disorder Society*, (2013); published online EpubJul 12 (10.1002/mds.25603).

83. C. J. Wilson, M. D. Bevan, Intrinsic dynamics and synaptic inputs control the activity patterns of subthalamic nucleus neurons in health and in Parkinson's disease. *Neuroscience* **198**, 54-68 (2011); published online EpubDec 15 (10.1016/j.neuroscience.2011.06.049).
84. D. Plenz, S. T. Kital, A basal ganglia pacemaker formed by the subthalamic nucleus and external globus pallidus. *Nature* **400**, 677-682 (1999).
85. M. D. Bevan, P. J. Magill, D. Terman, J. P. Bolam, C. J. Wilson, Move to the rhythm: oscillations in the subthalamic nucleus–external globus pallidus network. *Trends in neurosciences* **25**, 525-531 (2002).
86. S. N. Haber, The place of dopamine in the cortico-basal ganglia circuit. *Neuroscience* **282C**, 248-257 (2014); published online EpubOct 19 (10.1016/j.neuroscience.2014.10.008).
87. H. W. Berendse, H. J. Groenewegen, A. Lohman, Compartmental distribution of ventral striatal neurons projecting to the mesencephalon in the rat. *The Journal of neuroscience* **12**, 2079-2103 (1992).
88. K. S. Rommelfanger, T. Wichmann, Extrastriatal dopaminergic circuits of the Basal Ganglia. *Frontiers in neuroanatomy* **4**, 139 (2010)10.3389/fnana.2010.00139).
89. A. Benazzouz, O. Mamad, P. Abedi, R. Bouali-Benazzouz, J. Chetrit, Involvement of dopamine loss in extrastriatal basal ganglia nuclei in the pathophysiology of Parkinson's disease. *Frontiers in aging neuroscience* **6**, 87 (2014)10.3389/fnagi.2014.00087).
90. J. Chetrit, A. Taupignon, L. Froux, S. Morin, R. Bouali-Benazzouz, F. Naudet, N. Kadiri, C. E. Gross, B. Bioulac, A. Benazzouz, Inhibiting subthalamic d5 receptor constitutive activity alleviates abnormal electrical activity and reverses motor impairment in a rat model of Parkinson's disease. *The Journal of neuroscience : the official journal of the Society for Neuroscience* **33**, 14840-14849 (2013); published online EpubSep 11 (10.1523/JNEUROSCI.0453-13.2013).
91. A. Galvan, B. Floran, D. Erlij, J. Aceves, Intrapallidal dopamine restores motor deficits induced by 6-hydroxydopamine in the rat. *Journal of neural transmission* **108**, 153-166 (2001).

92. A. Galvan, X. Hu, K. S. Rommelfanger, J.-F. Pare, Z. U. Khan, Y. Smith, T. Wichmann, Localization and function of dopamine receptors in the subthalamic nucleus of normal and parkinsonian monkeys. *Journal of neurophysiology* **112**, 467-479 (2014).
93. J. Baufreton, Z. T. Zhu, M. Garret, B. Bioulac, S. W. Johnson, A. I. Taupignon, Dopamine receptors set the pattern of activity generated in subthalamic neurons. *FASEB journal : official publication of the Federation of American Societies for Experimental Biology* **19**, 1771-1777 (2005); published online EpubNov (10.1096/fj.04-3401hyp).
94. D. J. Surmeier, L. Carrillo-Reid, J. Bargas, Dopaminergic modulation of striatal neurons, circuits, and assemblies. *Neuroscience* **198**, 3-18 (2011); published online EpubDec 15 (10.1016/j.neuroscience.2011.08.051).
95. N. X. Tritsch, B. L. Sabatini, Dopaminergic modulation of synaptic transmission in cortex and striatum. *Neuron* **76**, 33-50 (2012); published online EpubOct 4 (10.1016/j.neuron.2012.09.023).
96. N. S. Bamford, H. Zhang, Y. Schmitz, N.-P. Wu, C. Cepeda, M. S. Levine, C. Schmauss, S. S. Zakharenko, L. Zablow, D. Sulzer, Heterosynaptic dopamine neurotransmission selects sets of corticostriatal terminals. *Neuron* **42**, 653-663 (2004).
97. C. L. Zold, F. Kasanetz, P. E. Pomata, M. A. Belluscio, M. V. Escande, G. L. Galinanes, L. A. Riquelme, M. G. Murer, Striatal gating through up states and oscillations in the basal ganglia: Implications for Parkinson's disease. *Journal of physiology, Paris* **106**, 40-46 (2012); published online EpubJan (10.1016/j.jphysparis.2011.06.002).
98. C. J. Wilson, Y. Kawaguchi, The origins of two-state spontaneous membrane potential fluctuations of neostriatal spiny neurons. *The Journal of neuroscience* **16**, 2397-2410 (1996).
99. K. Y. Tseng, F. Kasanetz, L. Kargieman, L. A. Riquelme, M. G. Murer, Cortical slow oscillatory activity is reflected in the membrane potential and spike trains of striatal neurons in rats with chronic nigrostriatal lesions. *The Journal of Neuroscience* **21**, 6430-6439 (2001).
100. T. N. Lerner, A. C. Kreitzer, Neuromodulatory control of striatal plasticity and behavior. *Current opinion in neurobiology* **21**, 322-327 (2011); published online EpubApr (10.1016/j.conb.2011.01.005).

101. A. C. Kreitzer, R. C. Malenka, Dopamine modulation of state-dependent endocannabinoid release and long-term depression in the striatum. *The Journal of neuroscience : the official journal of the Society for Neuroscience* **25**, 10537-10545 (2005); published online EpubNov 9 (10.1523/JNEUROSCI.2959-05.2005).
102. R. Van Zessen, J. L. Phillips, E. A. Budygin, G. D. Stuber, Activation of VTA GABA neurons disrupts reward consumption. *Neuron* **73**, 1184-1194 (2012).
103. D. B. Carr, S. R. Sesack, GABA - containing neurons in the rat ventral tegmental area project to the prefrontal cortex. *Synapse* **38**, 114-123 (2000).
104. M. T. Brown, K. R. Tan, E. C. O'Connor, I. Nikonenko, D. Muller, C. Luscher, Ventral tegmental area GABA projections pause accumbal cholinergic interneurons to enhance associative learning. *Nature* **492**, 452-456 (2012); published online EpubDec 20 (10.1038/nature11657).
105. C. E. Vaaga, M. Borisovska, G. L. Westbrook, Dual-transmitter neurons: functional implications of co-release and co-transmission. *Current opinion in neurobiology* **29C**, 25-32 (2014); published online EpubMay 7 (10.1016/j.conb.2014.04.010).
106. N. X. Tritsch, J. B. Ding, B. L. Sabatini, Dopaminergic neurons inhibit striatal output through non-canonical release of GABA. *Nature* **490**, 262-266 (2012); published online EpubOct 11 (10.1038/nature11466).
107. J. Berrios, A. M. Stamatakis, P. A. Kantak, Z. A. McElligott, M. C. Judson, M. Aita, M. Rougie, G. D. Stuber, B. D. Philpot, Loss of UBE3A from TH-expressing neurons suppresses GABA co-release and enhances VTA-NAc optical self-stimulation. *Nature communications* **7**, 10702 (2016)10.1038/ncomms10702).
108. P. Hoerbelt, T. A. Lindsley, M. W. Fleck, Dopamine Directly Modulates GABAA Receptors. *The Journal of neuroscience : the official journal of the Society for Neuroscience* **35**, 3525-3536 (2015); published online EpubFeb 25 (10.1523/JNEUROSCI.4390-14.2015).
109. G. D. Stuber, T. S. Hnasko, J. P. Britt, R. H. Edwards, A. Bonci, Dopaminergic terminals in the nucleus accumbens but not the dorsal striatum corelease glutamate. *The Journal of neuroscience : the official journal of the Society for Neuroscience* **30**, 8229-8233 (2010); published online EpubJun 16 (10.1523/JNEUROSCI.1754-10.2010).

110. M. Antal, B. M. Beneduce, W. G. Regehr, The substantia nigra conveys target-dependent excitatory and inhibitory outputs from the Basal Ganglia to the thalamus. *The Journal of neuroscience : the official journal of the Society for Neuroscience* **34**, 8032-8042 (2014); published online EpubJun 4 (10.1523/JNEUROSCI.0236-14.2014).
111. J. Tepper, L. Martin, D. Anderson, GABAA receptor-mediated inhibition of rat substantia nigra dopaminergic neurons by pars reticulata projection neurons. *The Journal of Neuroscience* **15**, 3092-3103 (1995).
112. P. Mailly, S. Charpier, S. Mahon, A. Menetrey, A. Thierry, J. Glowinski, J. Deniau, Dendritic arborizations of the rat substantia nigra pars reticulata neurons: spatial organization and relation to the lamellar compartmentation of striato-nigral projections. *The Journal of Neuroscience* **21**, 6874-6888 (2001).
113. C. R. Gerfen, The neostriatal mosaic. I. Compartmental organization of projections from the striatum to the substantia nigra in the rat. *Journal of Comparative Neurology* **236**, 454-476 (1985).
114. F. M. Zhou, C. R. Lee, Intrinsic and integrative properties of substantia nigra pars reticulata neurons. *Neuroscience* **198**, 69-94 (2011); published online EpubDec 15 (10.1016/j.neuroscience.2011.07.061).
115. J. H. Goldberg, M. A. Farries, M. S. Fee, Basal ganglia output to the thalamus: still a paradox. *Trends in neurosciences* **36**, 695-705 (2013); published online EpubNov 1 (10.1016/j.tins.2013.09.001).
116. P. Calabresi, B. Picconi, A. Tozzi, V. Ghiglieri, M. Di Filippo, Direct and indirect pathways of basal ganglia: a critical reappraisal. *Nature neuroscience* **17**, 1022-1030 (2014); published online EpubAug (10.1038/nn.3743).
117. A. Nambu, Seven problems on the basal ganglia. *Current opinion in neurobiology* **18**, 595-604 (2008); published online EpubDec (10.1016/j.conb.2008.11.001).
118. S. G. Kim, S. Ogawa, Biophysical and physiological origins of blood oxygenation level-dependent fMRI signals. *Journal of cerebral blood flow and metabolism : official journal of the International Society of Cerebral Blood Flow and Metabolism* **32**, 1188-1206 (2012); published online EpubJul (10.1038/jcbfm.2012.23).

119. N. K. Logothetis, What we can do and what we cannot do with fMRI. *Nature* **453**, 869-878 (2008); published online EpubJun 12 (10.1038/nature06976).
120. B. B. Biswal, Resting state fMRI: a personal history. *NeuroImage* **62**, 938-944 (2012); published online EpubAug 15 (10.1016/j.neuroimage.2012.01.090).
121. Jonathan D. Power, Bradley L. Schlaggar, Steven E. Petersen, Studying Brain Organization via Spontaneous fMRI Signal. *Neuron* **84**, 681-696 (2014)10.1016/j.neuron.2014.09.007).
122. C. P. Pawela, B. B. Biswal, Y. R. Cho, D. S. Kao, R. Li, S. R. Jones, M. L. Schulte, H. S. Matloub, A. G. Hudetz, J. S. Hyde, Resting-state functional connectivity of the rat brain. *Magnetic resonance in medicine : official journal of the Society of Magnetic Resonance in Medicine / Society of Magnetic Resonance in Medicine* **59**, 1021-1029 (2008); published online EpubMay (10.1002/mrm.21524).
123. A. Viswanathan, R. D. Freeman, Neurometabolic coupling in cerebral cortex reflects synaptic more than spiking activity. *Nature neuroscience* **10**, 1308-1312 (2007); published online EpubOct (10.1038/nn1977).
124. C. C. Yen, M. Fukuda, S. G. Kim, BOLD responses to different temporal frequency stimuli in the lateral geniculate nucleus and visual cortex: insights into the neural basis of fMRI. *NeuroImage* **58**, 82-90 (2011); published online EpubSep 1 (10.1016/j.neuroimage.2011.06.022).
125. J. B. Goense, N. K. Logothetis, Neurophysiology of the BOLD fMRI signal in awake monkeys. *Current biology : CB* **18**, 631-640 (2008); published online EpubMay 6 (10.1016/j.cub.2008.03.054).
126. A. Rauch, G. Rainer, N. K. Logothetis, The effect of a serotonin-induced dissociation between spiking and perisynaptic activity on BOLD functional MRI. *Proceedings of the National Academy of Sciences of the United States of America* **105**, 6759-6764 (2008); published online EpubMay 6 (10.1073/pnas.0800312105).
127. G. T. Einevoll, C. Kayser, N. K. Logothetis, S. Panzeri, Modelling and analysis of local field potentials for studying the function of cortical circuits. *Nature reviews. Neuroscience* **14**, 770-785 (2013); published online EpubOct 18 (10.1038/nrn3599).

128. N. K. Logothetis, J. Pauls, M. Augath, T. Trinath, A. Oeltermann, Neurophysiological investigation of the basis of the fMRI signal. *Nature* **412**, 150-157 (2001).
129. M. L. Scholvinck, D. A. Leopold, M. J. Brookes, P. H. Khader, The contribution of electrophysiology to functional connectivity mapping. *NeuroImage* **80**, 297-306 (2013); published online EpubOct 15 (10.1016/j.neuroimage.2013.04.010).
130. M. L. Schölvinck, A. Maier, Q. Y. Frank, J. H. Duyn, D. A. Leopold, Neural basis of global resting-state fMRI activity. *Proceedings of the National Academy of Sciences* **107**, 10238-10243 (2010).
131. E. A. Ferenczi, K. A. Zalocusky, C. Liston, L. Grosenick, M. R. Warden, D. Amatyia, K. Katovich, H. Mehta, B. Patenaude, C. Ramakrishnan, P. Kalanithi, A. Etkin, B. Knutson, G. H. Glover, K. Deisseroth, Prefrontal cortical regulation of brainwide circuit dynamics and reward-related behavior. *Science* **351**, aac9698 (2016); published online EpubJan 1 (10.1126/science.aac9698).
132. H. Y. Lai, D. L. Albaugh, Y. C. Kao, J. R. Younce, Y. Y. Shih, Robust deep brain stimulation functional MRI procedures in rats and mice using an MR - compatible tungsten microwire electrode. *Magnetic resonance in medicine : official journal of the Society of Magnetic Resonance in Medicine / Society of Magnetic Resonance in Medicine* **73**, 1246-1251 (2015).
133. J. R. Younce, D. L. Albaugh, Y. Y. Shih, Deep Brain Stimulation with Simultaneous fMRI in Rodents. *Journal of visualized experiments : JoVE*, e51271-e51271 (2014).
134. W. M. Grill, M. B. Cantrell, M. S. Robertson, Antidromic propagation of action potentials in branched axons: implications for the mechanisms of action of deep brain stimulation. *Journal of computational neuroscience* **24**, 81-93 (2008); published online EpubFeb (10.1007/s10827-007-0043-9).
135. T. Wichmann, M. R. DeLong, Deep-Brain Stimulation for Basal Ganglia Disorders. *Basal ganglia* **1**, 65-77 (2011); published online EpubJul 1 (10.1016/j.baga.2011.05.001).
136. A. L. Benabid, P. Pollak, D. Hoffmann, C. Gervason, M. Hommel, J. Perret, J. De Rougemont, D. Gao, Long-term suppression of tremor by chronic stimulation of the ventral intermediate thalamic nucleus. *The Lancet* **337**, 403-406 (1991).

137. Andres M. Lozano, N. Lipsman, Probing and Regulating Dysfunctional Circuits Using Deep Brain Stimulation. *Neuron* **77**, 406-424 (2013)10.1016/j.neuron.2013.01.020).
138. A. D. Dorval, A. M. Kuncel, M. J. Birdno, D. A. Turner, W. M. Grill, Deep brain stimulation alleviates parkinsonian bradykinesia by regularizing pallidal activity. *Journal of neurophysiology* **104**, 911-921 (2010); published online EpubAug (10.1152/jn.00103.2010).
139. E. Moro, A. M. Lozano, P. Pollak, Y. Agid, S. Rehncrona, J. Volkmann, J. Kulisevsky, J. A. Obeso, A. Albanese, M. I. Hariz, N. P. Quinn, J. D. Speelman, A. L. Benabid, V. Fraix, A. Mendes, M. L. Welter, J. L. Houeto, P. Cornu, D. Dormont, A. L. Tornqvist, R. Ekberg, A. Schnitzler, L. Timmermann, L. Wojtecki, A. Gironell, M. C. Rodriguez-Oroz, J. Guridi, A. R. Bentivoglio, M. F. Contarino, L. Romito, M. Scerrati, M. Janssens, A. E. Lang, Long-term results of a multicenter study on subthalamic and pallidal stimulation in Parkinson's disease. *Movement disorders : official journal of the Movement Disorder Society* **25**, 578-586 (2010); published online EpubApr 15 (10.1002/mds.22735).
140. H. Y. Lai, J. R. Younce, D. L. Albaugh, Y. C. Kao, Y. Y. Shih, Functional MRI reveals frequency-dependent responses during deep brain stimulation at the subthalamic nucleus or internal globus pallidus. *NeuroImage* **84**, 11-18 (2014)10.1016/j.neuroimage.2013.08.026).
141. H. K. Min, S. C. Hwang, M. P. Marsh, I. Kim, E. Knight, B. Strierner, J. P. Felmlee, K. M. Welker, C. D. Blaha, S. Y. Chang, K. E. Bennet, K. H. Lee, Deep brain stimulation induces BOLD activation in motor and non-motor networks: an fMRI comparison study of STN and EN/GPi DBS in large animals. *NeuroImage* **63**, 1408-1420 (2012); published online EpubNov 15 (10.1016/j.neuroimage.2012.08.006).
142. C. K. Young, A. R. Brown, J. H. Robinson, U. I. Tuor, J. F. Dunn, B. H. Bland, G. C. Teskey, Functional MRI response and correlated electrophysiological changes during posterior hypothalamic nucleus deep brain stimulation. *NeuroImage* **56**, 35-44 (2011); published online EpubMay 1 (10.1016/j.neuroimage.2011.02.023).
143. E. S. Boyden, F. Zhang, E. Bamberg, G. Nagel, K. Deisseroth, Millisecond-timescale, genetically targeted optical control of neural activity. *Nature neuroscience* **8**, 1263-1268 (2005); published online EpubSep (10.1038/nn1525).
144. O. Yizhar, L. E. Fenno, T. J. Davidson, M. Mogri, K. Deisseroth, Optogenetics in neural systems. *Neuron* **71**, 9-34 (2011); published online EpubJul 14 (10.1016/j.neuron.2011.06.004).

145. F. Zhang, J. Vierock, O. Yizhar, L. E. Fenno, S. Tsunoda, A. Kianianmomeni, M. Prigge, A. Berndt, J. Cushman, J. Polle, J. Magnuson, P. Hegemann, K. Deisseroth, The microbial opsin family of optogenetic tools. *Cell* **147**, 1446-1457 (2011); published online EpubDec 23 (10.1016/j.cell.2011.12.004).
146. J. H. Lee, R. Durand, V. Gradinaru, F. Zhang, I. Goshen, D. S. Kim, L. E. Fenno, C. Ramakrishnan, K. Deisseroth, Global and local fMRI signals driven by neurons defined optogenetically by type and wiring. *Nature* **465**, 788-792 (2010); published online EpubJun 10 (10.1038/nature09108).
147. T. Wichmann, M. R. DeLong, Deep brain stimulation for neurologic and neuropsychiatric disorders. *Neuron* **52**, 197-204 (2006); published online EpubOct 5 (10.1016/j.neuron.2006.09.022).
148. W. K. Goodman, R. L. Alterman, Deep brain stimulation for intractable psychiatric disorders. *Annual review of medicine* **63**, 511-524 (2012)10.1146/annurev-med-052209-100401).
149. P. P. de Koning, M. Figee, P. van den Munckhof, P. R. Schuurman, D. Denys, Current status of deep brain stimulation for obsessive-compulsive disorder: a clinical review of different targets. *Current psychiatry reports* **13**, 274-282 (2011); published online EpubAug (10.1007/s11920-011-0200-8).
150. B. H. Bewernick, S. Kayser, V. Sturm, T. E. Schlaepfer, Long-term effects of nucleus accumbens deep brain stimulation in treatment-resistant depression: evidence for sustained efficacy. *Neuropsychopharmacology : official publication of the American College of Neuropsychopharmacology* **37**, 1975-1985 (2012); published online EpubAug (10.1038/npp.2012.44).
151. L. Garcia, G. D'Alessandro, B. Bioulac, C. Hammond, High-frequency stimulation in Parkinson's disease: more or less? *Trends in neurosciences* **28**, 209-216 (2005); published online EpubApr (10.1016/j.tins.2005.02.005).
152. D. L. Albaugh, Y. Y. Shih, Neural circuit modulation during deep brain stimulation at the subthalamic nucleus for Parkinson's disease: what have we learned from neuroimaging studies? *Brain connectivity* **4**, 1-14 (2014); published online EpubFeb (10.1089/brain.2013.0193).
153. R. Jech, in *Deep Brain Stimulation in Neurological and Psychiatric Disorders*. (Springer, 2008), pp. 179-201.

154. M. Tagliati, J. Jankovic, F. Pagan, F. Susatia, I. U. Isaias, M. S. Okun, D. B. S. W. G. National Parkinson Foundation, Safety of MRI in patients with implanted deep brain stimulation devices. *NeuroImage* **47 Suppl 2**, T53-57 (2009); published online EpubAug (10.1016/j.neuroimage.2009.04.044).
155. E. J. Knight, H. K. Min, S. C. Hwang, M. P. Marsh, S. Paek, I. Kim, J. P. Felmlee, O. A. Abulseoud, K. E. Bennet, M. A. Frye, K. H. Lee, Nucleus accumbens deep brain stimulation results in insula and prefrontal activation: a large animal fMRI study. *PloS one* **8**, e56640 (2013)10.1371/journal.pone.0056640).
156. S. G. Ewing, A. A. Grace, Long-term high frequency deep brain stimulation of the nucleus accumbens drives time-dependent changes in functional connectivity in the rodent limbic system. *Brain Stimul* **6**, 274-285 (2013); published online EpubMay (10.1016/j.brs.2012.07.007).
157. C. Hamani, B. O. Amorim, A. L. Wheeler, M. Diwan, K. Driesslein, L. Covolan, C. R. Butson, J. N. Nobrega, Deep brain stimulation in rats: different targets induce similar antidepressant-like effects but influence different circuits. *Neurobiology of disease* **71**, 205-214 (2014); published online EpubNov (10.1016/j.nbd.2014.08.007).
158. J. Hamilton, J. Lee, J. J. Canales, Chronic Unilateral Stimulation of the Nucleus Accumbens at High or Low Frequencies Attenuates Relapse to Cocaine Seeking in an Animal Model. *Brain Stimul* **8**, 57-63 (2015); published online EpubOct 5 (10.1016/j.brs.2014.09.018).
159. C. B. McCracken, A. A. Grace, High-frequency deep brain stimulation of the nucleus accumbens region suppresses neuronal activity and selectively modulates afferent drive in rat orbitofrontal cortex in vivo. *The Journal of neuroscience : the official journal of the Society for Neuroscience* **27**, 12601-12610 (2007); published online EpubNov 14 (10.1523/JNEUROSCI.3750-07.2007).
160. F. M. Vassoler, H. D. Schmidt, M. E. Gerard, K. R. Famous, D. A. Ciraulo, C. Kornetsky, C. M. Knapp, R. C. Pierce, Deep brain stimulation of the nucleus accumbens shell attenuates cocaine priming-induced reinstatement of drug seeking in rats. *The Journal of neuroscience : the official journal of the Society for Neuroscience* **28**, 8735-8739 (2008); published online EpubAug 27 (10.1523/JNEUROSCI.5277-07.2008).
161. Y. Xie, T. Heida, J. Stegenga, Y. Zhao, A. Moser, V. Tronnier, T. J. Feuerstein, U. G. Hofmann, High-frequency electrical stimulation suppresses cholinergic accumbens interneurons in acute rat brain slices through GABA receptors. *The European journal of neuroscience* **40**, 3653-3662 (2014); published online EpubSep 23 (10.1111/ejn.12736).

162. D. R. Sparta, A. M. Stamatakis, J. L. Phillips, N. Hovelso, R. van Zessen, G. D. Stuber, Construction of implantable optical fibers for long-term optogenetic manipulation of neural circuits. *Nature protocols* **7**, 12-23 (2012); published online EpubJan (10.1038/nprot.2011.413).
163. B. C. Shyu, C. Y. Lin, J. J. Sun, S. L. Chen, C. Chang, BOLD response to direct thalamic stimulation reveals a functional connection between the medial thalamus and the anterior cingulate cortex in the rat. *Magnetic resonance in medicine : official journal of the Society of Magnetic Resonance in Medicine / Society of Magnetic Resonance in Medicine* **52**, 47-55 (2004); published online EpubJul (10.1002/mrm.20111).
164. T.-H. H. Chao, J.-H. Chen, C.-T. Yen, Repeated BOLD-fMRI imaging of deep brain stimulation responses in rats. *PloS one* **9**, e97305 (2014).
165. Y. Y. Shih, G. Li, E. R. Muir, B. H. De La Garza, J. W. Kiel, T. Q. Duong, Pharmacological MRI of the choroid and retina: blood flow and BOLD responses during nitroprusside infusion. *Magnetic resonance in medicine : official journal of the Society of Magnetic Resonance in Medicine / Society of Magnetic Resonance in Medicine* **68**, 1273-1278 (2012); published online EpubOct (10.1002/mrm.24112).
166. Y. Y. Shih, L. Wang, B. H. De La Garza, G. Li, G. Cull, J. W. Kiel, T. Q. Duong, Quantitative retinal and choroidal blood flow during light, dark adaptation and flicker light stimulation in rats using fluorescent microspheres. *Current eye research* **38**, 292-298 (2013); published online EpubFeb (10.3109/02713683.2012.756526).
167. R. Gruetter, Automatic, localized in Vivo adjustment of all first - and second - order shim coils. *Magnetic Resonance in Medicine* **29**, 804-811 (1993).
168. M. Fukuda, A. L. Vazquez, X. Zong, S. G. Kim, Effects of the alpha(2)-adrenergic receptor agonist dexmedetomidine on neural, vascular and BOLD fMRI responses in the somatosensory cortex. *The European journal of neuroscience* **37**, 80-95 (2013); published online EpubJan (10.1111/ejn.12024).
169. S. G. Kim, N. Harel, T. Jin, T. Kim, P. Lee, F. Zhao, Cerebral blood volume MRI with intravascular superparamagnetic iron oxide nanoparticles. *NMR in biomedicine* **26**, 949-962 (2013); published online EpubAug (10.1002/nbm.2885).
170. S. Canals, M. Beyerlein, Y. Murayama, N. K. Logothetis, Electric stimulation fMRI of the perforant pathway to the rat hippocampus. *Magnetic resonance imaging* **26**, 978-986 (2008); published online EpubSep (10.1016/j.mri.2008.02.018).

171. M. L. Kringelbach, N. Jenkinson, S. L. Owen, T. Z. Aziz, Translational principles of deep brain stimulation. *Nature reviews. Neuroscience* **8**, 623-635 (2007); published online EpubAug (10.1038/nrn2196).
172. H. Decot, W. Gao, J. H. Jennings, P. A. Kantak, Y. C. Kao, M. Das, I. B. Witten, K. Deisseroth, Y. Y. Shih, G. D. Stuber, in *The 23rd Annual Meeting of the International Society for Magnetic Resonance in Medicine*. (Tornoto, Canada, 2015).
173. D. L. Albaugh, G. D. Stuber, Y. Y. Shih, in *The 23rd Annual Meeting of the International Society for Magnetic Resonance in Medicine*. (Toronto, Canada, 2015).
174. P. A. Valdes-Hernandez, A. Sumiyoshi, H. Nonaka, R. Haga, E. Aubert-Vasquez, T. Ogawa, Y. Iturria-Medina, J. J. Riera, R. Kawashima, An in vivo MRI Template Set for Morphometry, Tissue Segmentation, and fMRI Localization in Rats. *Frontiers in neuroinformatics* **5**, 26 (2011)10.3389/fninf.2011.00026).
175. Y. Benjamini, D. Drai, G. Elmer, N. Kafkafi, I. Golani, Controlling the false discovery rate in behavior genetics research. *Behavioural brain research* **125**, 279-284 (2001).
176. G. Paxinos, C. Watson, *The rat brain in stereotaxic coordinates*. (Academic Press, New York, NY, ed. 5th, 2004).
177. J. P. Britt, F. Benaliouad, R. A. McDevitt, G. D. Stuber, R. A. Wise, A. Bonci, Synaptic and behavioral profile of multiple glutamatergic inputs to the nucleus accumbens. *Neuron* **76**, 790-803 (2012); published online EpubNov 21 (10.1016/j.neuron.2012.09.040).
178. S. J. Russo, E. J. Nestler, The brain reward circuitry in mood disorders. *Nature reviews. Neuroscience* **14**, 609-625 (2013); published online EpubSep (10.1038/nrn3381).
179. Y. Xia, J. R. Driscoll, L. Wilbrecht, E. B. Margolis, H. L. Fields, G. O. Hjelmstad, Nucleus accumbens medium spiny neurons target non-dopaminergic neurons in the ventral tegmental area. *The Journal of neuroscience : the official journal of the Society for Neuroscience* **31**, 7811-7816 (2011); published online EpubMay 25 (10.1523/JNEUROSCI.1504-11.2011).
180. M. Figee, J. Luigjes, R. Smolders, C.-E. Valencia-Alfonso, G. van Wingen, B. de Kwaasteniet, M. Mantione, P. Ooms, P. de Koning, N. Vulink, N. Levar, L. Droge, P. van den

- Munckhof, P. R. Schuurman, A. Nederveen, W. van den Brink, A. Mazaheri, M. Vink, D. Denys, Deep brain stimulation restores frontostriatal network activity in obsessive-compulsive disorder. *Nature neuroscience* **16**, 386-387 (2013)10.1038/nn.3344).
181. F. A. Nasrallah, H. C. Tay, K. H. Chuang, Detection of functional connectivity in the resting mouse brain. *NeuroImage* **86**, 417-424 (2014); published online EpubFeb 1 (10.1016/j.neuroimage.2013.10.025).
 182. Y. Y. Shih, T. V. Yash, B. Rogers, T. Q. Duong, fMRI of deep brain stimulation at the rat ventral posteromedial thalamus. *Brain Stimulation* **7**, 190-193 (2014).
 183. T. Scherf, F. Angenstein, Postsynaptic and spiking activity of pyramidal cells, the principal neurons in the rat hippocampal CA1 region, does not control the resultant BOLD response: a combined electrophysiologic and fMRI approach. *Journal of cerebral blood flow and metabolism : official journal of the International Society of Cerebral Blood Flow and Metabolism* **35**, 565-575 (2015); published online EpubApr (10.1038/jcbfm.2014.252).
 184. M. Creed, V. J. Pascoli, C. Lüscher, Refining deep brain stimulation to emulate optogenetic treatment of synaptic pathology. *Science* **347**, 659-664 (2015).
 185. I. N. Christie, J. A. Wells, P. Southern, N. Marina, S. Kasparov, A. V. Gourine, M. F. Lythgoe, fMRI response to blue light delivery in the naive brain: Implications for combined optogenetic fMRI studies. *NeuroImage* **66C**, 634-641 (2012); published online EpubNov 2 (10.1016/j.neuroimage.2012.10.074).
 186. F. Schmid, L. Wachsmuth, F. Albers, M. Schwalm, A. Stroh, C. Faber, True and apparent optogenetic BOLD fMRI signals. *Magnetic resonance in medicine : official journal of the Society of Magnetic Resonance in Medicine / Society of Magnetic Resonance in Medicine*, (2016); published online EpubJan 17 (10.1002/mrm.26095).
 187. C. H. Tai, T. Boraud, E. Bezard, B. Bioulac, C. Gross, A. Benazzouz, Electrophysiological and metabolic evidence that high-frequency stimulation of the subthalamic nucleus bridges neuronal activity in the subthalamic nucleus and the substantia nigra reticulata. *FASEB journal : official publication of the Federation of American Societies for Experimental Biology* **17**, 1820-1830 (2003); published online EpubOct (10.1096/fj.03-0163com).

188. M. Filali, W. D. Hutchison, V. N. Palter, A. M. Lozano, J. O. Dostrovsky, Stimulation-induced inhibition of neuronal firing in human subthalamic nucleus. *Exp Brain Res* **156**, 274-281 (2004).
189. N. K. Logothetis, The ins and outs of fMRI signals. *Nature neuroscience* **10**, 1230-1232 (2007).
190. S. Shehab, C. D'Souza, M. Ljubisavljevic, P. Redgrave, High-frequency electrical stimulation of the subthalamic nucleus excites target structures in a model using c-fos immunohistochemistry. *Neuroscience* **270**, 212-225 (2014); published online EpubJun 13 (10.1016/j.neuroscience.2014.04.016).
191. F. M. Vassoler, S. L. White, T. J. Hopkins, L. A. Guercio, J. Espallergues, O. Berton, H. D. Schmidt, R. C. Pierce, Deep brain stimulation of the nucleus accumbens shell attenuates cocaine reinstatement through local and antidromic activation. *The Journal of neuroscience : the official journal of the Society for Neuroscience* **33**, 14446-14454 (2013); published online EpubSep 4 (10.1523/JNEUROSCI.4804-12.2013).
192. A. Saryyeva, M. Nakamura, J. K. Krauss, K. Schwabe, c-Fos expression after deep brain stimulation of the pedunclopontine tegmental nucleus in the rat 6-hydroxydopamine Parkinson model. *Journal of chemical neuroanatomy* **42**, 210-217 (2011).
193. S. K. Bourne, C. A. Eckhardt, S. A. Sheth, E. N. Eskandar, Mechanisms of deep brain stimulation for obsessive compulsive disorder: effects upon cells and circuits. *Frontiers in integrative neuroscience* **6**, 29 (2012)10.3389/fnint.2012.00029).
194. B. Nuttin, P. Cosyns, H. Demeulemeester, J. Gybels, B. Meyerson, Electrical stimulation in anterior limbs of internal capsules in patients with obsessive-compulsive disorder. *The Lancet* **354**, 1526 (1999)10.1016/s0140-6736(99)02376-4).
195. W. M. Grill, A. N. Snyder, S. Miocinovic, Deep brain stimulation creates an informational lesion of the stimulated nucleus. *Neuroreport* **15**, 1137-1140 (2004).
196. M. Figee, P. de Koning, S. Klaassen, N. Vulink, M. Mantione, P. van den Munckhof, R. Schuurman, G. van Wingen, T. van Amelsvoort, J. Booij, D. Denys, Deep brain stimulation induces striatal dopamine release in obsessive-compulsive disorder. *Biological psychiatry* **75**, 647-652 (2014); published online EpubApr 15 (10.1016/j.biopsych.2013.06.021).

197. B. D. Greenberg, L. A. Gabriels, D. A. Malone, Jr., A. R. Rezai, G. M. Friehs, M. S. Okun, N. A. Shapira, K. D. Foote, P. R. Cosyns, C. S. Kubu, P. F. Malloy, S. P. Salloway, J. E. Giftakis, M. T. Rise, A. G. Machado, K. B. Baker, P. H. Stypulkowski, W. K. Goodman, S. A. Rasmussen, B. J. Nuttin, Deep brain stimulation of the ventral internal capsule/ventral striatum for obsessive-compulsive disorder: worldwide experience. *Molecular psychiatry* **15**, 64-79 (2010); published online EpubJan (10.1038/mp.2008.55).
198. R. C. Pierce, F. M. Vassoler, Deep brain stimulation for the treatment of addiction: basic and clinical studies and potential mechanisms of action. *Psychopharmacology* **229**, 487-491 (2013); published online EpubOct (10.1007/s00213-013-3214-6).
199. A. Mundt, J. Klein, D. Joel, A. Heinz, A. Djodari-Irani, D. Harnack, A. Kupsch, H. Orawa, G. Juckel, R. Morgenstern, C. Winter, High-frequency stimulation of the nucleus accumbens core and shell reduces quinpirole-induced compulsive checking in rats. *The European journal of neuroscience* **29**, 2401-2412 (2009); published online EpubJun (10.1111/j.1460-9568.2009.06777.x).
200. A. van Dijk, M. Klanker, N. van Oorschot, R. Post, R. Hamelink, M. G. Feenstra, D. Denys, Deep brain stimulation affects conditioned and unconditioned anxiety in different brain areas. *Translational psychiatry* **3**, e289 (2013)10.1038/tp.2013.56).
201. H. K. Min, E. K. Ross, K. H. Lee, K. Dennis, S. R. Han, J. H. Jeong, M. P. Marsh, B. Striemer, J. P. Felmlee, J. L. Lujan, S. Goerss, P. S. Duffy, C. D. Blaha, S. Y. Chang, K. E. Bennet, Subthalamic Nucleus Deep Brain Stimulation Induces Motor Network BOLD Activation: Use of a High Precision MRI Guided Stereotactic System for Nonhuman Primates. *Brain Stimul* **7**, 603-607 (2014); published online EpubMay 2 (10.1016/j.brs.2014.04.007).
202. M. R. DeLong, Primate models of movement disorders of basal ganglia origin. *Trends in neurosciences* **13**, 281-285 (1990).
203. A. H. Gittis, J. D. Berke, M. D. Bevan, C. S. Chan, N. Mallet, M. M. Morrow, R. Schmidt, New roles for the external globus pallidus in basal ganglia circuits and behavior. *The Journal of neuroscience : the official journal of the Society for Neuroscience* **34**, 15178-15183 (2014); published online EpubNov 12 (10.1523/JNEUROSCI.3252-14.2014).
204. F. Tecuapetla, S. Matias, G. P. Dugue, Z. F. Mainen, R. M. Costa, Balanced activity in basal ganglia projection pathways is critical for contraversive movements. *Nature communications* **5**, 4315 (2014)10.1038/ncomms5315).

205. D. M. Friend, A. V. Kravitz, Working together: basal ganglia pathways in action selection. *Trends in neurosciences* **37**, 301-303 (2014); published online EpubMay 9 (10.1016/j.tins.2014.04.004).
206. R. Schmidt, D. K. Leventhal, N. Mallet, F. Chen, J. D. Berke, Canceling actions involves a race between basal ganglia pathways. *Nature neuroscience* **16**, 1118-1124 (2013); published online EpubJul 14 (10.1038/nn.3456).
207. J. F. Dunn, U. I. Tuor, J. Kmech, N. A. Young, A. K. Henderson, J. C. Jackson, P. A. Valentine, G. C. Teskey, Functional brain mapping at 9.4T using a new MRI-compatible electrode chronically implanted in rats. *Magnetic resonance in medicine : official journal of the Society of Magnetic Resonance in Medicine / Society of Magnetic Resonance in Medicine* **61**, 222-228 (2009); published online EpubJan (10.1002/mrm.21803).
208. E. K. Ross, J. P. Kim, M. L. Settell, S. R. Han, C. D. Blaha, H. K. Min, K. H. Lee, Fornix deep brain stimulation circuit effect is dependent on major excitatory transmission via the nucleus accumbens. *NeuroImage* **128**, 138-148 (2016); published online EpubJan 11 (10.1016/j.neuroimage.2015.12.056).
209. S. Canals, M. Beyerlein, H. Merkle, N. K. Logothetis, Functional MRI evidence for LTP-induced neural network reorganization. *Current biology : CB* **19**, 398-403 (2009); published online EpubMar 10 (10.1016/j.cub.2009.01.037).
210. S. B. Paek, H. K. Min, I. Kim, E. J. Knight, J. J. Baek, A. J. Bieber, K. H. Lee, S. Y. Chang, Frequency-dependent functional neuromodulatory effects on the motor network by ventral lateral thalamic deep brain stimulation in swine. *NeuroImage* **105**, 181-188 (2015); published online EpubJan 15 (10.1016/j.neuroimage.2014.09.064).
211. M. E. Raichle, The restless brain. *Brain connectivity* **1**, 3-12 (2011)10.1089/brain.2011.0019).
212. K. Kaneda, K. Isa, Y. Yanagawa, T. Isa, Nigral inhibition of GABAergic neurons in mouse superior colliculus. *The Journal of neuroscience : the official journal of the Society for Neuroscience* **28**, 11071-11078 (2008); published online EpubOct 22 (10.1523/JNEUROSCI.3263-08.2008).
213. K. Krautwald, F. Angenstein, Low frequency stimulation of the perforant pathway generates anesthesia-specific variations in neural activity and BOLD responses in the rat dentate gyrus. *Journal of cerebral blood flow and metabolism : official journal of the*

- International Society of Cerebral Blood Flow and Metabolism* **32**, 291-305 (2012); published online EpubFeb (10.1038/jcbfm.2011.126).
214. F. Zhao, T. Zhao, L. Zhou, Q. Wu, X. Hu, BOLD study of stimulation-induced neural activity and resting-state connectivity in medetomidine-sedated rat. *NeuroImage* **39**, 248-260 (2008); published online EpubJan 1 (10.1016/j.neuroimage.2007.07.063).
 215. Y. Y. Shih, C. C. Chen, B. C. Shyu, Z. J. Lin, Y. C. Chiang, F. S. Jaw, Y. Y. Chen, C. Chang, A new scenario for negative functional magnetic resonance imaging signals: endogenous neurotransmission. *The Journal of neuroscience : the official journal of the Society for Neuroscience* **29**, 3036-3044 (2009); published online EpubMar 11 (10.1523/JNEUROSCI.3447-08.2009).
 216. Y. H. Hsu, C. Chang, C. C. Chen, Negative cerebral blood volume fMRI response coupled with Ca(2)(+)-dependent brain activity in a dopaminergic road map of nociception. *NeuroImage* **90**, 43-51 (2014); published online EpubApr 15 (10.1016/j.neuroimage.2013.12.028).
 217. Y. Y. Shih, H. Y. Wey, B. H. De La Garza, T. Q. Duong, Striatal and cortical BOLD, blood flow, blood volume, oxygen consumption, and glucose consumption changes in noxious forepaw electrical stimulation. *Journal of cerebral blood flow and metabolism : official journal of the International Society of Cerebral Blood Flow and Metabolism* **31**, 832-841 (2011); published online EpubMar (10.1038/jcbfm.2010.173).
 218. Y. Y. Shih, S. Huang, Y. Y. Chen, H. Y. Lai, Y. C. Kao, F. Du, E. S. Hui, T. Q. Duong, Imaging neurovascular function and functional recovery after stroke in the rat striatum using forepaw stimulation. *Journal of cerebral blood flow and metabolism : official journal of the International Society of Cerebral Blood Flow and Metabolism* **34**, 1483-1492 (2014); published online EpubSep (10.1038/jcbfm.2014.103).
 219. A. M. Mishra, D. J. Ellens, U. Schridde, J. E. Motelow, M. J. Purcaro, M. N. DeSalvo, M. Enev, B. G. Sanganahalli, F. Hyder, H. Blumenfeld, Where fMRI and electrophysiology agree to disagree: corticothalamic and striatal activity patterns in the WAG/Rij rat. *The Journal of neuroscience : the official journal of the Society for Neuroscience* **31**, 15053-15064 (2011); published online EpubOct 19 (10.1523/JNEUROSCI.0101-11.2011).
 220. N. MacLeod, T. James, I. Kilpatrick, M. Starr, Evidence for a GABAergic nigrothalamic pathway in the rat. *Experimental brain research* **40**, 55-61 (1980).

221. C. G. Yan, R. C. Craddock, X. N. Zuo, Y. F. Zang, M. P. Milham, Standardizing the intrinsic brain: towards robust measurement of inter-individual variation in 1000 functional connectomes. *NeuroImage* **80**, 246-262 (2013); published online EpubOct 15 (10.1016/j.neuroimage.2013.04.081).
222. M. Magnuson, W. Majeed, S. D. Keilholz, Functional connectivity in blood oxygenation level-dependent and cerebral blood volume-weighted resting state functional magnetic resonance imaging in the rat brain. *Journal of magnetic resonance imaging : JMRI* **32**, 584-592 (2010); published online EpubSep (10.1002/jmri.22295).
223. K. Murphy, R. M. Birn, D. A. Handwerker, T. B. Jones, P. A. Bandettini, The impact of global signal regression on resting state correlations: are anti-correlated networks introduced? *NeuroImage* **44**, 893-905 (2009); published online EpubFeb 1 (10.1016/j.neuroimage.2008.09.036).
224. M. S. Okun, Deep-brain stimulation for Parkinson's disease. *The New England journal of medicine* **367**, 1529-1538 (2012); published online EpubOct 18 (10.1056/NEJMct1208070).
225. J. L. Vitek, T. Hashimoto, J. Peoples, M. R. DeLong, R. A. Bakay, Acute stimulation in the external segment of the globus pallidus improves parkinsonian motor signs. *Movement disorders : official journal of the Movement Disorder Society* **19**, 907-915 (2004); published online EpubAug (10.1002/mds.20137).
226. D. Weiss, M. Walach, C. Meisner, M. Fritz, M. Scholten, S. Breit, C. Plewnia, B. Bender, A. Gharabaghi, T. Wachter, R. Kruger, Nigral stimulation for resistant axial motor impairment in Parkinson's disease? A randomized controlled trial. *Brain : a journal of neurology* **136**, 2098-2108 (2013); published online EpubJul (10.1093/brain/awt122).
227. N. Chastan, G. W. Westby, J. Yelnik, E. Bardinet, M. C. Do, Y. Agid, M. L. Welter, Effects of nigral stimulation on locomotion and postural stability in patients with Parkinson's disease. *Brain : a journal of neurology* **132**, 172-184 (2009); published online EpubJan (10.1093/brain/awn294).
228. A. Fasano, C. C. Aquino, J. K. Krauss, C. R. Honey, B. R. Bloem, Axial disability and deep brain stimulation in patients with Parkinson disease. *Nature reviews. Neurology* **11**, 98-110 (2015); published online EpubFeb (10.1038/nrneurol.2014.252).
229. C. Wille, B. J. Steinhoff, D. M. Altenmuller, A. M. Staack, S. Bilic, G. Nikkhah, J. Vesper, Chronic high-frequency deep-brain stimulation in progressive myoclonic epilepsy in

- adulthood--report of five cases. *Epilepsia* **52**, 489-496 (2011); published online EpubMar (10.1111/j.1528-1167.2010.02884.x).
230. L. H. Shi, F. Luo, D. Woodward, J. Y. Chang, Deep brain stimulation of the substantia nigra pars reticulata exerts long lasting suppression of amygdala-kindled seizures. *Brain research* **1090**, 202-207 (2006); published online EpubMay 23 (10.1016/j.brainres.2006.03.050).
231. H. Guo, H. Zhang, Y. Kuang, C. Wang, X. Jing, J. Gu, G. Gao, Electrical stimulation of the substantia nigra pars reticulata (SNr) suppresses chemically induced neocortical seizures in rats. *Journal of molecular neuroscience : MN* **53**, 546-552 (2014); published online EpubAug (10.1007/s12031-013-0220-4).
232. L. Velisek, J. Veliskova, S. L. Moshe, Electrical stimulation of substantia nigra pars reticulata is anticonvulsant in adult and young male rats. *Experimental neurology* **173**, 145-152 (2002); published online EpubJan (10.1006/exnr.2001.7830).
233. J. X. Haensel, A. Spain, C. Martin, A systematic review of physiological methods in rodent pharmacological MRI studies. *Psychopharmacology* **232**, 489-499 (2015); published online EpubFeb (10.1007/s00213-014-3855-0).
234. Q. Li, Y. Ke, D. C. Chan, Z. M. Qian, K. K. Yung, H. Ko, G. W. Arbuthnott, W. H. Yung, Therapeutic deep brain stimulation in Parkinsonian rats directly influences motor cortex. *Neuron* **76**, 1030-1041 (2012); published online EpubDec 6 (10.1016/j.neuron.2012.09.032).
235. M. Michaelides, S. A. Anderson, M. Ananth, D. Smirnov, P. K. Thanos, J. F. Neumaier, G. J. Wang, N. D. Volkow, Y. L. Hurd, Whole-brain circuit dissection in free-moving animals reveals cell-specific mesocorticolimbic networks. *The Journal of clinical investigation* **123**, 5342-5350 (2013); published online EpubDec 2 (10.1172/JCI72117).
236. F. Blandini, M. T. Armentero, Animal models of Parkinson's disease. *The FEBS journal* **279**, 1156-1166 (2012); published online EpubApr (10.1111/j.1742-4658.2012.08491.x).
237. D. J. Ellens, D. K. Leventhal, Electrophysiology of Basal Ganglia and cortex in models of Parkinson disease. *Journal of Parkinson's disease* **3**, 241-254 (2013); published online EpubJan 1 (10.3233/JPD-130204).

238. R. Q. So, G. C. McConnell, A. T. August, W. M. Grill, Characterizing effects of subthalamic nucleus deep brain stimulation on methamphetamine-induced circling behavior in hemi-Parkinsonian rats. *IEEE transactions on neural systems and rehabilitation engineering : a publication of the IEEE Engineering in Medicine and Biology Society* **20**, 626-635 (2012); published online EpubSep (10.1109/TNSRE.2012.2197761).
239. N. Mallet, A. Pogosyan, L. F. Marton, J. P. Bolam, P. Brown, P. J. Magill, Parkinsonian beta oscillations in the external globus pallidus and their relationship with subthalamic nucleus activity. *The Journal of neuroscience : the official journal of the Society for Neuroscience* **28**, 14245-14258 (2008); published online EpubDec 24 (10.1523/JNEUROSCI.4199-08.2008).
240. C. S. Chan, K. E. Glajch, T. S. Gertler, J. N. Guzman, J. N. Mercer, A. S. Lewis, A. B. Goldberg, T. Tkatch, R. Shigemoto, S. M. Fleming, D. M. Chetkovich, P. Osten, H. Kita, D. J. Surmeier, HCN channelopathy in external globus pallidus neurons in models of Parkinson's disease. *Nature neuroscience* **14**, 85-92 (2011); published online EpubJan (10.1038/nn.2692).
241. A. V. Cruz, N. Mallet, P. J. Magill, P. Brown, B. B. Averbeck, Effects of dopamine depletion on network entropy in the external globus pallidus. *Journal of neurophysiology* **102**, 1092-1102 (2009); published online EpubAug (10.1152/jn.00344.2009).
242. K. Y. Fan, J. Baufreton, D. J. Surmeier, C. S. Chan, M. D. Bevan, Proliferation of external globus pallidus-subthalamic nucleus synapses following degeneration of midbrain dopamine neurons. *The Journal of neuroscience : the official journal of the Society for Neuroscience* **32**, 13718-13728 (2012); published online EpubOct 3 (10.1523/JNEUROSCI.5750-11.2012).
243. U. Schridde, M. Khubchandani, J. E. Motelow, B. G. Sanganahalli, F. Hyder, H. Blumenfeld, Negative BOLD with large increases in neuronal activity. *Cerebral cortex* **18**, 1814-1827 (2008); published online EpubAug (10.1093/cercor/bhm208).
244. H. J. Lee, A. J. Weitz, D. Bernal-Casas, B. A. Duffy, M. Choy, A. V. Kravitz, A. C. Kreitzer, J. H. Lee, Activation of Direct and Indirect Pathway Medium Spiny Neurons Drives Distinct Brain-wide Responses. *Neuron*, (2016).
245. J. K. Choi, Y. I. Chen, E. Hamel, B. G. Jenkins, Brain hemodynamic changes mediated by dopamine receptors: Role of the cerebral microvasculature in dopamine-mediated neurovascular coupling. *NeuroImage* **30**, 700-712 (2006); published online EpubApr 15 (10.1016/j.neuroimage.2005.10.029).

246. C. Y. Sander, J. M. Hooker, C. Catana, M. D. Normandin, N. M. Alpert, G. M. Knudsen, W. Vanduffel, B. R. Rosen, J. B. Mandeville, Neurovascular coupling to D2/D3 dopamine receptor occupancy using simultaneous PET/functional MRI. *Proceedings of the National Academy of Sciences of the United States of America* **110**, 11169-11174 (2013); published online EpubJul 2 (10.1073/pnas.1220512110).
247. Z. Liang, G. D. Watson, K. D. Alloway, G. Lee, T. Neuberger, N. Zhang, Mapping the functional network of medial prefrontal cortex by combining optogenetics and fMRI in awake rats. *NeuroImage* **117**, 114-123 (2015); published online EpubAug 15 (10.1016/j.neuroimage.2015.05.036).
248. S. Threlfell, S. J. Cragg, Dopamine signaling in dorsal versus ventral striatum: the dynamic role of cholinergic interneurons. *Frontiers in systems neuroscience* **5**, 11 (2011)10.3389/fnsys.2011.00011).
249. I. B. Witten, E. E. Steinberg, S. Y. Lee, T. J. Davidson, K. A. Zalocusky, M. Brodsky, O. Yizhar, S. L. Cho, S. Gong, C. Ramakrishnan, G. D. Stuber, K. M. Tye, P. H. Janak, K. Deisseroth, Recombinase-driver rat lines: tools, techniques, and optogenetic application to dopamine-mediated reinforcement. *Neuron* **72**, 721-733 (2011); published online EpubDec 8 (10.1016/j.neuron.2011.10.028).
250. F. Zhang, V. Gradinaru, A. R. Adamantidis, R. Durand, R. D. Airan, L. de Lecea, K. Deisseroth, Optogenetic interrogation of neural circuits: technology for probing mammalian brain structures. *Nature protocols* **5**, 439-456 (2010); published online EpubMar (10.1038/nprot.2009.226).
251. C. D. Nichols, B. L. Roth, Engineered G-protein Coupled Receptors are Powerful Tools to Investigate Biological Processes and Behaviors. *Frontiers in molecular neuroscience* **2**, 16 (2009)10.3389/neuro.02.016.2009).
252. S. M. Ferguson, D. Eskenazi, M. Ishikawa, M. J. Wanat, P. E. Phillips, Y. Dong, B. L. Roth, J. F. Neumaier, Transient neuronal inhibition reveals opposing roles of indirect and direct pathways in sensitization. *Nature neuroscience* **14**, 22-24 (2011); published online EpubJan (10.1038/nn.2703).
253. F. Junyent, E. J. Kremer, CAV-2—why a canine virus is a neurobiologist's best friend. *Current opinion in pharmacology* **24**, 86-93 (2015).
254. Y. Li, L. Hickey, R. Perrins, E. Werlen, A. A. Patel, S. Hirschberg, M. W. Jones, S. Salinas, E. J. Kremer, A. E. Pickering, Retrograde optogenetic characterization of the pontospinal

module of the locus coeruleus with a canine adenoviral vector. *Brain research* **1641**, 274-290 (2016).